The University of Southern Queensland
Faculty of Health, Engineering and Sciences

Investigating Wave Rotor Performance Characteristics and Design for Air Pumping Applications

A dissertation submitted by

Liam Channer

in fulfilment of the requirements of

ENG4111 and 4112 Research Project

towards the degree of

Bachelor of Engineering (Honours) BENH

Submitted: October, 2019

Abstract

Many opportunities exist in industry to improve efficiency thereby reducing energy consumption and cost. The wave rotor is a device which manipulates expansion and shock waves to compress gases with theoretically high efficiency, unrivalled by other known means. Applications vary from refrigeration to internal combustion engine supercharging. Although research has been carried out for many decades, it is very much a work in progress technology. To improve the understanding of performance, analysis and design of wave rotors used for air pumping applications. Experimental testing, computational fluid dynamics (CFD) simulations and the development of a one-dimensional (1D) mathematical analysis method has been performed in the present work. The 1D analysis method developed provides a low computational cost alternative to CFD for preliminary design with exceptional correlation to experimental results published in literature. As part of this work a pressure exchanger equalising wave rotor (PEEWR) was experimentally tested to expand on experimental performance maps published in literature. The same trends in performance were successfully reproduced, however the overall performance was substantially lower than published data for other devices. Causes for the low experimental performance was investigated using CFD. It was identified that viscous effects and suboptimal porting were the main contributors to the low experimental performance. With improved design using the tools and techniques developed and demonstrated in this work it is expected that wave rotor performance matching that demonstrated elsewhere can be achieved. This will enable future research, development and deployment of wave rotor concepts for application in industrial energy efficiency initiatives.

University of Southern Queensland

Faculty of Health, Engineering & Sciences

ENG4111/2 ***Research Project***

Limitations of Use

Certification of Dissertation

I certify that the ideas, designs and experimental work, results, analyses and conclusions set out in this dissertation are entirely my own effort, except where otherwise indicated and acknowledged.

I further certify that the work is original and has not been previously submitted for assessment in any other course or institution, except where specifically stated.

Liam Channer

[redacted]

Acknowledgements

The author would like to acknowledge Prof. David Buttsworth for providing this research opportunity by sponsoring and supervising the work. Without this it wouldn't have been possible.

Thanks to Mr Byrenn Birch for providing support with LaTeX and providing access to USQ's high powered computer for running CFD simulations it is greatly appreciated.

Lastly, thanks to the USQ mechanical and electrical technical staff who have also been important to the success of the project by manufacturing parts for the experimental test rig, supplying electronic components and the data acquisition system.

Table of Contents

List of Figures

List of Tables

Acronyms

1D	One Dimensional
2D	Two Dimensional
3D	Three Dimensional
CFD	Computational Fluid Dynamics
DAQ	Data Acquisition
H	High pressure port
IC	Internal Combustion
IC	Integrated Circuit
L	Low pressure port
M	Medium pressure port
NASA	National Aeronautics and Space Administration
PEEWR	Pressure Exchanger Equalising Wave Rotor
TUSQ	USQ hypersonic facility
UK	United Kingdom
USQ	University of Southern Queensland
VFD	Variable Frequency Drive

Nomenclature

Roman Symbols

Symbol	Description	Units
a	Speed of sound	$\mathrm{m\,s^{-1}}$
d	Diameter	m
E	Expansion wave	–
l	Length	m
$\dot{m}$	Mass flow rate	$\mathrm{kg\,s^{-1}}$
m	Mass	kg
Ma	Mach number	–
P	Pressure	Pa
r	Radius	m
R	Gas constant	$\mathrm{J\,kg^{-1}\,K^{-1}}$
Re	Reynolds number	–
T	Temperature	K, °C
t	Time	s
u	Velocity	$\mathrm{m\,s^{-1}}$
W	Shock wave speed	$\mathrm{m\,s^{-1}}$
x	Axial distance	m
x_1, x_2, x_3, x_4, x_{4t}, x_5, x_{5t}, x_6, x_9	Zones on xt diagram Figure 3.1	–
x_6, x_6', x_8	Zones on xt diagram Figure 3.2	–

Greek Symbols

Symbol	Description	Units
γ	Ratio of specific heats	–
ζ	Wave rotor performance parameter, = m_L/m_H	–
η	Isentropic efficiency	–
θ	Rotor rotation angle	rad, degrees
μ	Viscosity	Pa s
ν	Kinematic viscosity	$m^2\,s^{-1}$
Π	Shock wave pressure ratio P_2/P_1	–
ρ	Density	$kg\,m^{-3}$
ϕ	Optimal port angle	rad, degrees
ω	Angular Velocity	$rad\,s^{-1}$

Subscripts

Script	**Description**
0	Stagnation condition
1	Initial
2	Final
A1, A2, B1, B2, B3, C1, C2, C3, C4, D1, D2	Zones on xt diagram Figure 3.1
A, B, C, D	A = A1 and A2, B = B1 and B2 and B3 etc.
atm	Atmospheric condition
c	Close
cr	Critical
$E1$, $E2$	Expansion waves in Figure 3.1
$head$	Expansion wave head
max	Maximum value
min	Minimum value
o	Open
p	Particle
$S1$, $S2$, $S3$	Shock waves in Figure 3.1
$tail$	Expansion wave tail

Chapter 1

Introduction

Contents

The wave rotor is a type of turbo machine which manipulates expansion and shock waves to compress gases. The applications for wave rotors vary from refrigeration to internal combustion engine supercharging. Although there is a large quantity of literature on wave rotors, the literature specifically on pressure exchanger equalising wave rotors is limited with only one paper publishing experimental results. The results published by Kentfield (1969) are extremely promising, however, fail to provide enough detail to be able confidently to reproduce or improve on.

1.1 Motivation for the Research

Steam is used extensively throughout industry. Opportunities exist to improve efficiency through vapour recompression. Currently mechanical vapour recompression is used in some instances to compress low pressure steam to a usable pressure so more energy can be extracted, hence improving the overall efficiency of the plant. Potentially more efficient and simpler alternatives have been proposed such as an ejector or wave rotor. Rather than using high pressure steam to drive a turbine and then a compressor, the ejector or wave rotor would compress the low pressure steam directly using the high pressure steam. While an ejector is a simpler device relative to a wave rotor, theoretically the latter is significantly more efficient.

The pressure exchanger equalising wave rotor (PEEWR) configuration is in principle ideally suited to the application of vapour recompression. However, there are still many aspects of the device requiring further research. The only experimental results published are by Kentfield (1969). The results are promising, however are lacking information e.g. almost all quantities are expressed in a dimensionless form. Also the working fluid used by Kentfield (1969) was air.

The current wave rotor research at USQ is aimed at expanding the understanding of PEEWRs using air as the working fluid so the work done by Kentfield (1969) can be used as reference. It also has the added advantage of being simpler than steam both for experimental and analytical work. Once a comprehensive understanding is gained using air as the working fluid the focus will be shifted to using steam.

1.2 Overview of Research

The purpose of this research is to try and address some of the shortcomings in literature by undertaking experimental testing to validate the results by Kentfield (1969) and generate some basic understanding of parameters affecting performance. Also, a simple 1D analysis method based on the Euler compressible flow equations is developed to aid with preliminary design. Computational Fluid Dynamics (CFD) is also used to help visualise what is going on inside the device and validate experimental and simple 1D analysis results.

1.2.1 Experimental Testing

The experimental part of this project finalised the manufacturing of a PEEWR already designed and partially manufactured at USQ. The device was then commissioned for experimental testing with the relevant instrumentation and data acquisition systems. From here the device was tested over a range of pressure ratios to map the performance.

1.2.2 One Dimensional Analysis

The computational cost of simulating a wave rotor using CFD is extremely high due to the nature of the fluid flow and dynamic channels. Hence, it is valuable to develop a basic analysis method. Basic analysis procedures have already been developed for other types of wave rotors. As part of this work a procedure to analyse the PEEWR was developed and validated.

1.2.3 Computational Fluid Dynamic Analysis

Computational Fluid Dynamics allows for more detailed analysis of a PEEWR. It also aids with visualising the nature of the fluid flow within the device. The CFD carried out in this research was focused on developing a methodology for simulating the PEEWR using ANSYS Fluent, validating the 1D analysis method and helping evaluate the design of the PEEWR used in the experimental work.

Chapter 2

Background and Literature Review

Contents

2.1 The Wave Rotor

The Wave rotor is a type of turbo machine. The device has the potential to be used in countless applications from jet engines to refrigeration systems (Akbari, Nalim & Mueller, 2006). Wave Rotor designs vary, however they all work on the same principle of transferring energy from a high to a low energy flow directly without intermediate components such as pistons, diaphragms or turbines (Azoury, 1965). In other words, the two flows come into direct contact with one another to transfer energy.

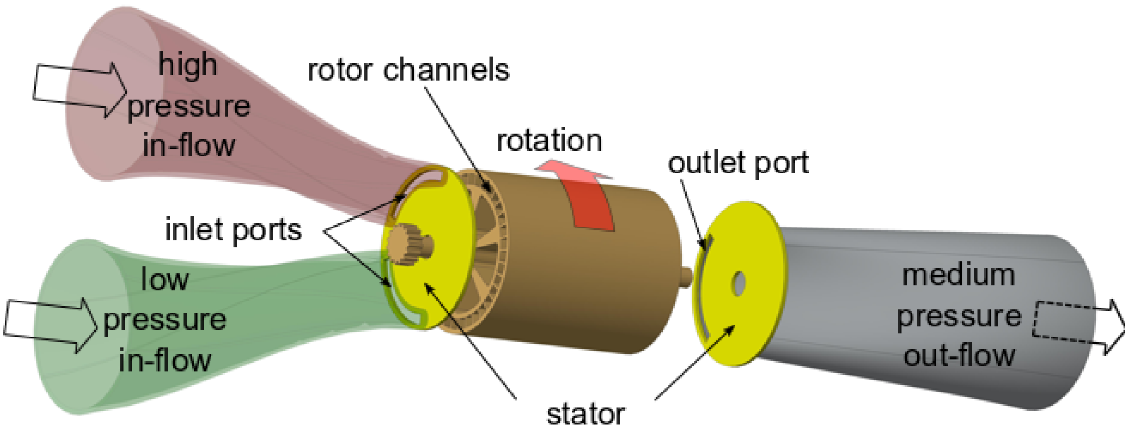

Figure 2.1: Three port wave rotor typical setup (Adapted from Buttsworth, personal communication, 2019)

Wave rotors consist of three key components: the rotor and two end plates. The rotor has multiple axial channels arranged in a circle around the centre axis. The end plates are located at the ends of rotor equipped with strategically positioned ports which provide valving for each channel as the rotor rotates (see Figure 2.1). Generally the end plates are stationary and the rotor spins. However, wave rotors have also been designed with the channels stationary and the end plates rotating, which allows access to the channels for instrumentation during research. However, this creates more complications in commercial applications and reduces efficiency (Akbari et al., 2006).

Ports in the end plates strategically allow different energy level flows to enter and leave the rotor channels creating unsteady flow in each channel. This unsteady flow forms shock and expansion waves which are manipulated though port positions and rotor speed to exchange energy between the flows in a desired manner.

The rotor is typically shaft driven from an external power source eg. crank shaft or electric motor. The power required to rotate the rotor only has to overcome the air resistance and bearing friction. The energy exchange is achieved solely through manipulation of unsteady flow. Hence, with good design, the energy required to rotate the rotor can be made negligible. Alternatively wave rotors can be made self driving by using some of the fluid momentum and altered channels to drive the rotor (Gyarmathy, 1983; Hermann, 1989). However this adds more complexity to controlling rotor speed.

The isentropic efficiency of ideal shock waves as shown by Figure 2.2 is extremely high when compared to other compression methods for pressure ratios up to 2.2. This has

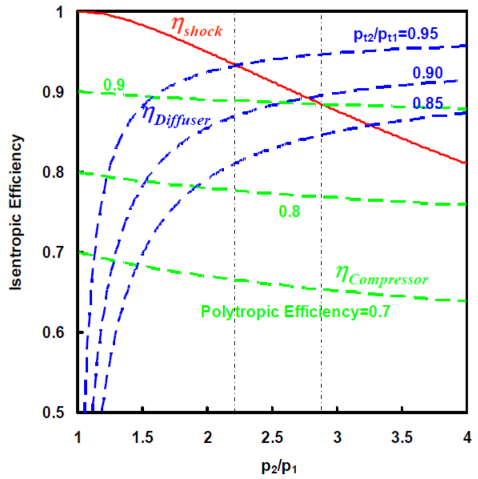

Figure 2.2: Multiple compression methods isentropic efficiency vs compression ratio (Akbari, Nalim & Mueller, 2006)

generated a lot of research interest in wave rotors for low pressure gain applications (Akbari et al., 2006). Other advantages are low rotational speed compared to other turbo machinery, very fast response hence negligible lag, channel erosion is low, the device is self cooled and simpler to manufacture. Despite all the advantages the commercial use of wave rotors has been scarce due to off design issues and lack of knowledge on the best wave rotor configuration for given applications. Sealing between the rotor and end pates is still an area for improvement. The current method utilises a small gap between the rotor and end plate, however, this introduces losses as some of the flow leaks between the end plates and rotor.

2.2 History of Wave Rotor Research

The wave rotor concept was first proposed in different forms between 1906 and 1928 (Akbari et al., 2006). However, poor knowledge of unsteady flow hampered the development (Kentfield, 1998) until the 1940s when a Swiss inventor, Claude Seippel successfully implemented a topping wave rotor for a gas turbine. As described by Akbari et al. (2006) the wave rotor was expected to increase performance by 80% and efficiency by 25%. The experimental results were far from ideal, however they proved the wave rotor concept. This work by Seippel lead to the development of the "Comprex", a pressure wave supercharger used on diesel engines (Hîrceagă, Iancu & Müller, 2005).

Seippel worked for the Swiss company Brown Boveri, now known as Asea Brown Boveri, which started to develop the Comprex (Akbari et al., 2006; Berchtold & Gardiner, 1958) with promising signs. However, due to the complexity, Brown Boveri shelved the project to focus on gas turbines (Berchtold & Gardiner, 1958). The development of the Comprex was continued by the US firm ITE Circuit Breaker Company. The US Bureau of Aeronautics and Cornell University were also involved. The development by ITE Circuit Breaker took place between 1947-1957 (Berchtold & Gardiner, 1958). The project was continued by the Brown Boveri Company who commercialised the Comprex in 1970s according to Akbari et al. (2006) where Hitomi, Yuzuriha and Tanaka (1989) reported the Comprex was commercially used in tractors as early as 1956. The Comprex has been used commercially in diesel tractors, trucks and family cars, most famously the Mazda 626 (Akbari et al., 2006; Mayer, Oda, Kato, Haase & Fried, 1989). Akbari et al. (2006) reported that Mazda produced more than 150,000 cars fitted with a Comprex. According to Akbari et al. (2006) Mazda bought the Comprex from Brown Boveri in the late 1980s.

Independent of the Comprex development, wave rotors for aeroplane applications were conceived in the 1940s by an engineer in Budapest. Later the UK company Power Jets Ltd was inspired by his idea and researched the applications of wave rotors for internal combustion engine supercharging in 1949. Power Jets Ltd expanded their wave rotor applications to include refrigeration and gas turbines, wave rotor configurations including pressure equalisers and dividers. According to Akbari et al. (2006) two prototype air cycle refrigerators with wave rotors were tested in gold mines located in both South Africa and India. The research work was continued at Imperial College, London in collaboration with several other companies.

In the UK and independent of other efforts, the Ruston-Hornsby Company funded the build and testing of a wave rotor engine in the 1950s (Akbari et al., 2006; Shreeve & Mathur, 1985). This wave rotor engine was first conceived much earlier by the lead researcher Pearson and was known as the Pearson Rotor. As described by Akbari et al. (2006) the channels were helical rather than straight so mechanical work could be extracted from the gas flow. Results proved the device could produce up to 26 kW at design conditions and could operate at between 3000 and 18000 rpm. This was impressive for a device only 230 mm in diameter and 76 mm in length. However, due to the unrefined manufacturing and design, the thermal efficiency was only 10%. Unfortunately the company ran into financial difficulties. Pearson was unable to attract alternative funding to continue the project (Shreeve & Mathur, 1985).

Other organisations such as Ford Motors, Rolls Royce, French National Aerospace Re-

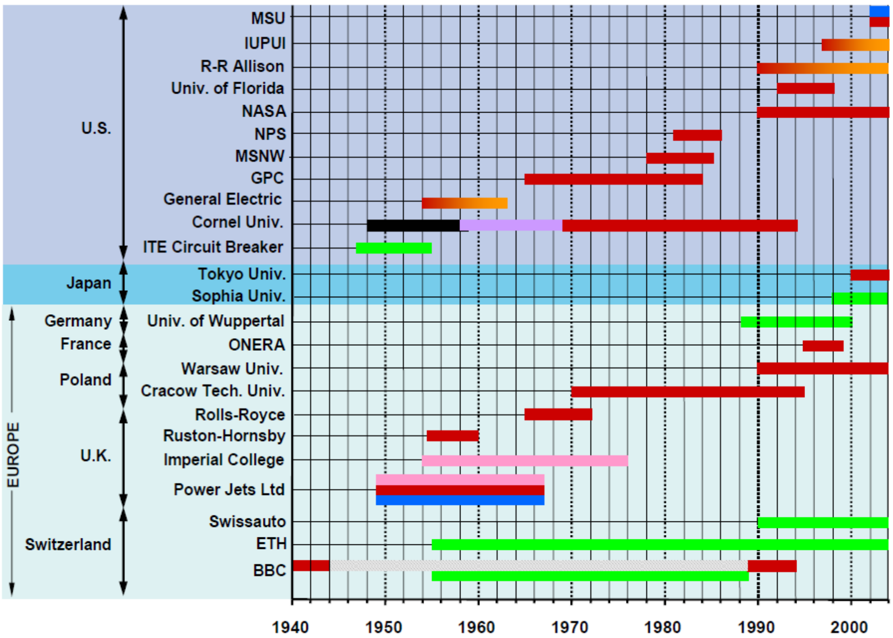

Figure 2.3: Past wave rotor research. Red: gas turbine application, Green: IC engine supercharging, Blue: refrigeration cycle, Pink: pressure divider and equalizer, Purple: wave superheater, Orange: internal combustion wave rotors, Black: general applications (Akbari, Nalim & Mueller, 2006)

search Establishment and NASA were also involved in early wave rotor research. Akbari et al. (2006) reports Rolls Royce undertook both theoretical and experimental research in the application of topping cycles for gas turbines in the 60s and 70s. The French National Aerospace Research Establishment has also spent time investigating wave rotors in the mid to late 1990s. The focus was on improving gas turbine cycles for the application of auxiliary power units, turbo shaft, turbo fan, and turbo jet engines (Fatsis & Ribaud, 1999).

NASA have been researching wave rotors since the late 1980s in collaboration with Rolls Royce Allison. Today they are leaders in the field of wave rotors in both analytical and experimental research. NASA's collaboration with Rolls-Royce Allison is working to bring predicted efficiency improvements to the Allison 250 turbo shaft engine known as the Rolls-Royce M250 to reality. Incorporating a wave rotor in the engine cycle is also predicted to increase the specific power by 18-20% and reduce specific fuel consumption by 12 – 22 % according to Akbari et al. (2006).

Wave rotor research carried out pre 2004 is summarised by Figure 2.3 along with the applications being investigated.

2.3 Wave Rotor Types and Applications

Wave rotors have the potential to be used in multiple applications from supercharging to refrigeration. This section will discuss some of the main wave rotor applications being investigated.

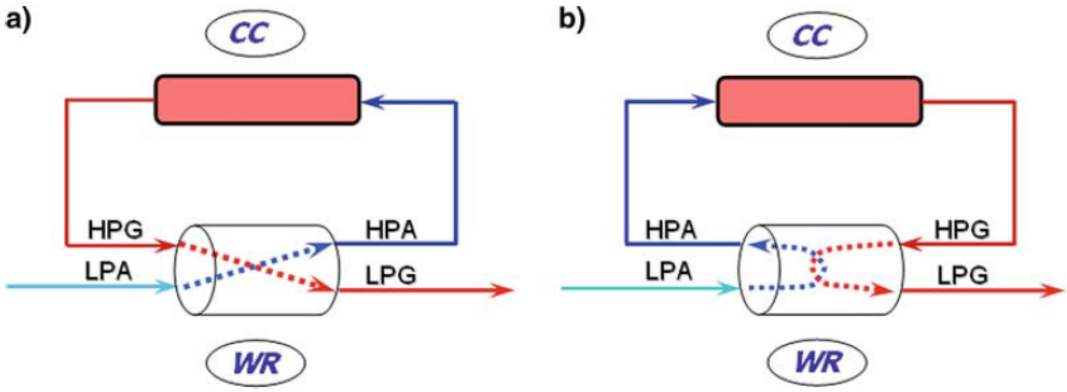

Figure 2.4: Wave rotor configurations: (a) through flow wave rotor; and (b) vs reverse flow setup (Iancu, Piechna & Müller, 2008)

The number of ports a wave rotors has varies with design and application, the most common is four ports. According to Akbari et al. (2006), extensive research has also been conducted into: two, four, five and nine port wave rotors intended for use in a gas turbine cycle whereas, three port setups have been used for pressure dividing and equalising applications. The porting configurations also vary with design. Wave rotors with the inlets on one side and outlets on the other side are known as a through flow set-up. Having the driving fluid ports on one side and the driven fluid ports on the other is called a reverse flow set-up. Figure 2.4 depicts the two configurations. Both the driving and driven fluids pass through the whole channel in a through flow setup whereas in the reverse flow configuration, the driving and driven fluids do not travel the whole channel (Iancu, Piechna & Müller, 2008). Hence, Akbari et al. (2006) reports, through flow setups have an even temperature distribution, whereas reverse flow setups have an uneven temperature distribution with typically one side hotter than the other. Depending on the application and temperature difference between driven and driving fluids, through flow and reverse flow setups have their advantages and disadvantage. The Comprex is an example of a four port reverse flow wave rotor.

2.3.1 Pressure Equaliser and Divider

Pressure equalising wave rotors are relevant to compressible fluid pumping applications where ejectors are employed (Kentfield, 1963). Other applications have also been proposed such as thrust augmenters for aircraft jet propulsion units (Kentfield, 1963). As described by Kentfield (1963) an equalising wave rotor has the potential to be significantly more efficient than an ejector as the operating cycle of the wave rotor is "in essence reversible". This is confirmed by Azoury (1965) who reports ejectors have a maximum overall isentropic efficiency of 21% compared to 75% for equalisers (see Figure 2.5). Kentfield (1969) reported a slightly smaller maximum efficiency of 70% for the equaliser however, this is still a remarkable improvement on the ejector's 21%.

The pressure divider wave rotor is effectively the equaliser operating in reverse, i.e. splitting a medium pressure flow into a high and low pressure stream. Kentfield (1963) identified two possible applications: cooling and high pressure boosting. NASA has been researching pressure divider wave rotors for topping cycle applications to improve turbine performance and efficiency by boosting turbine inlet temperature and pressure (Wilson, 1998). The divider wave rotor Kentfield (1969) tested was been researched for refrigeration applications. Analysis of wave rotor operation proceeds most readerly by considering an 'unwrapped' rotor to illustrate the channels moving up the page on a 2D plane as illustrated in Figure 2.6 which depicts the divider and equaliser setup experimentally tested by Kentfield (1969). Other configurations for the 3 ports are possible, however as determined by Kentfield (1963) the configuration presented in Figure 2.6 is theoretically the best option.

Referring to the left hand portion of Figure 2.6 the divider works as follows. When the left end of a channel opens to the medium pressure port a shock wave travels to the right compressing the fluid in the channel and reflects off the closed right end of the channel further compressing the fluid. Just after the shock wave reflects the high pressure port opens allowing the fluid to exit the channel at the high pressure. The reflected shock wave arriving at the left end of the channel defines the closing of the medium pressure port. This causes an expansion wave which travels to the right dictating the closing of the high pressure port on arrival at the right end of the channel. Just after closing the medium pressure port, the low pressure port opens allowing the low pressure fluid in the channel to exhaust. The expansion wave that dictated the closing of the high pressure port reflects and travels back to the left end of the channel. When the reflected expansion wave arrives

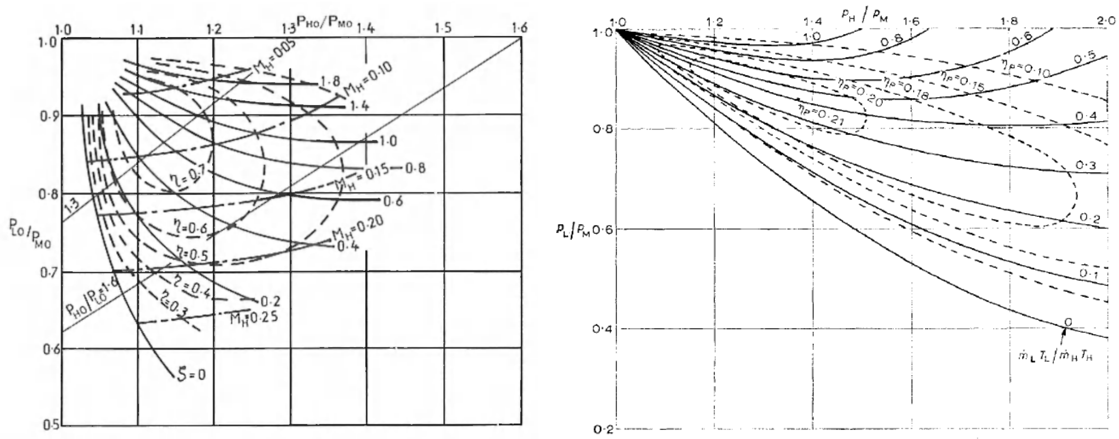

(a) Equaliser wave rotor (b) Ejector

Figure 2.5: Comparison of wave rotor and ejector performance (Azoury, 1965)

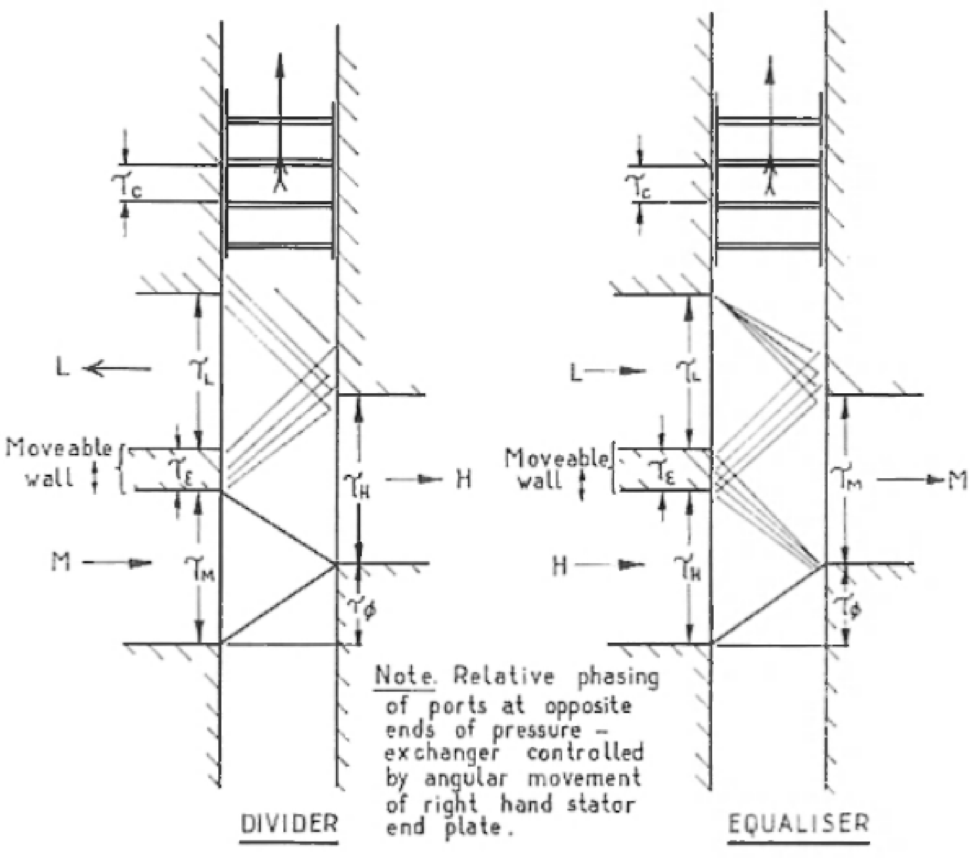

Figure 2.6: Unwrapped divider and equaliser schematic (Kentfield, 1969)

at the left end of the channel the low pressure port is closed and the channel travels round (back to the bottom of the page as it were) for the cycle to be repeated.

Referring to the right hand portion of Figure 2.6, the equaliser wave rotor works as follows. When the left end of a channel opens to the high pressure port a shock wave travels to the right compressing the fluid in the channel. Just before the shock wave reaches the right end of the channel the medium pressure port opens allowing the fluid to exit the channel at the medium pressure. This causes an expansion wave which travels to the left dictating the closing of the high pressure port on arrival at the left end of the channel. As the fluid is still moving a second expansion wave occurs travelling to the right. This reduces the pressure behind the expansion wave and as the low pressure port opens it sucks in the low pressure fluid. When the second expansion wave reaches the right hand end of the channel the medium pressure port is closed. This causes a shock wave which converts the dynamic pressure of the low pressure flow into static pressure. When the shock wave reaches the left end of the channel the low pressure port is closed and the channel travels round (back to the bottom of the page as it were) for the cycle to be repeated.

2.3.2 Internal Combustion Engine Supercharging

Internal combustion engine supercharging is the only successfully commercialised application of a wave rotor to date. This wave rotor was marketed as the Comprex. The Comprex works by extracting energy from the exhaust gas to compress the intake air. The configuration of the Comprex fitted to an internal combustion engine is depicted in Figure 2.7 along with an unwrapped schematic (Mardarescu, Hirceaga, Radu & Leahu, 2010). The main advantages of using a wave rotor as a engine supercharger compared to conventional turbine compressor arrangements is the device is more efficient, simpler to manufacture, rotates slower, has significantly less boost response time and higher pressure boosting ratios, as illustrated in Figure 2.8 (Akbari et al., 2006; Costiuc & Chiru, 2017; Mataczynski, 2014). Also internal combustion engines fitted with such a device are reported to have reduced NOx emissions (Costiuc & Chiru, 2017).

Since the commercialisation of the Comprex, research on wave rotor internal combustion engine super charging applications have been focused on improving the off design performance and furthering the understanding of key design parameters. This is being achieved by taking advantage of CFD and development of basic analysis methods along with reverse engineering (Hitomi et al., 1989; Mardarescu et al., 2010). Some of the

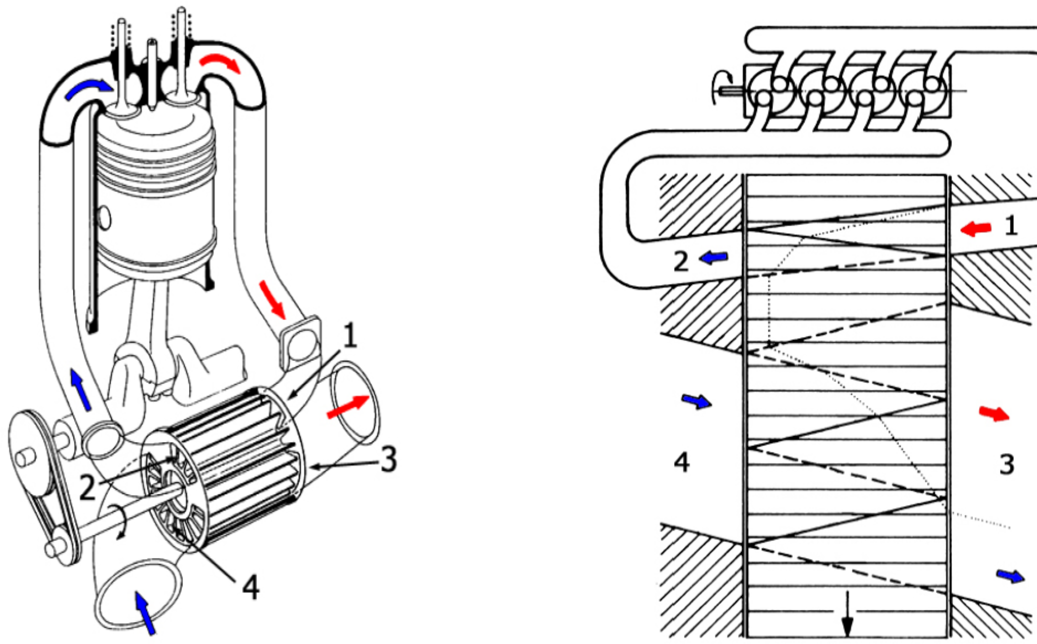

Figure 2.7: Comprex arrangement schematics. 1 - exhausted gas intake, 2 - air outlet port 3 - exhausted gas outlet and 4 - air intake port (Mardarescu, Hirceaga, Radu & Leahu, 2010)

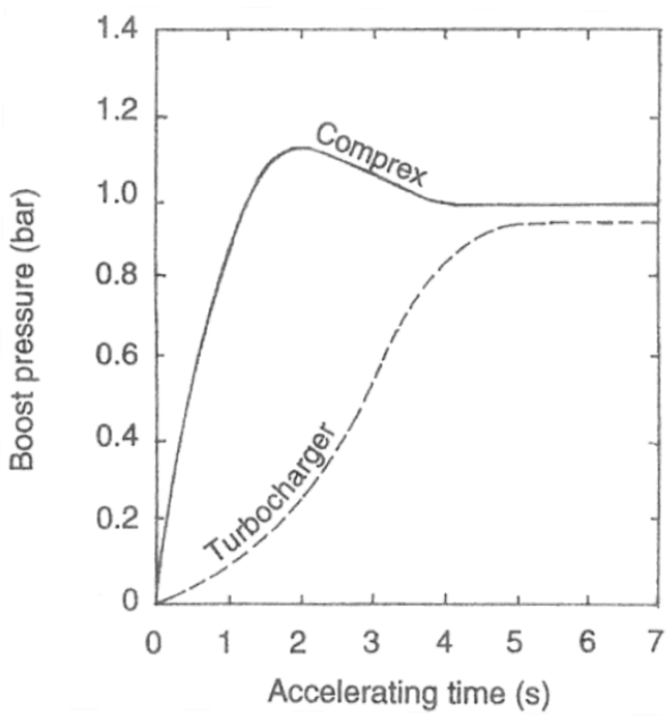

Figure 2.8: Comprex performance vs standard turbocharger (Mataczynski, 2014)

design features are still not fully understood in open literature (Costiuc & Chiru, 2017).

An example of the improvements being investigated is driving the Comprex with a variable speed electric motor to improve performance (Leahu & Chiru, 2015). The experimental results show an improvement in efficiency over a wide operating range as the speed is adjusted to the optimal point for the given operating conditions rather than it being fixed by the crank shaft speed.

Swissauto, a Swiss engine manufacturer, has developed a pressure wave supercharger known as the "Hyprex" for small petrol engines which is believed to have superior performance to the Comprex (Akbari et al., 2006; ‘Swissauto’, 2019). The device has been demonstrated, however it is yet to be commercialised. Scaling down a Comprex has also been investigated by Mataczynski (2014) for improving the performance of internal combustion engine propelled aircraft operating at high altitude.

2.3.3 Gas Turbines

Gas turbine topping applications have the capability of increasing the turbine inlet pressure by 15-20% over the air delivered directly by the compressor (Akbari et al., 2006; Wilson, 1998). Hence considerably more work can be extracted increasing the overall thermodynamic efficiency. The wave rotor is placed between the compressor and turbine as shown in Figure 2.9. The wave rotor further compresses the air before entering the combustor. This leads to a more complete combustion, i.e more energy is extracted from the fuel. The fluid leaving the combuster is at a high pressure and temperature than if the wave rotor was not present in the cycle. Before the fluid enters the turbine it travels though the wave rotor compressing the inlet air to the combustor and cools to the same temperature as an untopped cycle. This allows for combustion at a higher temperature without being limited by the turbine blade material. Since the wave rotor is a through flow configuration it can handle higher temperatures as the inlet air cools the channels thus keeping a lower average rotor temperature (Akbari et al., 2006; Mataczynski, 2014).

Wave rotors have also been investigated for gas turbines where the combustion takes place in the rotor channels eliminating an external combustion chamber (Lenoble & Ogaji, 2010). Such a configuration is referred to in literature as an internal combustion wave rotor (Akbari et al., 2006), as illustrated in Figure 2.10.

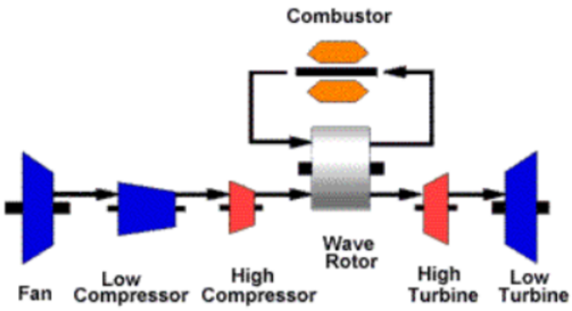

Figure 2.9: Topping wave rotor for gas turbine (Mataczynski, 2014)

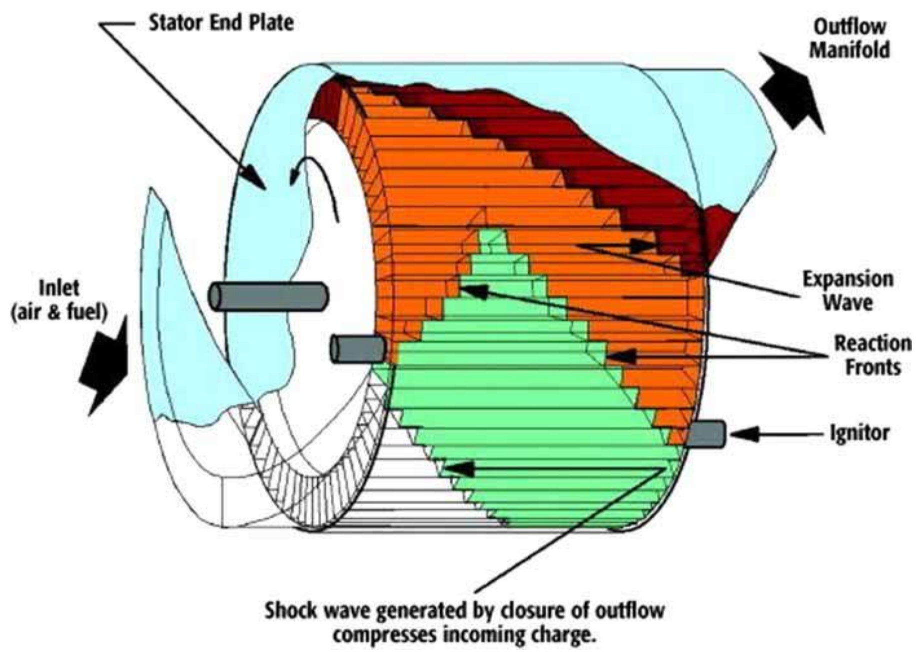

Figure 2.10: Topping wave rotor for gas turbine with combustion in channel (Lenoble & Ogaji, 2010)

2.3.4 Refrigeration

Refrigeration applications for wave rotors have seen a renewed interest recently with quite a lot of literature being published (Dai, Cheng, Zou & Hu, 2015; Hu, Yu & Liu, 2018; Yuqiang et al., 2010; Zhao & Hu, 2017). There are several proposed variations of the implementation of a wave rotor in the refrigeration cycle. For example the wave rotor has been investigated as a more efficient alternative to a throttling valve or turbo expander (Zhao & Hu, 2017). A more novel application is a water refrigeration (R718 refrigerant) cycle as proposed by Kharazi, Akbari and Müller (2004) and illustrated in Figure 2.11. Conventional R718 refrigeration systems using water as refrigerant are already commercialised in Europe, however due to their large size and the cost there is need for optimisation for wider use. Implementing a wave rotor in the cycle can reduce the size and cost significantly as it eliminates the condenser and the second stage of the compressor while improving the cycle efficiency (Akbari & Mueller, 2005; Kharazi, Akbari & Müller, 2005).

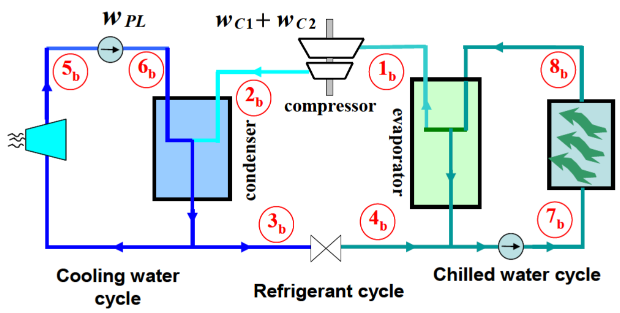

(a) Standard R718 refrigeration cycle

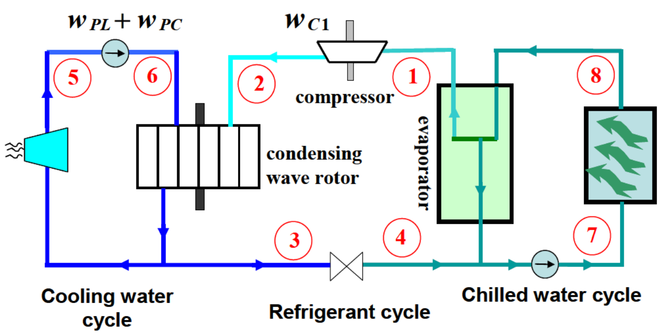

(b) Wave rotor incorporated in refrigeration cycle

Figure 2.11: Wave rotor refrigeration application (Kharazi, Akbari & Müller, 2004)

2.3.5 Other applications

Cornell Aeronautical Laboratory developed and built a wave rotor back in the 1960s which was used to superheat helium as part of a hypersonic wind tunnel (Akbari et al., 2006). The wave rotor was 2 m in diameter and compressed helium to 120 atmospheres and raised the temperature to more than 4000 K in the test section. This gave the wind tunnel remarkable performance with run-times over 15 seconds. The device was in service for 11 years (Weatherston & Hertzberg, 1967).

Micro turbine wave rotors are also being researched (Akbari & Mueller, 2005; Tüchler & Copeland, 2019). The device compresses, combusts and expands an air-fuel mixture. The rotor channels are helical to enable work to be extracted. This application was first proposed and researched by Pearson back in the early 1900s (Akbari et al., 2006). A recent paper by Tüchler and Copeland provides promising results with an experimentally measured efficiency as high as 80%.

2.4 Numerical Methods Used in Wave Rotor Research

There are several methods used for simulating wave rotors. These range from simple one dimensional methods to full three dimensional computational fluid dynamics (CFD) simulations.

The simple one dimensional method such as discussed by Chan, Liu, Xing and Song (2017), Iancu et al. (2008), Mardarescu et al. (2010) works by analysing a four port wave rotor on a xt diagram. The rotor's circumference is unwrapped as illustrated in Figure 2.12 and the channel cross sectional area is treated as finite. Each primary expansion and shock wave is calculated using the Euler compressible flow equations. This gives a good approximate method for determining the port timing and mass entrainment.

The commercial CFD software ANSYS Fluent is reported in literature for analysing wave rotors (Chan et al., 2017; Iancu, Piechna & Müller, 2005, 2008). The most popular model is inviscid with the main objective to reduce computational cost. The port timing is usually determined by other means such as the one dimensional analysis method described above and then refined by CFD. These stimulations are generally carried out as 2D. However a scaled down 3D simulation has been reported by Iancu et al. (2005). Both implicit and explicit solving methods have been used. There does not seem to be any consensus on

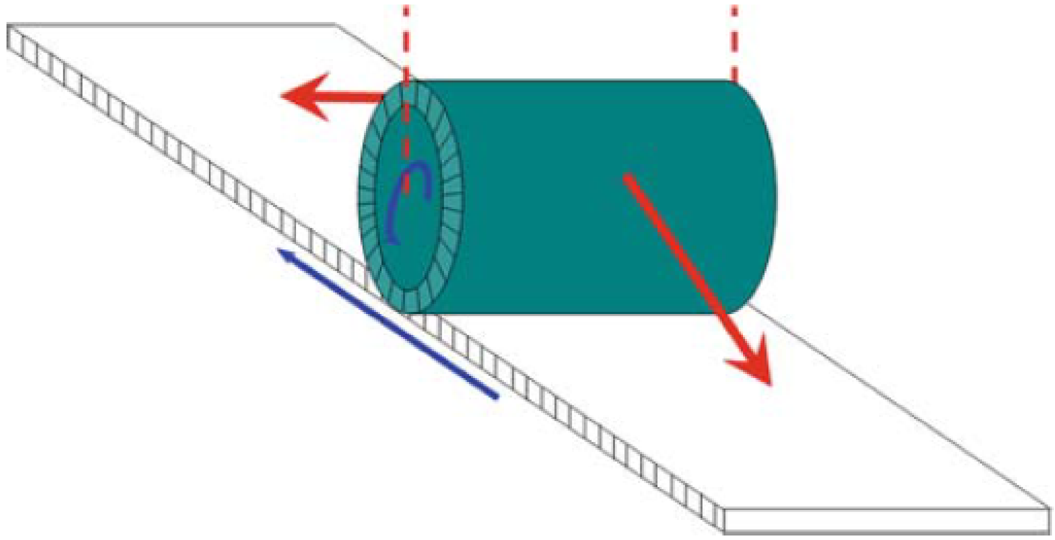

Figure 2.12: 3D to 2D wave rotor schematic (Iancu, Piechna & Müller, 2008)

the best method (Akbari & Mueller, 2005; Iancu et al., 2005).

Although commercial CFD software can simulate a wave rotor with reasonable accuracy it requires extreme computational resources and has inherent limitations. This has led to researchers developing their own simulation code for example. The most widely published wave rotor CFD code is a quasi one dimensional approach that has been developed by Paxson and Wilson (1995) at NASA. The code takes gradual port opening, leakage, viscous effects and heat transfer between channel walls and fluid into account. The code has been improved over time and now also takes the circumferential velocity into account and allows for simulating off design operating conditions. The code has been demonstrated to be within 6% of experimental results (Mataczynski, 2014).

2.5 Knowledge Gap

Although there is a large quantity of literature on wave rotors, the literature specifically on pressure exchanger equalising wave rotors (PEEWR) is limited to only one paper publishing experimental results. The results published by Kentfield (1969) are extremely promising, however fail to provide enough detail to be able confidently to reproduce or improve on.

There are a number of publications on the analysis methods used in wave rotors, however they are focused on four port configured wave rotors which operate on a different cycle. Most of the CFD methodology is transferable to the 3 port PEEWR setup. However, an in-depth CFD methodology is lacking in current open literature. The simple analysis method based on the Euler compressible flow equations presented in current literature has not been developed for a 3 port PEEWR setup.

The purpose of this work is to address some of the short-comings in literature by undertaking experimental testing to validate the results by Kentfield (1969) and generate some basic understanding of parameters affecting performance. Also, a simple 1D analysis method based on the Euler compressible flow equations has been developed to aid the preliminary design. While CFD is used to help visualise the flow processes inside the device and validate experimental and simple 1D analysis results.

Chapter 3

One Dimensional Analysis Method

Contents

The computational cost of simulating a wave rotor using CFD is extremely high due to the nature of the fluid flow and dynamic channels. Hence, it is valuable to develop a basic analysis method. Basic analysis procedures have already been reported by Iancu et al. (2008) and Chan et al. (2017) and are applicable to a four port cycle based on the Euler compressible flow equations. The purpose of this chapter is develop a procedure to analyse the pressure exchanger equaliser wave rotor which is a three port device.

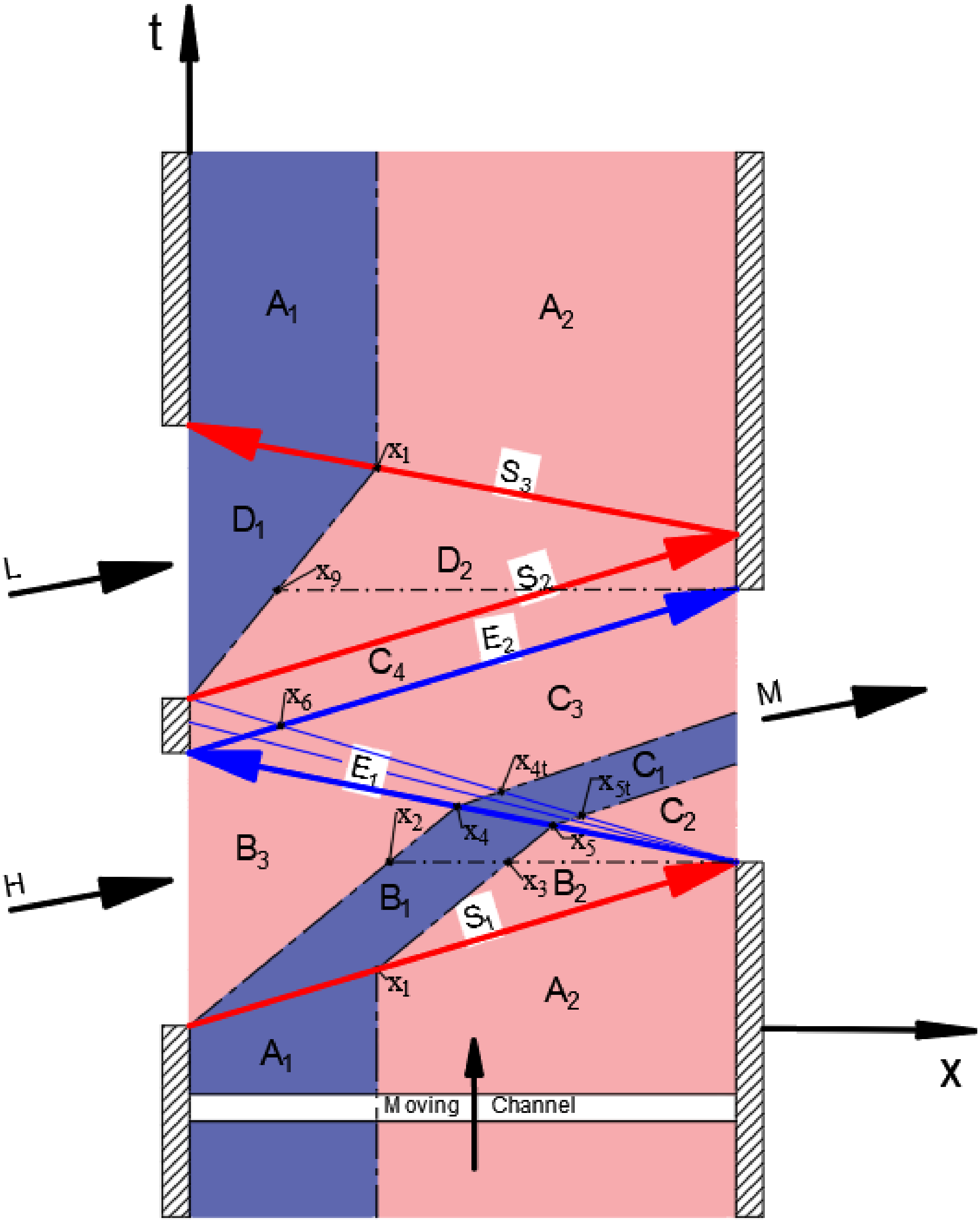

Figure 3.1: PEEWR zones

3.1 Analysis Overview

Referring to Figure 3.1, in zone A the channels contain the fluid from the last cycle. As the H port opens a shock wave (S_1) travels down the channel. The fluid behind the shock wave forms zone B. Just before the shock wave (S_1) reaches the end of the channel the M port opens. This port opening causes the expansion wave E_1. The fluid behind the expansion wave E_1 forms the third zone C. Expansion wave E_1 is reflected of the wall between the H and L ports forming expansion wave E_2. The fluid behind E_2 forms zone C4. As the expansion wave E_2 reaches the end of the channel the M port closes. The closing of H port is determined by the head of expansion wave E_1 where the opening of the L port is determined by the tail of E_1 reaching the end of the channel. When the L port opens shock wave S_2 travels down the channel and reflects off the closed end of the channel forming the third sock wave S_3. S_3 converts the momentum of the fluid travelling down the channel into static pressure. The dashed lines show the interface between the H and L entrained fluids. From theses interfaces each zone can be divided into sub zones showing how the fluid flows though each channel.

The properties/conditions of each zone can be calculated using the following standard equations (Anderson, 1990; Chan et al., 2017; Iancu & Müller, 2006; Iancu et al., 2008).

Isentropic relations:

$$a = \sqrt{\gamma R T} \tag{3.1}$$

$$\frac{T_0}{T} = 1 + \frac{\gamma - 1}{2} Ma^2 \tag{3.2}$$

$$\frac{P_0}{P} = \left(1 + \frac{\gamma - 1}{2} Ma^2\right)^{\frac{\gamma}{\gamma-1}} \tag{3.3}$$

$$\frac{P_2}{P_1} = \left(\frac{T_2}{T_1}\right)^{\frac{\gamma}{\gamma-1}} = \left(\frac{a_2}{a_1}\right)^{\frac{2\gamma}{\gamma-1}} \tag{3.4}$$

$$\frac{T_2}{T_1} = \left(\frac{a_2}{a_1}\right)^2 \tag{3.5}$$

Shock relations:

$$\Pi_S = \frac{P_2}{P_1} \tag{3.6}$$

$$\frac{T_2}{T_1} = \Pi_s \left(\frac{\frac{\gamma+1}{\gamma-1} + \Pi_s}{1 + \frac{\gamma+1}{\gamma-1}\Pi_s}\right) \tag{3.7}$$

$$W = a_1\sqrt{\frac{\gamma+1}{2\gamma}(\Pi_s - 1) + 1} \tag{3.8}$$

$$u_p = \frac{a_1}{\gamma}(\Pi_s - 1)\left(\frac{\frac{2\gamma}{\gamma+1}}{\Pi_s + \frac{\gamma-1}{\gamma+1}}\right)^{1/2} \tag{3.9}$$

Expansion wave relations:

$$\frac{a_2}{a_1} = 1 \pm \frac{\gamma-1}{2}\frac{u_2 - u_1}{a_1} \tag{3.10}$$

$$\begin{cases} u_{head} = a_1 \pm u_1 \\ u_{tail} = a_2 \pm u_2 \end{cases} \tag{3.11}$$

Where the $\pm$ sign is + when the expansion wave is travelling with the flow and − when the expansion wave is travelling against the flow.

3.2 Analysis steps

This procedure for analysing the wave rotor requires the temperature and pressure of all the ports to be known; the channel length must also be specified. The pressure is assumed to be constant in zones A, B, C1, C2, C3 and D. In other words the pressure does not change at the interface between the L and H fluid. However, the temperature and density is usually different.

The conditions in zone A are assumed to be initially equal to the L port conditions.

3.2.1 Step 1: First Shock Wave

Zones A and B are separated by the shock wave S_1 in the xt diagram. The following assumptions are made: $u_A = 0$, $P_{0A} = P_L = P_{0L}$, $T_{0A1} = T_L = T_{0L}$, $u_H = 0$, $P_{0B} = P_H = P_{0H}$, $T_{0B3} = T_H = T_{0H}$

The conditions in zone B are determined iteratively by the following procedure.

The first step is to assume the pressure ratio Π_{S1}. Then using Equation 3.6 the pressure

P_B is determined with the following equation:

$$P_B = \Pi_{S1} P_A \tag{3.12}$$

After calculating P_B it must be checked that $P_B < P_H$. If this is not the case a smaller Π_{S1} should be assumed.

Now that P_B is known and the flow acceleration from the port into the channel is assumed to be isentropic so the Mach number Ma_B is calculated using Equation 3.3 rearranged:

$$Ma_B = \sqrt{\frac{2}{\gamma - 1}\left(\frac{P_H}{P_B}^{\frac{\gamma-1}{\gamma}} - 1\right)} \tag{3.13}$$

Using Equations 3.4 and 3.1 the speed of sound a_{B3} is determined:

$$\frac{P_2}{P_1} = \left(\frac{a_2}{a_1}\right)^{\frac{2\gamma}{\gamma-1}} \rightarrow a_{B3} = a_H \left(\frac{P_B}{P_H}\right)^{\frac{\gamma-1}{2\gamma}} = \sqrt{\gamma R T_H}\left(\frac{P_B}{P_H}\right)^{\frac{\gamma-1}{2\gamma}} \tag{3.14}$$

As the speed of sound and Mach number is known in zone $B3$ the particle velocity u_B is known though the following equation:

$$u_B = a_{B1} Ma_{B1} = a_{B2} Ma_{B2} = a_{B3} Ma_{B3} \tag{3.15}$$

The last step of the loop is to calculate the pressure ratio Π_{S1} using Equation 3.9 rearranged for Π_{S1}. The assumed Π_{S1} is used on the right hand side of the equation.

$$\Pi_{S1NEW} = 1 + \frac{u_B \gamma}{a_{B3}}\left(\frac{\frac{2\gamma}{\gamma+1}}{\Pi_{S1} + \frac{\gamma-1}{\gamma+1}}\right)^{-0.5} \tag{3.16}$$

Π_{S1NEW} becomes Π_{S1} and calculation process returns to Equation 3.12. This process is repeated until $\Pi_{S1} = \Pi_{S1NEW}$.

Now that Π_{S1} is known the remaining conditions are calculated.

Shock wave velocity:

$$u_{S1_{A1}} = a_{A1}\sqrt{\frac{\gamma+1}{2\gamma}(\Pi_{S1}-1)+1} \tag{3.17}$$

$$u_{S1_{A2}} = a_{A2}\sqrt{\frac{\gamma+1}{2\gamma}(\Pi_{S1}-1)+1} \tag{3.18}$$

Temperature in $B1$ and $B2$ are determined by applying Equation 3.7:

$$T_{B1} = \Pi_{S1}\left(\frac{\frac{\gamma+1}{\gamma-1}+\Pi_{S1}}{1+\frac{\gamma+1}{\gamma-1}\Pi_{S1}}\right)T_{A1} \tag{3.19}$$

$$T_{B2} = \Pi_{S1}\left(\frac{\frac{\gamma+1}{\gamma-1}+\Pi_{S1}}{1+\frac{\gamma+1}{\gamma-1}\Pi_{S1}}\right)T_{A2} \tag{3.20}$$

The temperature in $B3$ is obtained though Equation 3.2:

$$T_{B3} = \frac{T_H}{1+\frac{\gamma-1}{2}Ma_{B3}^2} \tag{3.21}$$

Speed of sound for $B1$ and $B2$ are found using Equation 3.1:

$$a_{B1} = \sqrt{\gamma R T_{B1}} \tag{3.22}$$

$$a_{B2} = \sqrt{\gamma R T_{B2}} \tag{3.23}$$

The last part of step 1 is to find the opening time of port M. The opening time t_{Mo} is defined by when $S1$ reaches the end of the rotor channel. As the speed of sound could be different in $A1$ and $A2$ the shock velocity will be different accordingly. Hence, the time for the shock to reach $x1$:

$$t_{x1} = t_{Ho} + \frac{x1}{u_{S1_{A1}}} \tag{3.24}$$

And the time for the shock to reach the end of the channel:

$$t_{Mo} = t_{x1} + \frac{l - x1}{u_{S1_{A2}}} \tag{3.25}$$

3.2.2 Step 2: First Expansion Wave

The second step is to calculate the property changes over the first expansion wave E_1. As the expansion wave travels at the speed of sound with respect to the particle velocity, its velocity will be different in the three sub zones as the speed of sound changes. The following assumptions are made: $P_{0M} = P_M = P_{C3} = P_{C2} = P_{C1}$.

The change in properties across expansion wave E_1 is assumed to be isentropic and the pressure behind the wave is assumed to be equal to the static pressure of the medium pressure port.

The speeds of sound for zone C is found using Equation 3.4 rearranged:

$$a_{C1} = a_{B1} \left(\frac{P_M}{P_{B1}} \right)^{\frac{\gamma-1}{2\gamma}} \tag{3.26}$$

$$a_{C2} = a_{B2} \left(\frac{P_M}{P_{B2}} \right)^{\frac{\gamma-1}{2\gamma}} \tag{3.27}$$

$$a_{C3} = a_{B3} \left(\frac{P_M}{P_{B3}} \right)^{\frac{\gamma-1}{2\gamma}} \tag{3.28}$$

The particle velocity in zone C is found using Equation 3.10 rearranged:

$$u_{C1} = \frac{2a_{B1} - 2a_{C1} + (\gamma - 1)\, u_{B1}}{\gamma - 1} \tag{3.29}$$

$$u_{C2} = \frac{2a_{B2} - 2a_{C2} + (\gamma - 1)\, u_{B2}}{\gamma - 1} \tag{3.30}$$

$$u_{C3} = \frac{2a_{B3} - 2a_{C3} + (\gamma - 1)\, u_{B3}}{\gamma - 1} \tag{3.31}$$

The Mach number for each sub-zone is also found:

$$Ma_{C1} = u_{C1}/a_{C1} \tag{3.32}$$

$$Ma_{C2} = u_{C2}/a_{C2} \tag{3.33}$$

$$Ma_{C3} = u_{C3}/a_{C3} \tag{3.34}$$

Lastly the temperatures are determined for each respective sub-zone using Equation 3.5 rearranged:

$$T_{C1} = T_{B1}\left(\frac{a_{C1}}{a_{B1}}\right)^2 \tag{3.35}$$

$$T_{C2} = T_{B2}\left(\frac{a_{C2}}{a_{B2}}\right)^2 \tag{3.36}$$

$$T_{C3} = T_{B3}\left(\frac{a_{C3}}{a_{B3}}\right)^2 \tag{3.37}$$

Now that the conditions are known in zones B and C, the velocity of expansion wave $E1$ can be determined.

The interface between $B3$ and $B1$ at the time t_{Mo} is defined by:

$$x_2 = u_{B3}\left(t_{Mo} - t_{Ho}\right) \tag{3.38}$$

Similarly the interface between $B1$ and $B2$ at the time t_{Mo} is defined by:

$$x_3 = u_{B2}\left(t_{Mo} - t_{x_1}\right) + x_1 \tag{3.39}$$

The time for the head of expansion wave $E1$ from the medium port to x_5 is:

$$t_{x_5} = \frac{l - x_3}{a_{B2}} \tag{3.40}$$

The head of expansion wave $E1$ crosses the interface between $B1$ and $B2$ at:

$$x_5 = l - t_{x_5}\left(a_{B2} - u_B\right) \tag{3.41}$$

The time for the head of expansion wave $E1$ from the x_5 to x_4 is:

$$t_{x_4} = \frac{x_3 - x_2}{a_{B1}} \tag{3.42}$$

The head of expansion wave $E1$ crosses interface $B2$ and $B3$ at:

$$x_4 = x_5 - t_{x_4}\left(a_{B1} - u_B\right) \tag{3.43}$$

lastly the closing time of the H port can be calculated:

$$t_{Hc} = t_{Mo} + t_{x_5} + t_{x_4} + \frac{x_4}{a_{B3} - u_B} \tag{3.44}$$

The tail of expansion wave $E1$ reaching the left end of the channel defines the opening of the L port.

The process of determining the tail speed is similar to the head. The particle speed increases linearly from the head to the tail of the wave hence, the average particle speed is used for the tail calculations.

The time for the tail of expansion wave $E1$ from the medium port to x_5 is:

$$t_{x_5t} = \frac{l - x_3}{a_{C2}} \tag{3.45}$$

The tail of expansion wave $E1$ crosses the interface between $B1$ and $B2$ at:

$$x_{5t} = l - t_{x_5t}\left(a_{B2} - \frac{u_{B2} + u_{C2}}{2}\right) \tag{3.46}$$

The time for the tail of expansion wave $E1$ from the x_5 to x_4 is:

$$t_{x_4 t} = \frac{x_3 - x_2}{a_{C1}} \tag{3.47}$$

The tail of expansion wave $E1$ crosses the interface between $B2$ and $B3$ at:

$$x_{4t} = x_{5t} - t_{x_{4t}} \left(a_{C1} - \frac{u_{C3} + u_{B3}}{2} \right) \tag{3.48}$$

Now finding the opening time of port L:

$$t_{Lo} = t_{Mo} + t_{x_{5t}} + t_{x_{4t}} + \frac{x_{4t}}{a_{C3} - u_{C3}} \tag{3.49}$$

The tail speed and time of expansion wave $E1$ is approximate as the particle speeds in $C1$, $C2$ and $C1$ are all different and hence, the interface positions are not simple to calculate in a precise manner.

3.2.3 Step 3: Second Expansion Wave

The second expansion wave $E2$ head reaching the end of the right hand side of the channel defines the closing of the medium port. The left hand side of the channel where the head of $E2$ crosses $E1$ is appropriately referred to by Anderson (1990) as the "Non-simple region". For the purpose of this analysis, the conditions in this region will be taken as the average of the left end of the channel and at x_6. The expansion wave $E2$ is assumed to only travel into zone $C3$. The tail of $E2$ is ignored. The following assumption is also made: $u_{C4} = 0$.

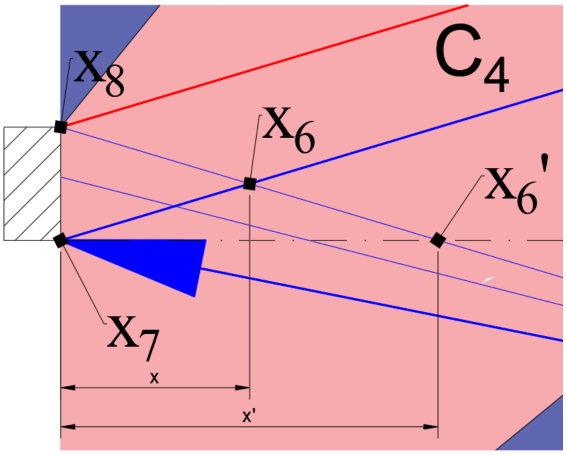

Figure 3.2: Non-simple region

Figure 3.2 show the non-simple region in more detail and provides additional nomenclature. The zone between x_7 and x_6 will be referred to as x.

$$a_x = \frac{a_{B3} + a_{C3}}{2} \tag{3.50}$$

$$u_x = \frac{u_B + u_{C3}}{2} \tag{3.51}$$

$$x' = \left(t_{Hc} - t_{Mo} - t_{x_{5t}} - t_{x_{4t}}\right)(a_{C3} - u_{C3}) \tag{3.52}$$

$$\frac{x' - x}{u_{E2_{tail}}} = \frac{x}{a_x + u_x} \rightarrow x = \frac{x'}{1 + \frac{u_{E2_{tail}}}{a_x + u_x}} = \frac{x'}{1 + \frac{a_{C3} - u_{C3}}{a_x + u_x}} \tag{3.53}$$

Now the time for the head of $E2$ to reach x_6 can be found:

$$t_x = \frac{x}{u_x + a_x} \tag{3.54}$$

And lastly the closing time of M port:

$$t_{Mc} = t_{Mc} + t_x + \frac{l - x}{u_{C3} + a_{C3}} \tag{3.55}$$

As the flow speed behind the expansion wave $E2$ is assumed to be zero the conditions in zone $C4$ can be obtained.

Using Equation 3.10 rearranged:

$$a_{C4} = a_{C3} - \frac{(\gamma - 1)\, u_{C3}}{2} \tag{3.56}$$

Using Equation 3.1 rearranged:

$$T_{C4} = \frac{a_{C4}^2}{\gamma R} \tag{3.57}$$

And using Equation 3.4 rearranged:

$$P_{C4} = P_{C3} \left(\frac{a_{C4}}{a_{C3}} \right)^{\frac{2\gamma}{\gamma - 1}} \tag{3.58}$$

3.2.4 Step 4: Second shock wave

The process for determining the properties of $D1$, $D2$ and the shock speed is the same as step 1.

$$P_D = \Pi_{S2} P_{C4} \tag{3.59}$$

After calculating P_D it must checked that $P_D < P_L$. If this is not the case a smaller Π_{S2} should be assumed.

$$Ma_{D1} = \sqrt{\frac{2}{\gamma - 1} \left(\frac{P_L}{P_D}^{\frac{\gamma - 1}{\gamma}} - 1 \right)} \tag{3.60}$$

Using Equation 3.4 and 3.1 the speed of sound a_{B3} is determined:

$$a_{D1} = \sqrt{\gamma R T_L}\left(\frac{P_D}{P_L}\right)^{\frac{\gamma-1}{2\gamma}} \tag{3.61}$$

As the speed of sound and Mach number is known in zone $B3$ the particle velocity u_B is known though the following equation:

$$u_D = a_{D1} Ma_{D1} \tag{3.62}$$

The last step of the loop is to calculate the pressure ratio Π_{S1} using Equation 3.9 rearranged for Π_{S1}. The assumed Π_{S1} is used on the right hand side of the equation.

$$\Pi_{S2NEW} = 1 + \frac{u_D \gamma}{a_{C4}}\left(\frac{\frac{2\gamma}{\gamma+1}}{\Pi_{S2} + \frac{\gamma-1}{\gamma+1}}\right)^{-0.5} \tag{3.63}$$

Π_{S2NEW} becomes Π_{S2} and calculation process returns to Equation 3.59. This process is repeated until $\Pi_{S2} = \Pi_{S2NEW}$.

Now that Π_{S2} is known the remaining conditions are calculated.

Shock wave velocity:

$$u_{S2} = a_{C4}\sqrt{\frac{\gamma + 1}{2\gamma}\left(\Pi_{S2} - 1\right) + 1} \tag{3.64}$$

Temperature in $D2$ is determined by applying Equation 3.7:

$$T_{D2} = \Pi_{S2}\left(\frac{\frac{\gamma+1}{\gamma-1} + \Pi_{S2}}{1 + \frac{\gamma+1}{\gamma-1}\Pi_{S1}}\right) T_{C4} \tag{3.65}$$

The temperature in $D1$ is obtained though Equation 3.2:

$$T_{D1} = \frac{T_L}{1 + \frac{\gamma-1}{2} Ma_{D1}^2} \tag{3.66}$$

Speed of sound for $D2$ is found using Equation 3.1:

$$a_{D2} = \sqrt{\gamma R T_{D2}} \tag{3.67}$$

3.2.5 Step 5: Third Shock Wave

The third shock wave ($S3$) is shock $S2$ reflected. As the flow behind the reflected shock wave is assumed to be zero, the the pressure ratio can be determined from the following equation:

$$\Pi_{S3} = 1 + \frac{u_D \gamma}{a_{D2}} \left(\frac{\frac{2\gamma}{\gamma+1}}{\Pi_{S3} + \frac{\gamma-1}{\gamma+1}} \right)^{-0.5} \tag{3.68}$$

Equation 3.68 is solved numerically.

Once Π_{S3} is known the wave speed can be calculated with respect to the particle velocity:

$$W_{S3_{D1}} = a_{D1} \sqrt{\frac{\gamma + 1}{2\gamma} (\Pi_{S3} - 1) + 1} \tag{3.69}$$

$$W_{S3_{D2}} = a_{D2} \sqrt{\frac{\gamma + 1}{2\gamma} (\Pi_{S3} - 1) + 1} \tag{3.70}$$

The absolute velocity of the shock wave:

$$u_{S3_{D1}} = W_{S3_{D1}} - u_D \tag{3.71}$$

$$u_{S3_{D2}} = W_{S3_{D2}} - u_D \tag{3.72}$$

The position of the $D1 - D2$ interface at the time t_{Mc}:

$$x_9 = u_{D1} \left(t_{Mc} - t_{Lo} \right) \tag{3.73}$$

Now the time $S3$ takes from the right hand side of the channel to the $D1 - D2$ interface:

$$t_{x1_{D2}} = \frac{l - x_9}{W_{S3_{D2}}} \tag{3.74}$$

The time $D1 - D2$ interface to the left hand side of the channel:

$$t_{x1_{D1}} = \frac{l - u_{S3_{D2}} t_{x1_{D2}}}{u_{S3_{D1}}} \tag{3.75}$$

The closing time of L port can be determined:

$$t_{Lc} = t_{Lo} + \frac{l}{u_{S2}} + t_{x1_{D1}} + t_{x1_{D2}} \tag{3.76}$$

Now all the port opening times are known. The conditions of zone A should be calculated and the procedure from step 1 to this point should be repeated until the solution converges.

Pressure in zone A:

$$P_A = \Pi_{S3} P_D \tag{3.77}$$

Temperature in $A1$ and $A2$ are determined by applying Equation 3.7:

$$T_{A1} = \Pi_{S3} \left(\frac{\frac{\gamma+1}{\gamma-1} + \Pi_{S3}}{1 + \frac{\gamma+1}{\gamma-1} \Pi_{S3}} \right) T_{D1} \tag{3.78}$$

$$T_{A2} = \Pi_{S3} \left(\frac{\frac{\gamma+1}{\gamma-1} + \Pi_{S3}}{1 + \frac{\gamma+1}{\gamma-1} \Pi_{S3}} \right) T_{D2} \tag{3.79}$$

Speed of sound for $B1$ and $B2$ are found using Equation 3.1:

$$a_{A1} = \sqrt{\gamma R T_{D1}} \tag{3.80}$$

$$a_{A2} = \sqrt{\gamma R T_{D2}} \tag{3.81}$$

3.2.6 Mass Flow and Performance

Once a converged solution is obtained, the mass flow for each port can be calculated. The rotor channel cross sectional area is not considered and hence, the mass entering the channel will be expressed per unit area:

$$\frac{m}{A} = \left(PMa\sqrt{\frac{\gamma}{RT}} \right) t \tag{3.82}$$

Where t is the duration for which the channel is open to the port.

The mass entering the H port:

$$\frac{m_H}{A} = \left(P_{B3} Ma_{B3} \sqrt{\frac{\gamma}{RT_{B3}}} \right) [t_{Hc} - t_{Ho}] \tag{3.83}$$

The mass entering the L port:

$$\frac{m_L}{A} = \left(P_{D1} Ma_{D1} \sqrt{\frac{\gamma}{RT_{D1}}} \right) [t_{Lc} - t_{Lo}] \tag{3.84}$$

The mass leaving the channel is:

$$\frac{m_M}{A} = \frac{m_H}{A} + \frac{m_L}{A} \longrightarrow m_M = m_H + m_L \tag{3.85}$$

Now that the mass flow per cycle is known the performance parameter and isentropic efficiency can be determined with the following equations (Kentfield, 1969):

$$\zeta = \frac{m_L T_{0L}}{m_H T_{0H}} \tag{3.86}$$

$$\eta = \zeta \left[\frac{\left(\frac{(P_{M0}}{P_{L0}} \right)^{\frac{\gamma-1}{\gamma}} - 1}{1 - \left(\frac{P_{M0}}{P_{H0}} \right)^{\frac{\gamma-1}{\gamma}}} \right] \tag{3.87}$$

As the ports stagnation temperatures and pressures are assumed to be equal to the static the equations become:

$$\zeta = \frac{m_L T_L}{m_H T_H} \tag{3.88}$$

$$\eta = \zeta \left[\frac{\left(\frac{(P_M}{P_L}\right)^{\frac{\gamma-1}{\gamma}} - 1}{1 - \left(\frac{P_M}{P_H}\right)^{\frac{\gamma-1}{\gamma}}} \right] \tag{3.89}$$

3.2.7 Solution Implantation

The analysis procedure outlined in this chapter has been coded for MATLAB in Appendix 3. The following chapter will focus on the application of the code to develop simulated performance maps.

Chapter 4

1D Performance Mapping Simulation and Validation

Contents

4.1 Simulated Performance Maps

The 1D analysis method described in the previous chapter was developed for estimating the optimal port timing for a given set of port boundary conditions. After developing the analysis method it was realised it could be applied to multiple boundary conditions to simulate a performance map similar to the map published by Kentfield (1969) as duplicated in Figure 4.1.

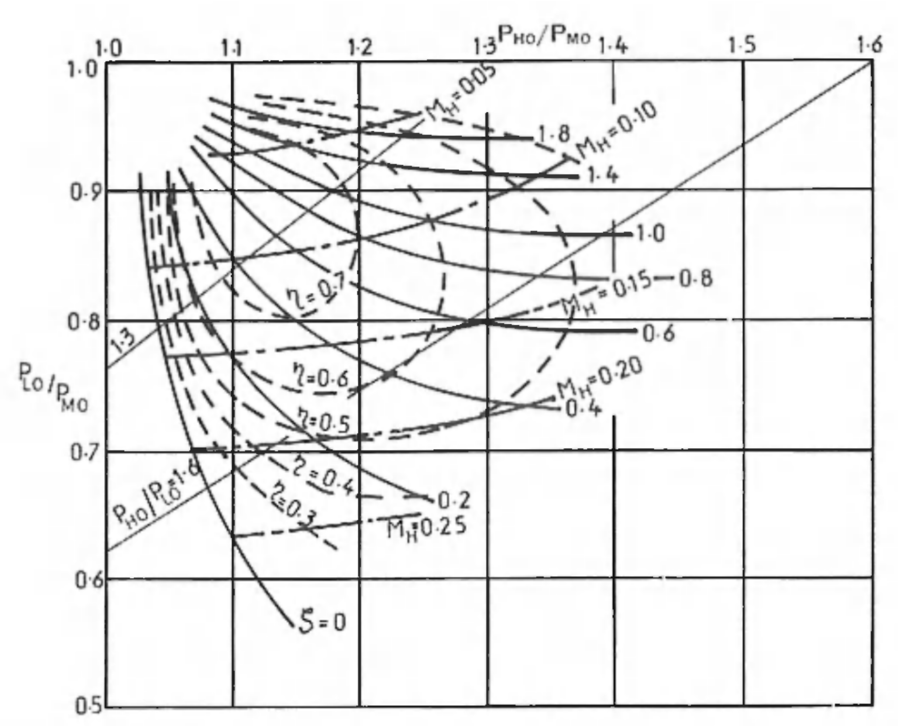

Figure 4.1: Experimental results by Kentfield (1969)

The simulated performance maps illustrated in Figures 4.2 and 4.3 were generated by calculating multiple port pressure ratios and then generating a contour plot from the results. The temperature in this case was assumed to be 300 K for all three ports.

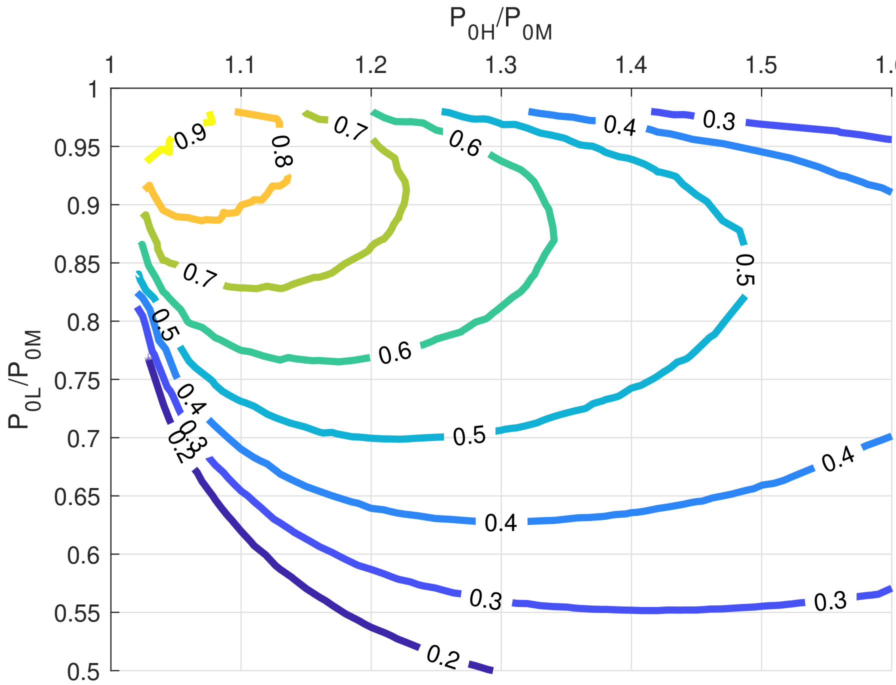

Figure 4.2: Simulated isentropic efficiency η

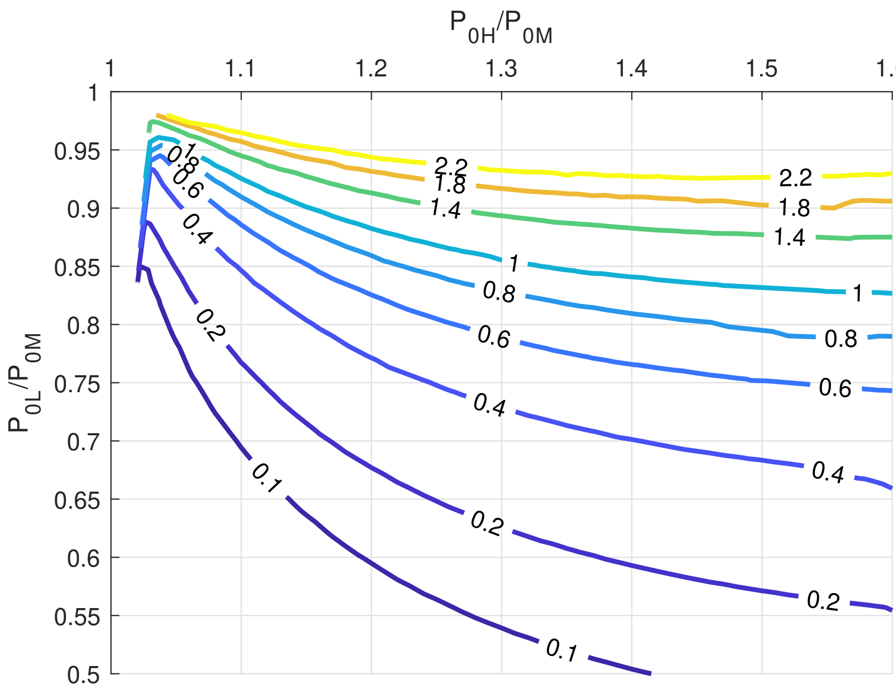

Figure 4.3: Simulated performance parameter ζ

4.2 Validation

Considering the simplifications and assumptions made during the 1D analysis method, the simulated result from the precent work and the experimental results published by Kentfield (1969) have extremely good correlation. Comparing this more closely, the simulated maps have been overlaid on the Kentfield (1969) experimental results in Figure 4.4. As one can see in Figure 4.4b both experimental and simulated ζ contour lines line up precisely for P_{0H}/P_{0M} ratios up to 1.3, but at higher ratios, the results do not line up as closely. The simulated and experimental η in Figure 4.4a is not in as good agreement as ζ however, it follows the trend very closely.

One should keep in mind that the simulated performance maps are generated assuming optimal porting for each given pressure ratio, whereas the experimental results are derived from a fixed geometry tested over the mapped range. This will explain some of the miss-match between experimental and simulated performance maps.

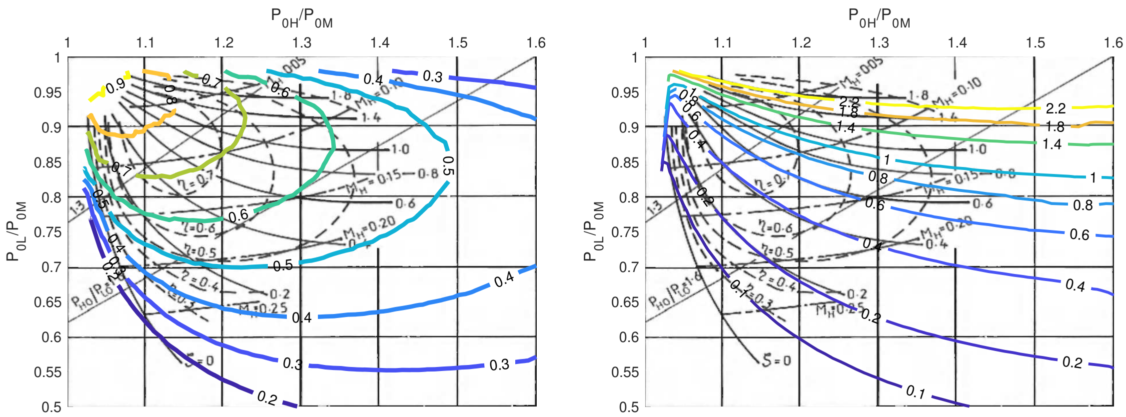

(a) Isentropic efficiency η validation (b) Performance parameter ζ validation

Figure 4.4: Simulated maps overlaid on the Kentfield (1969) experimental results

The maps are intended to give an indication of an expected value for ζ and η. The more important output from the 1D analysis is correct port timings so CFD geometries can be generated for more rigorous analysis or to aid device design directly. The port timing derived from the present 1D analysis was validated using CFD. Figure 4.5 illustrates the CFD pressure contour results. Shock and expansion waves are identifiable by the sudden change in pressure. The locations of these waves are within a reasonable agreement with the port opening and closing. Details of the CFD methodology and further results are reported in later chapters.

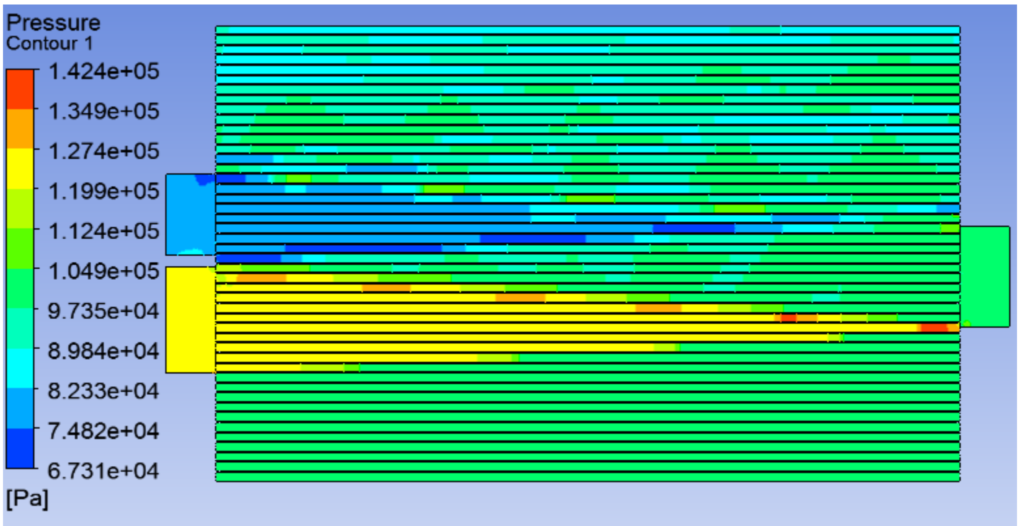

Figure 4.5: CFD pressure contour

4.2.1 Limitations

Although the simulated performance maps presented above have a very good correlation with the experimental results published by Kentfield (1969) there are several limitations with this analysis method. In addition to the assumptions described in the previous chapter, heat transfer from the channel walls, gradual port opening and viscous effects are all neglected. Furthermore simulating suboptimal port timing for the device is also not possible. Hence, each specified boundary condition set is simulated assuming the optimal port geometry is being used.

When developing the analysis method the assumption was made that all the fluid entering the device would leave within one rotor rotation. This assumption did not affect the results simulated in this work as the temperature differences were relatively small. However, eliminating this assumption would make the method more robust and would allow large port temperature difference to be accurately simulated.

Chapter 5

PEEWR Commissioning and Experimental Testing Methodology

Contents

5.1 Commissioning Notes

5.1.1 Assembling the Rotor and Casing

The inner part of the rotor was machined by cutting axial slots along the outer circumference as pictured in Figure 5.1. The outer sleeve was then machined with an inner diameter 0.2 mm smaller than the main rotor part outer diameter. The two rotor parts where then assembled by freezing inner part and heating the sleeve so they could be slipped together. The rotor was them dynamically balanced. The balancing correction was reactively small only requiring 3 grams to be removed from each end of the rotor.

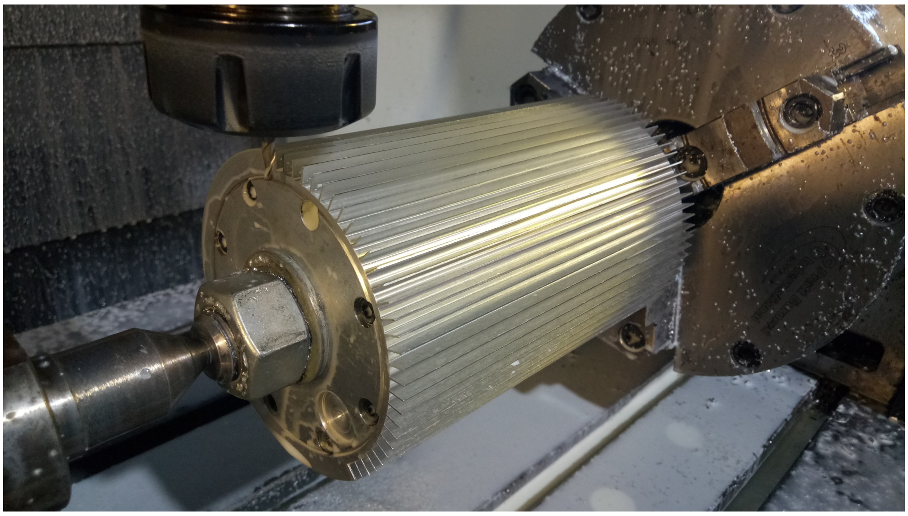

Figure 5.1: Rotor Machining (Blyth, personal communication, 2019)

The rotor and casing was assembled as shown in Figure 5.2. A selection of different thickness shims was used to adjust the position of the end plates so the rotor would rotate freely with a minimal gap.

5.1.2 Port Clearance

The rotor surface depth from the end plate was measured using a depth micrometer. The axial end float was measured with a dial gauge as shown in Figure 5.3. The ports were then 3D printed with the required dimensions so they touched the rotor end. From here the ports were fitted and then the rotor was rotated to see where they were touching. The ports were then disassembled and sanded to remove the marks left by the rotor. This process was repeated until the rotor cleared the port surface at all angles of rotation. This ensured the gap between the ports and rotor was as small as possible.

5.1.3 Test Rig Configuration

The original test rig setup used the hypersonic wind tunnel dump tanks at USQ. The dump tanks are large vacuum tanks pumped down to approximately 1 kPa absolute pressure. The combined volume of the dump tanks is 12.5 cubic meters. The medium pressure

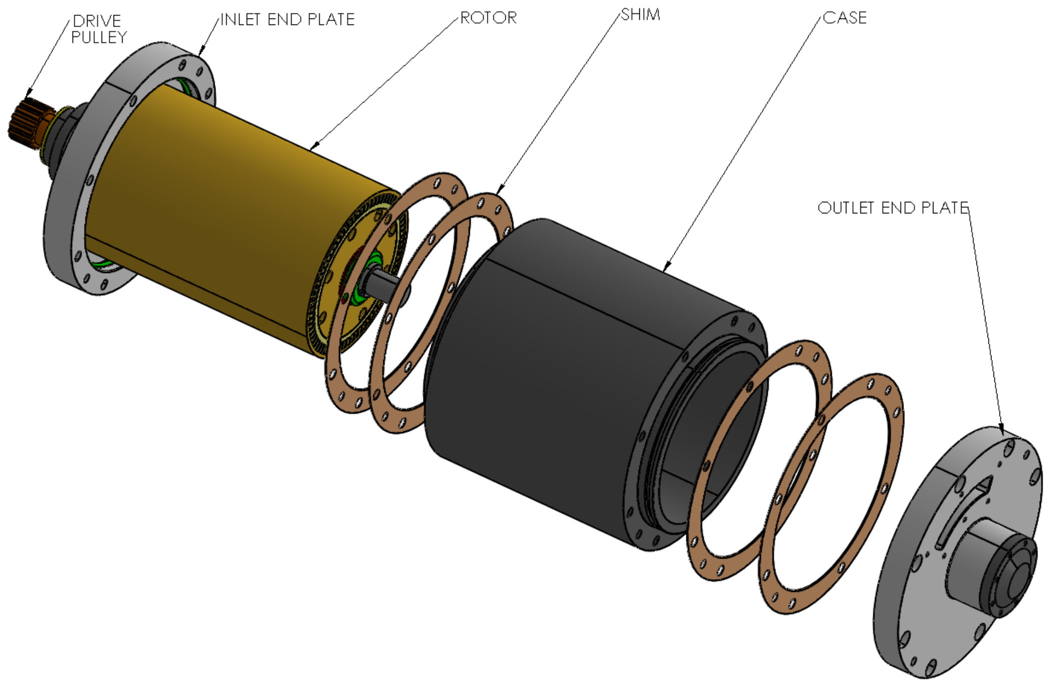

Figure 5.2: Assembling rotor in casing

port was connected to the dump tanks as shown in Figure 5.4. An inline gate valve was used to adjust the pressure seen by the PEEWR. The low pressure port was connected to a mass flow controller which throttled atmospheric air to a lower pressure by restricting suction caused by the PEEWR. The high pressure port was supplied by atmospheric air. This method was used as the original ports were 3D printed plastic and it was deemed to be safer to test the rig under vacuum rather than pressure.

The results measured using this setup were poor with a maximum isentropic efficiency of only 17.8% (Kentfield (1969) recoded a maximum of 70%). It was thought that the low efficiency was a result of the testing method rather than the device itself. The low pressure port depends on the suction from the PEEWR to lower the pressure below the high pressure port. However, on start up of the PEEWR the low and high pressure ports are at the same pressure, which means the device may not be getting to the optimal operating cycle. In other words, there is no direct control of the boundary conditions with the original setup. Proving this explanations is difficult without testing the device with more control over the boundary conditions. Hence, it was decided to redesign the ports to allow for testing the device under pressure, which would eliminate the start up port pressure issues.

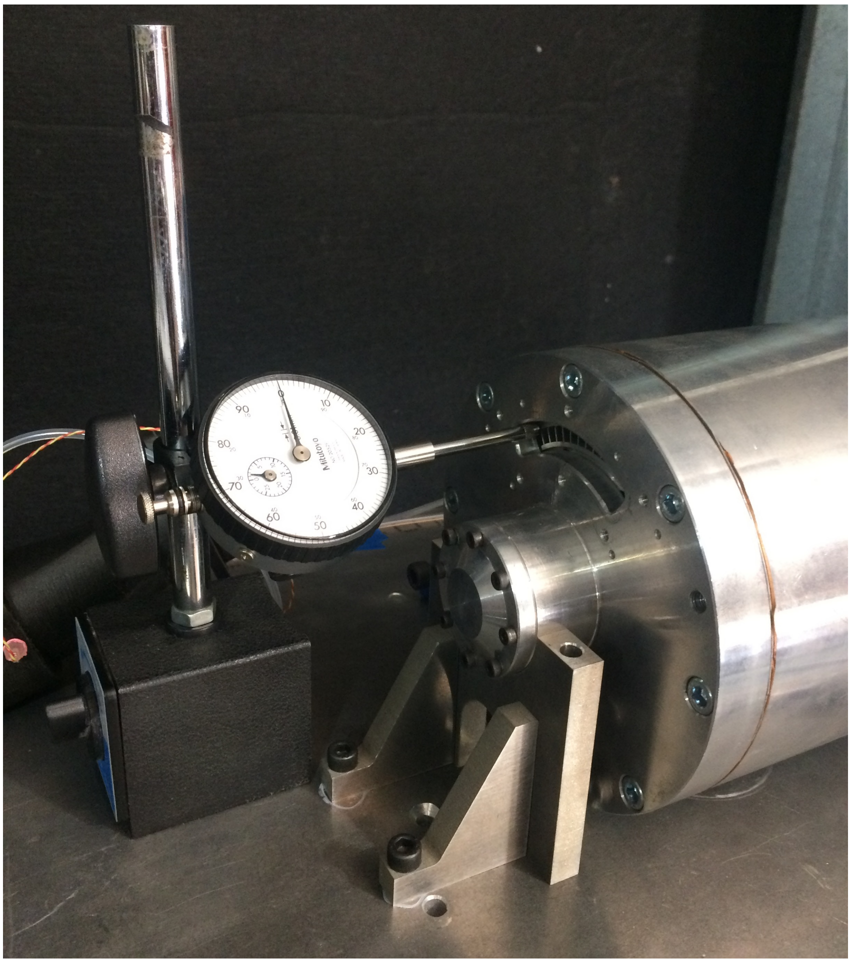

Figure 5.3: Measuring required port depth with dial gauge

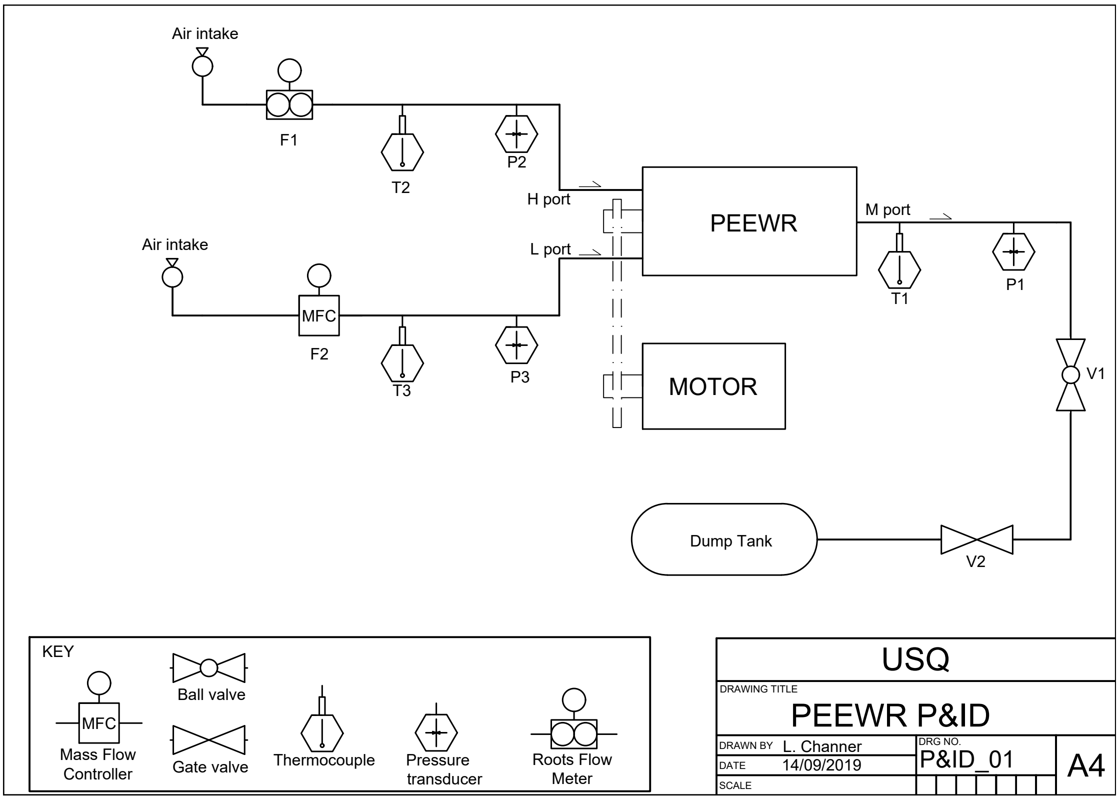

Figure 5.4: Piping and instrumentation diagram setup one

The design of the new ports is discussed in the following section. The P&ID of the updated rig is illustrated in Figure 5.5. The electric motor is three phase and controlled by a variable frequency drive (VFD). The electric motor was fitted with an encoder (note encoder not shown in P&ID) so the PEEWR rotor speed can be monitored by the data acquisition system. The motor speed is controlled manually by changing the frequency output of the VFD.

5.1.4 Porting Redesign

The main objectives for redesigning the ports was to ensure they would be suitable for withstanding moderate pressures while maintaining the flexibility of adjusting port timing. The chosen design is illustrated in Figure 5.6. The copper pipes and brass flange were soldered together forming the pressure containing part of the port. The 3D printed adaptor slips inside the copper and recessed part of the flange creating a transition from the round pipe to the required slot for port timing. This design allows for the 3D printed adaptor to be easily changed, hence the port timing is adjustable by modifying the adaptor design and reprinting. The ‘O’ring is used to seal between the PEEWR case, adaptor and brass flange. The port clearance was adjusted with the same method as discussed in

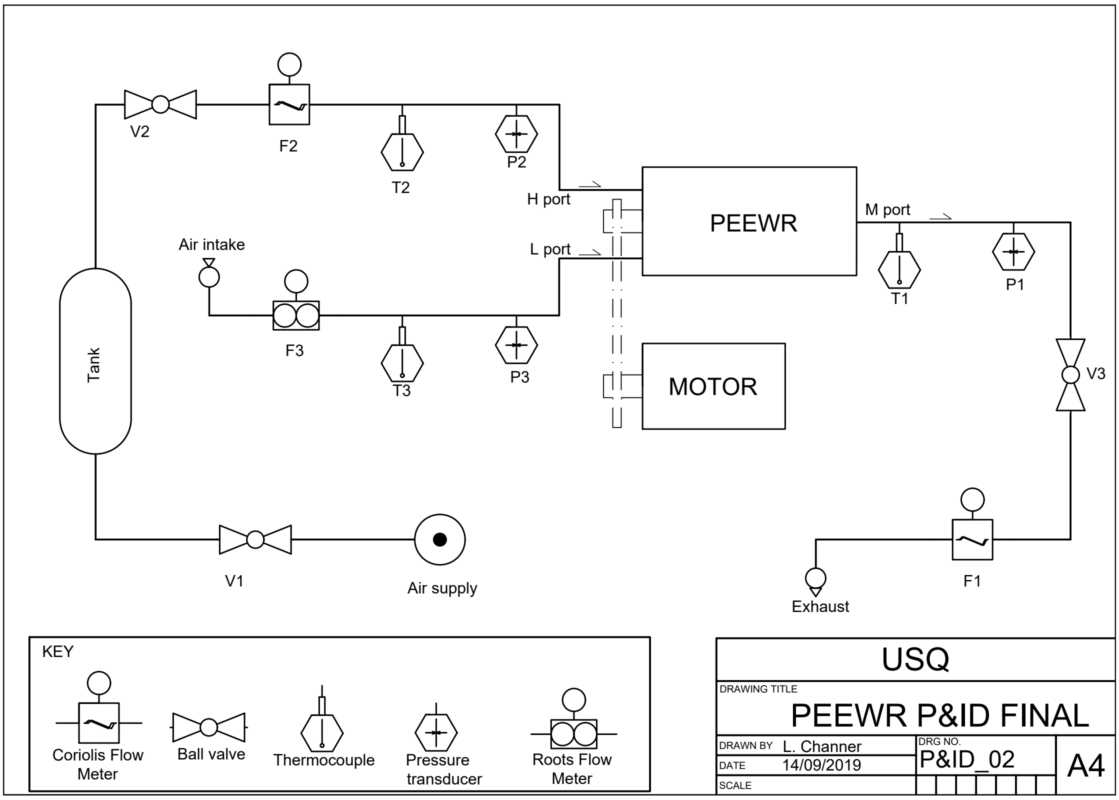

Figure 5.5: Piping and instrumentation diagram setup two

section 5.1.2.

5.2 Experimental Testing Methodology

The experimental methodology was developed around the instrumentation available at TUSQ Hypersonic Laboratory and the literature on testing wave rotors.

5.2.1 Instrumentation and Data Acquisition System

All the instrumentation was configured to be read by the data acquisition system. This allowed for regular readings and eliminated the possibility of errors associated with taking manual readings. The following sections will discuss the instrumentation used in the final setup of the test rig as presented in Figure 5.5

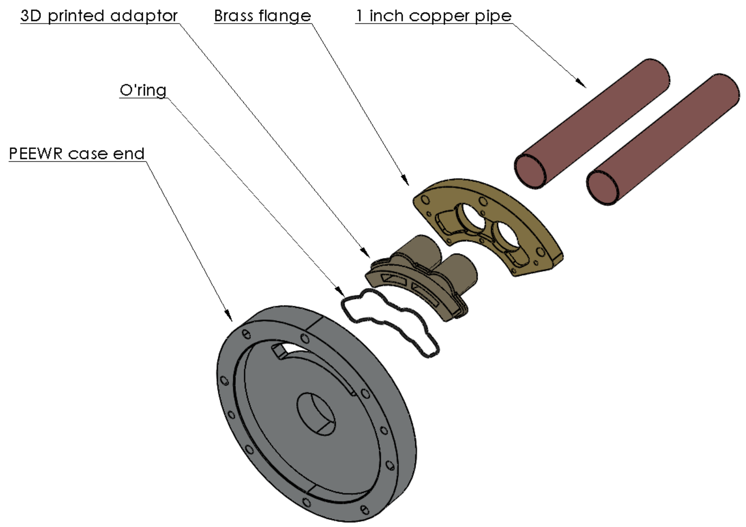

Figure 5.6: Redesigned porting

Flow Meters

The mass flow in the high and medium pressure ports was measured using Coriolis flow meters. The low pressure port mass flow was deduced as the difference of the high and medium pressure port flows. The low pressure also had a positive displacement roots flow meter which was left over from earlier setups of the test rig. This flow meter was only used as a cross check on the deduced flow rate based on the other ports as it measures volumetric flow rate which requires conversion to a mass flow rate. To convert the volumetric flow to mass flow the temperature and pressure is needed. As these are not measured directly at the flow meter there is an associated error in the mass flow rate measured by the roots flow meter.

Coriolis mass flow meters were selected based on their wide operating range and high accuracy. Also, their compatibility with the data acquisition system and availability at TUSQ was an advantage. For the high pressure port a Yokogawa rotaMASS RCCF31 was used while a Siemens Sitrans FC430 was used for the medium pressure port. The roots flow meter used on the low pressure port was a Romet RM85.

Thermocouples

The thermocouples used for measuring the flow temperature in each port was the K type variant. The end of the thermocouple was held in the flow by gluing it into a threaded

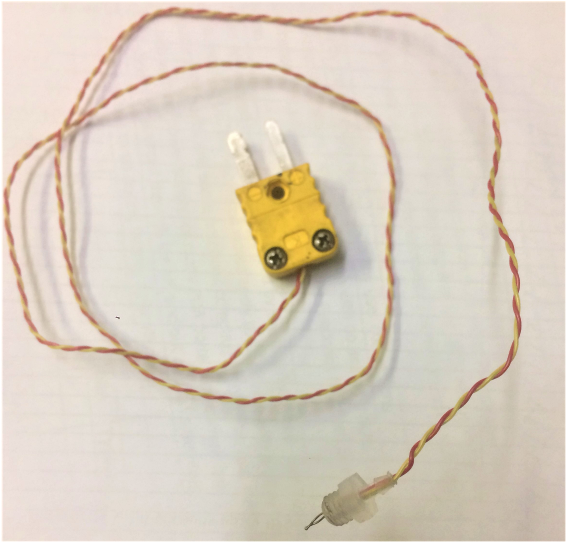

Figure 5.7: K type thermocouple

nipple as depicted in Figure 5.7. The nipple was threaded into the port tapping boss (see Figure 5.8).

All the thermocouples were connected to an amplifying IC which converts the voltage change seen across the thermocouple to an output where 0V equals 0 degrees Celsius and for example 0.2V equals 20 degrees Celsius.

Pressure Transducer

The pressure of each port was measured using XTL-190-3.5 Kulite absolute pressure transducers. The transducers were threaded into an acrylic manifold which was connected to the pressure tappings on the ports though a piece of 2 mm lab hose. The transducers were connect to the data Acquisition via a 100 gain amplifier.

Encoder

The electric motor shaft speed was measured with a 360 pulse per rotation Kubler 05.2400 encoder. This was connected directly to the data acquisition system. The belt drive connecting the motor to the wave rotor had a two to one pulley ratio hence the rotor shaft speed is twice the electric motor shaft speed.

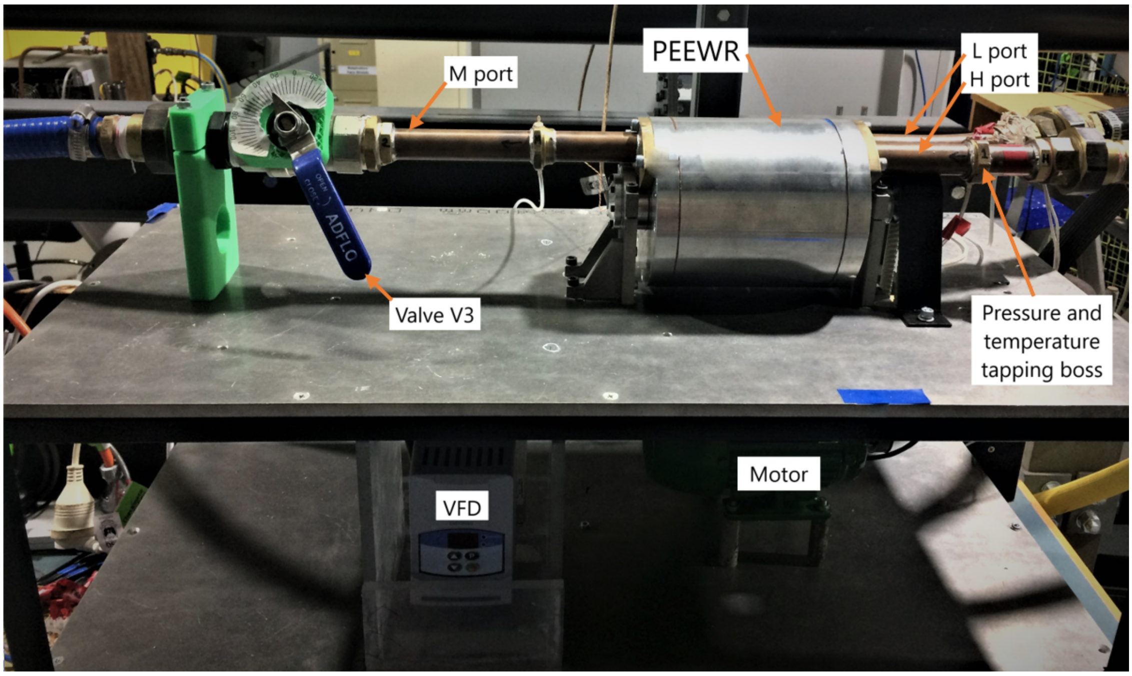

Figure 5.8: Test rig photo

Data Acquisition

The data acquisition system used was a LabJack U6. The U6 is an USB 14 channel analogue input plus two pulse counter DAQ. The system writes a .dat file directly to the computer's hard drive which can be read by MATLAB while being written. Each reading is given an absolute time stamp. During the testing of the device data was recorded every 500 ms.

5.2.2 Testing Procedure

Before the performance tests were performed, the local atmospheric pressure was measured using the barometer in the laboratory. Also, the instrumentation was calibrated. This was done by utilising the automatic zeroing mode in the Coriolis flow meters. The pressure transducers were calibrated by recoding a data file before the tests which was used as the zero gauge pressure readings.

The testing procedure used is as follows:

1. Referring to Figure 5.5, valve V1 is opened allowing air to fill the tank.

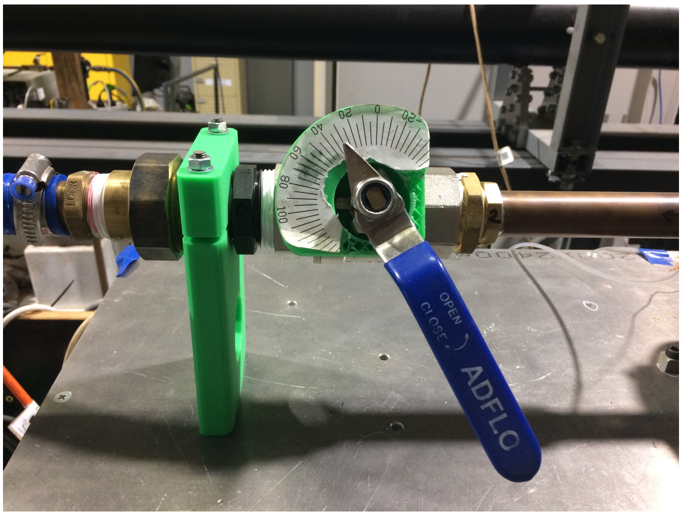

Figure 5.9: Medium pressure port valve 3 with scale for setting

2. The motor is switched on and the rotor is allowed to reach the desired operating speed.

3. On opening valve V2, high pressure flows can be supplied to the PEEWR. As the tank empties the pressure drops, hence, the high pressure port is supplied with a range of pressure over time. This is useful for supplying higher flow rates than possible from the laboratory air supply connected directly to the PEEWR.

4. Once the pressure in the tank has dropped the system is shutdown and valve V3 is adjusted to change the back pressure on the medium pressure port of the PEEWR. Valve V3 is depicted in Figure 5.9.

5. The process is repeated at multiple valve V3 settings.

5.2.3 Post Processing

The post processing was carried out in MATLAB. The data collected by the LabJack were voltage readings and number of pulses, hence, the first step in post processing was to convert these into recognisable quantities. Once this had been done the performance parameter and efficiency was by calculated with the following equations (Kentfield, 1969):

$$\zeta = \frac{m_L T_{0L}}{m_H T_{0H}} \tag{5.1}$$

$$\eta = \zeta \left[\frac{\left(\frac{(P_{M0}}{P_{L0}}\right)^{\frac{\gamma-1}{\gamma}} - 1}{1 - \left(\frac{P_{M0}}{P_{H0}}\right)^{\frac{\gamma-1}{\gamma}}} \right] \tag{5.2}$$

Where other quantities were derived from isentropic relations (Kentfield, 1969):

$$P_0 = P^{\frac{-1}{\gamma-1}} \left[P + \left(\frac{\gamma - 1}{2\gamma}\right) \frac{\dot{m}^2}{\rho A_{port}^2} \right]^{\frac{\gamma}{\gamma-1}} \tag{5.3}$$

The density was calculated using the ideal gas law:

$$\rho = \frac{P}{RT} \tag{5.4}$$

The stagnation temperature was found using the following isentropic relation:

$$\frac{T_0}{T} = \left(\frac{P_0}{P}\right)^{\frac{\gamma-1}{\gamma}} \tag{5.5}$$

During testing, the data being recoded was plotted (see Figure 5.10) so it could be visually validated with the digital displays on the Coriolis flow meters and the expected trend of the data. Referring to Figure 5.10a, the low pressure port deduced flow rate was visually validated with the Romet measured flow rate.

As one can see from Figure 5.10 the flow meter and temperature data is quite noisy, hence, ζ and η were smoothed in MATLAB using the Savitzky-Golay filtering function. Filtering was done with great care to avoid distortion of the data. As one can see from Figure 5.11, it was found filtering in multiple steps, gradually widening the filtering window was more effective while not distorting the data. Applying the final window width to the raw data directly is shown in Figure 5.11d for comparison with the stepped method.

Filtering the mass flow and temperature data before calculating the efficiency and performance parameter is another option. However, it was more convenient to filter the

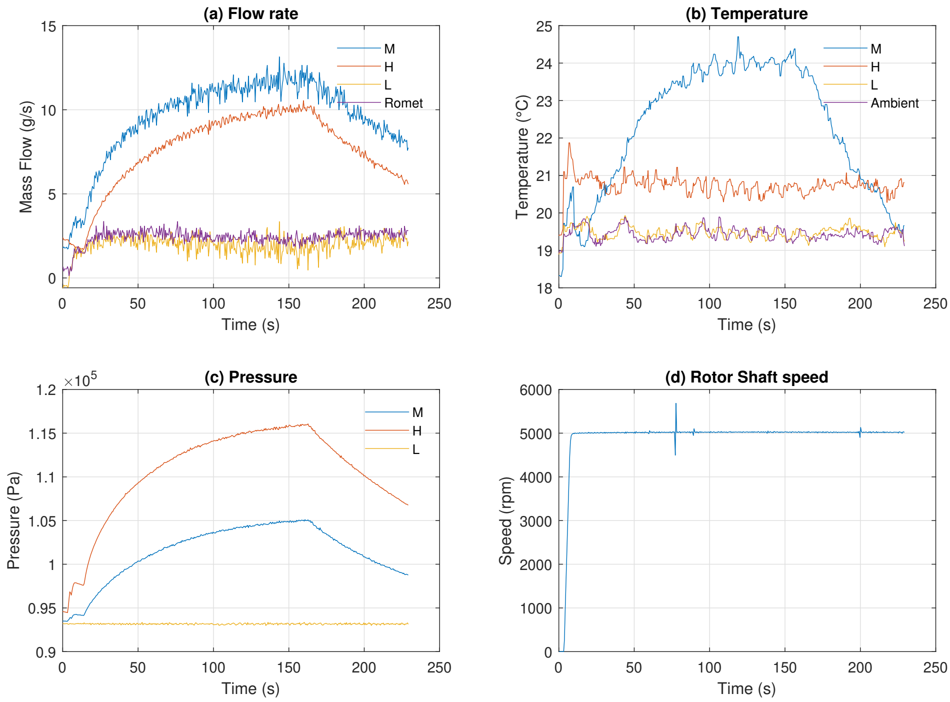

Figure 5.10: Example of fundamental data plots obtained during experiments

efficiency and performance parameter and keep the mass flow and temperature in raw form.

After filtering the efficiency and performance parameter, the data is shown in Figure 5.12. Finally the data is clipped to exclude the period when the rotor is getting up to speed and an output file is written containing the decoded data. This process was carried out for all the performance tests recorded and the data was used to generate the plots presented in the following chapter.

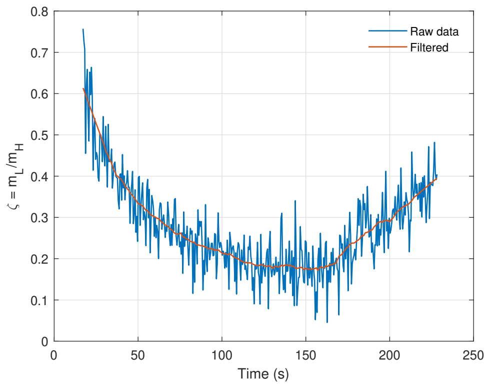

(a) Fist stage filtering

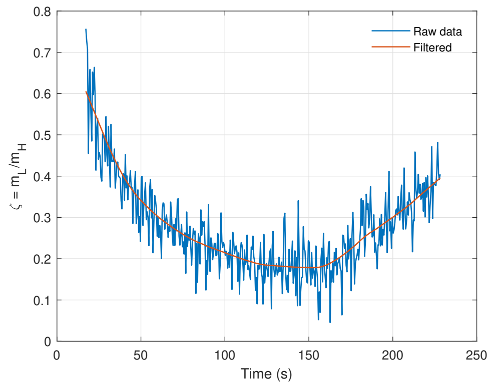

(b) Second stage filtering

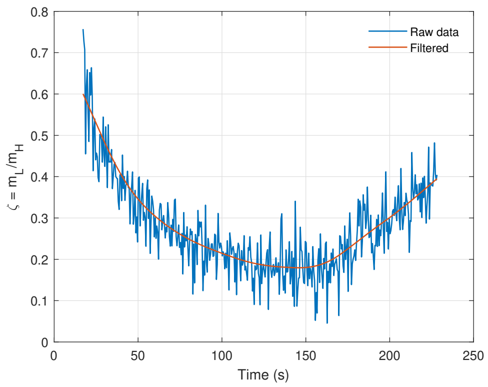

(c) Third stage filtering

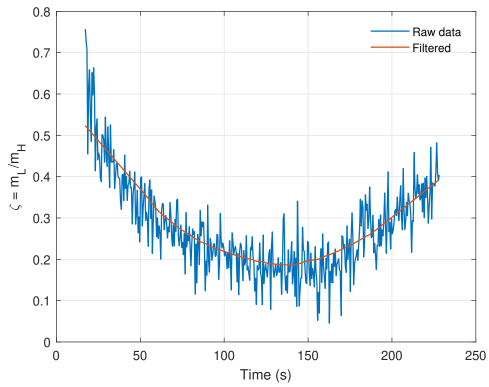

(d) All three sages applied in one go

Figure 5.11: Illustration of filtering affect on performance parameter ζ

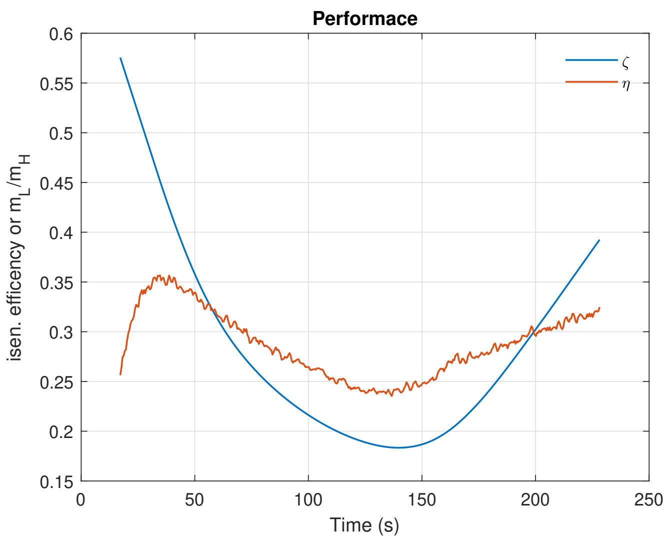

Figure 5.12: Example of derived data plots obtained during the experiments

Chapter 6

PEEWR Experimental Results and Discussion

Contents

This chapter presents and discusses the experimental results of the PEEWR tested as part of this work.

The PEEWR performance parameter ζ is used extensively in the following work and is defined by:

$$\zeta = \frac{\dot{m}_L T_{0L}}{\dot{m}_H T_{0H}} \tag{6.1}$$

The variation of the absolute temperature in experimental data was less than 3% therefore, ζ is effectively defined by the mass flow rates. As one can see from the above equation the larger ζ is the better the performance as more low pressure fluid is entrained relative to the amount of high pressure driving fluid being used.

The higher the isentropic efficiency η the better and this parameter is calculated based on ζ and the pressure of each port with the following equation:

$$\eta = \zeta \left[\frac{\left(\frac{(P_{0M}}{P_{0L}}\right)^{\frac{\gamma-1}{\gamma}} - 1}{1 - \left(\frac{P_{0M}}{P_{0H}}\right)^{\frac{\gamma-1}{\gamma}}} \right] \tag{6.2}$$

The pressure ratios P_{0L}/P_{0M} and P_{0H}/P_{0M} are also important as they indicate how much pressure boosting of the low pressure port and how much pressure is being used from the high pressure port. The lower the P_{0L}/P_{0M} and P_{0H}/P_{0M} ratios the better the performance of the device.

In summary, high values of ζ and η and low values of P_{0L}/P_{0M} and P_{0H}/P_{0M} should be targeted for optimal PEEWR operation.

6.1 Results

6.1.1 Performance Parameter and Efficiency

The experimental results presented in this section are at the design speed of the rotor of 5000 rpm. In the following section, rotor speed variation and its effects on performance are presented.

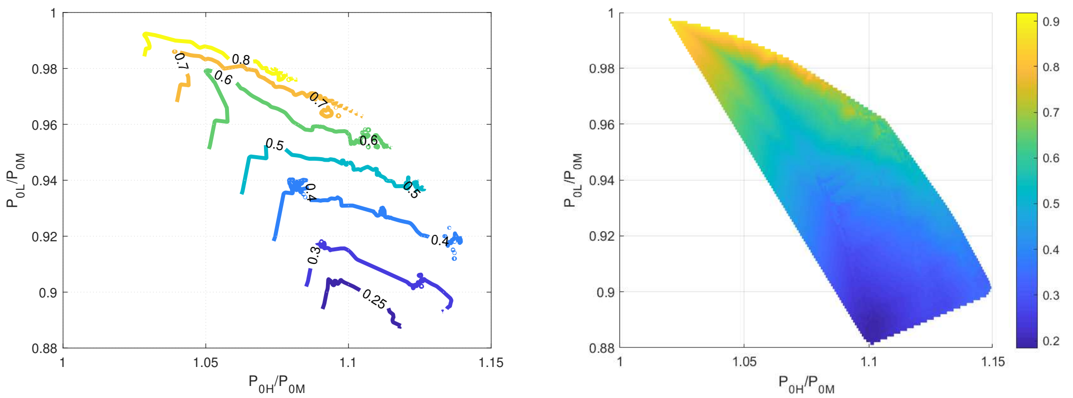

(a) ζ contour plot

(b) ζ surface plot

Figure 6.1: Performance parameter distribution from present experiments

The ζ and η contour plot lines in Figures 6.1 and 6.2 are not very smooth, hence the surface plots have also been provided as an alternative form of presentation. The efficiency and performance parameter results published by Kentfield (1969) were previously included in Figure 4.1 and can be used for comparison.

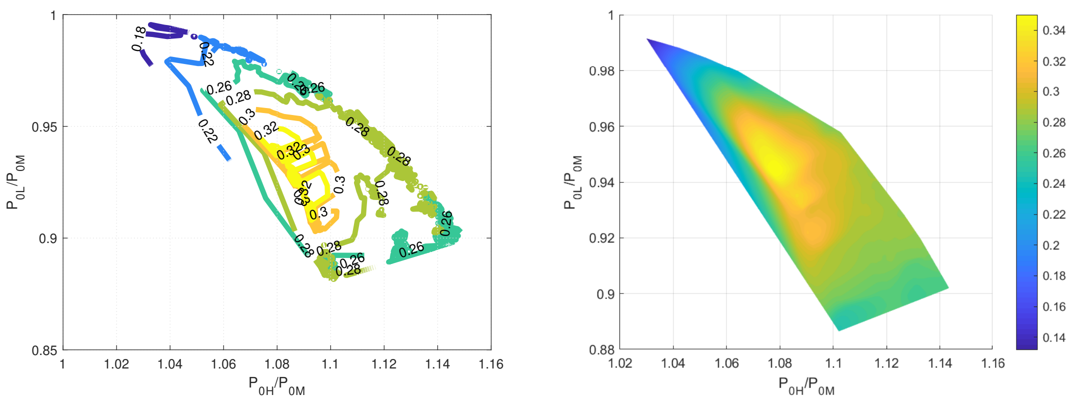

(a) η contour plot

(b) η surface plot

Figure 6.2: Efficiency distribution from present experiments

The experimental isentropic efficiency and performance parameter results obtained as part of this work (Figures 6.1 and 6.2) are substantially lower than published by Kentfield (1969) (Figures 4.1). Also the low pressure port boosting is very low compared to Kentfield (1969). Despite this the general trend of the results are similar which is encouraging.

6.1.2 Rotor Speed Variation

The results published by Kentfield (1969) also included the contour plot presented in Figure 6.3 illustrating how the performance parameter changes with rotor speed. This plot was for a fixed pressure ratio $P_{0H}/P_{0L} = 1.3$. As this pressure ratio was not achieved in the experimental data acquired in this work the equivalent plot has been created for a fixed pressure ratio $P_{0H}/P_{0L} = 1.2$ and presented in Figure 6.4. The trend of performance parameter with rotor speed in Figure 6.4 is very similar to Figure 6.3. The change in ζ is small at different rotor speeds, however, it does follow expectations by having the best P_{0L}/P_{0ML} at the design speed of 5000 rpm.

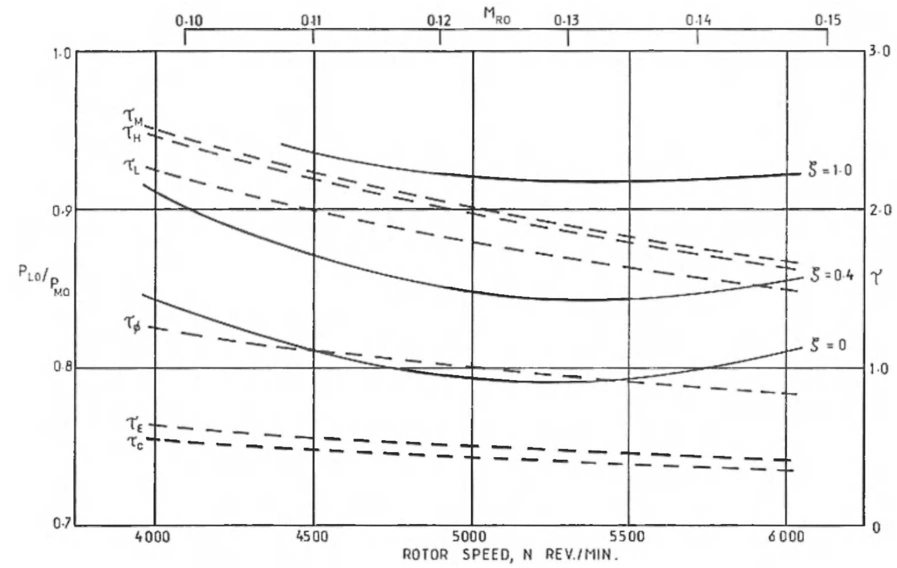

Figure 6.3: Performance (ζ) variation with rotor speed for $P_{0H}/P_{0L} = 1.3$ from Kentfield (1969)

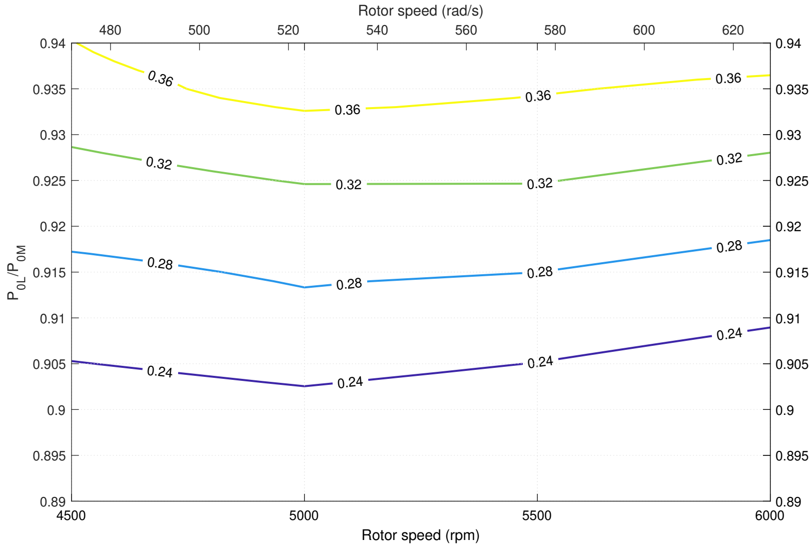

Figure 6.4: Performance (ζ) variation with rotor speed for $P_{0H}/P_{0L} = 1.2$ from present experiments

Building on the above, we can look at the change in isentropic efficiency with rotor speed. Figure 6.5 illustrates how the efficiency is much more sensitive to changes in rotor speed than the performance parameter shown in Figure 6.4. This highlights the importance of operating at the rotor design speed for maximum efficiency.

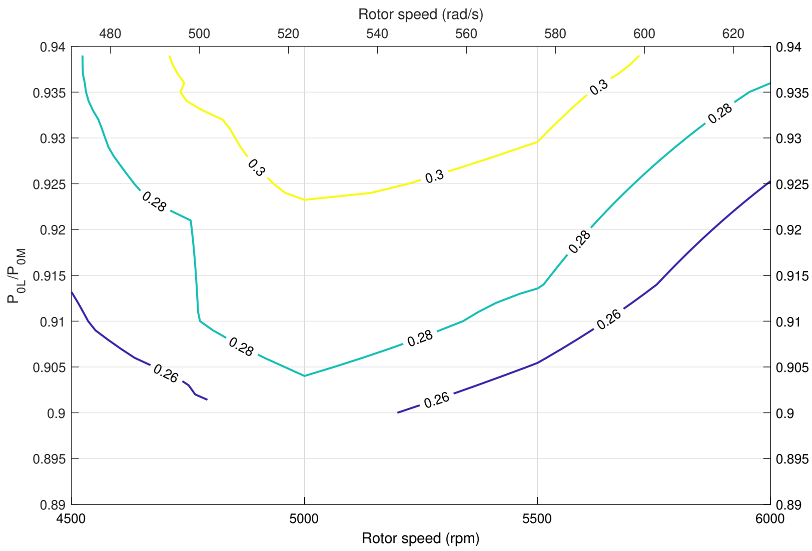

Figure 6.5: Efficiency (η) variation with rotor speed for $P_{0H}/P_{0L} = 1.2$ from present experiments

6.1.3 Pressure and Mass Flow Rate Plots

Results presented in the previous sections are useful for comparing with Kentfield (1969) results. However, as they are in dimensionless form, some information is lost. The plots in this section present the results in a more specific form to the PEEWR used in the experimental testing.

The low pressure port intake is directly from the atmosphere, therefore the port pressure remains relatively constant. The high pressure port's pressure is varied over the duration of a test, therefore it is convenient to make it the independent variable for plotting performance curves.

The mass flow rate data is quite noisy. Therefore, to make the results easier to read, regression lines have been applied to both the mass flow rate and pressure data as illustrated in Figure 6.6.

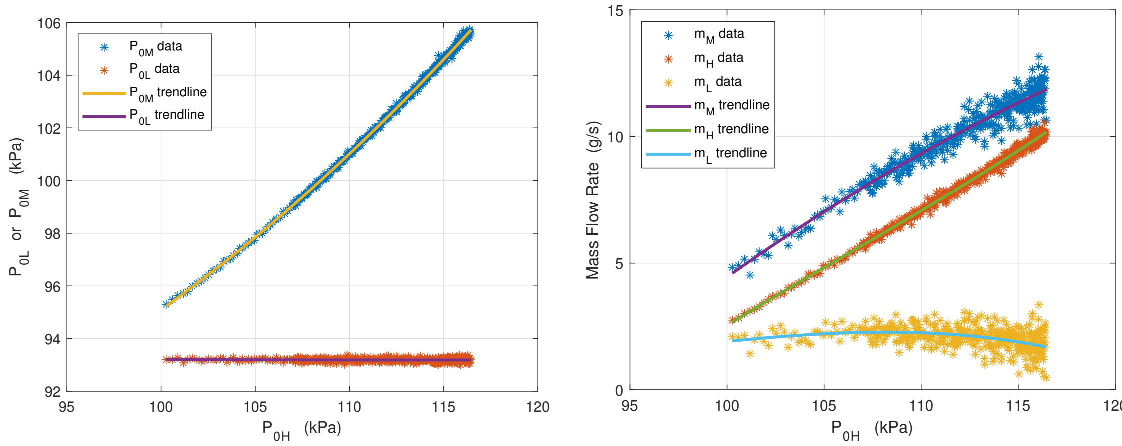

(a) Pressure (b) Mass flow rate

Figure 6.6: Pressure and mass flow rate trendlines for valve setting of 30°

The low pressure port mass flow rate is deduced from the measured high and medium pressure port flow rates. Therefore, the trendline for the low pressure port mass flow rate presented in Figure 6.6b is the difference between the high and medium pressure port trendlines rather than a best fit for the calculated low pressure mass flow data points.

The port pressures and mass flow rates have been plotted together in Figure 6.7a. From these trendlines the performance parameter ζ and isentropic efficiency η have been calculated and plotted along with port pressure in Figure 6.7b.

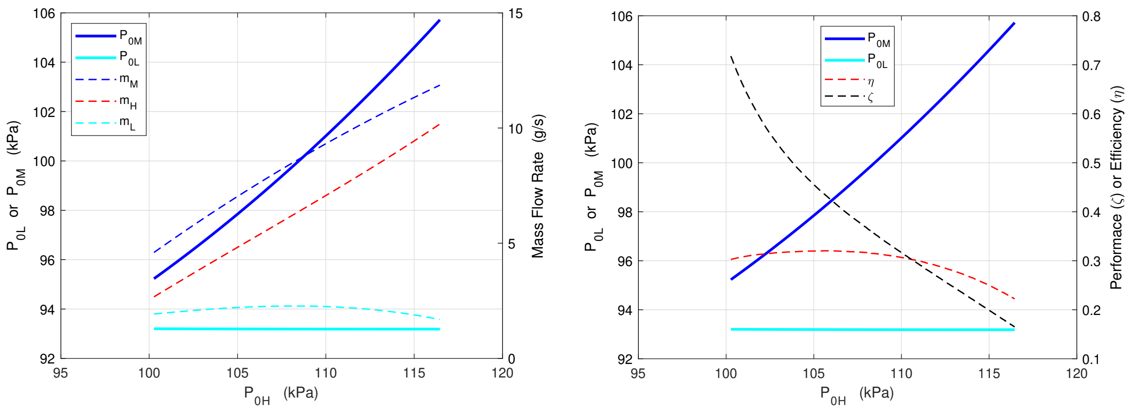

(a) Port mass flow rate and pressure (b) ζ, η and port pressure

Figure 6.7: Performance curves for valve setting of 30°

The results presented in Figure 6.6 and 6.7 are for a medium pressure port valve setting (refer to Figure 5.5). The valve setting is given in degrees of the ball valve handle on the medium pressure line (i.e valve setting 0° = *closed* and 90° = *open*). Equivalent plots to Figures 6.6 and 6.7 for other valve settings are included in Appendix C. Results recorded with 80° valve setting has been included in Figure 6.8 for comparison with the 30° valve setting results in Figure 6.7.

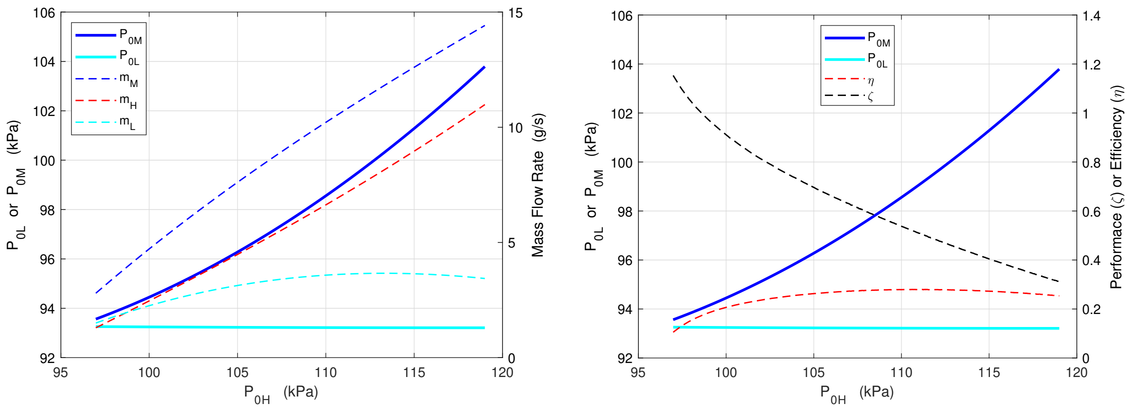

(a) Port mass flow rate and pressure (b) ζ, η and port pressure

Figure 6.8: Performance curves for valve setting of 80°

From the Figures 6.7 and 6.8 it can be noted that with a lower medium port back pressure relative to P_{0H} the mass flow rate increases in each port. Also, efficiency and performance parameter changes less relative to P_{0H}. However, maximum values of these quantities are higher with a larger back pressure on the medium pressure port.

6.2 Discussion

The experimental PEEWR performed well below expectations. Multiple possibilities could contribute to the differences but the reason for the differences between theoretical and observed performance requires further investigation. Literature identifies wave rotors are susceptible to losses though the following: heat transfer, rotor rotational friction (i.e. air and bearing resistance) and end plate leakage (Wilson, 1998; Wilson & Fronek, 1993). Porting angles have also been identified to influence efficiency (Paxson & Wilson, 1995). According to Wilson (1998) and Wilson and Fronek (1993) leakage is the largest inefficiency in wave rotors by a significant margin. Results presented by Wilson and Fronek (1993) identified reducing the clearance from 0.5 mm to 0.125 mm increased the wave rotor efficiency by 8%.

Table 6.1: PEEWR channel dimension comparisons

PEEWR	Rotor diameter (mm)	Channel width (mm)	Channel height (mm)	Channel length (mm)	Rotor design speed (rpm)
Power Jets (tested by Kentfield (1969))	165	15	55	279	5500
USQ	90	3.5	5	150	5000

Azoury (1965) provided some details on the device tested by Kentfield (1969). As presented in Table 6.1 the channel size of the PEEWR tested as part of this work is significantly smaller than the PEEWR tested by Kentfield (1969). Therefore, the percentage of cross sectional area affected by boundary layers will be much higher in the present work. Also, based on pictures published in Azoury (1965) the port piping is estimated to be 120 mm in diameter compared to 25 mm in the present work.

End plate leakage, suboptimal porting angles and viscus losses are likely to be significant contributors to the lack of performance. With the aid of CFD, suboptimal porting angles and viscous losses are investigated and discussed further in Chapter 8. Quantifying the losses through end plate leakage is outside the scope of this work, but remains a topic deserving further investigation.

6.2.1 Uncertainty

The instrumentation measurement uncertainty was evaluated by referring to the respective manuals and specification sheets. The relative uncertainty was also considered by comparing the readings at the same conditions as plotted in Figure 6.9.

It should be noted that the difference in port conditions is what is being investigated, hence it is more important that the instrumentation read the same relative to one another than the absolute value in this case.

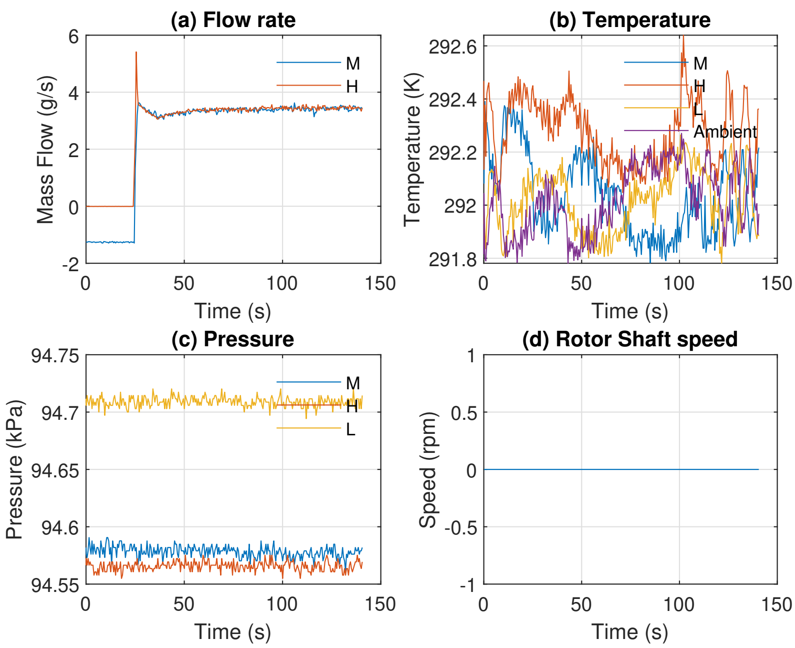

Figure 6.9: Instrumentation readings and nominal operating conditions

Pressure Transducers

The pressure transducer specification sheet gives a typical full scale error of 0.1% and a maximum of 0.5%. The full scale pressure rating is 3.5 bar where the typical operating pressure was closer to 1.1 bar. Therefore, the maximum uncertainty at 1.1 bar would be: $3.5 \times 0.5/1.1 = 1.59\%$ and the typical $3.5 \times 0.1/1.1 = 0.32\%$.

From the data presented in Figure 6.9, the relative uncertainty is estimated to be $\pm 0.097\%$. As explained in Chapter 5 the pressure data is calibrated. Hence, the uncertainty can be confidently taken as $\pm 0.1\%$.

Mass Flow Meters

The Coriolis flow meter manuals for the Yokogawa rotaMASS RCCF31 specifies the uncertainty as:

$$E = \pm 0.5 \pm \frac{0.02361}{\dot{m}(g/s)} \times 100\%$$

Evaluating this at a typical mass flow rate of 8 g/s the uncertainty is:

$$E = \pm 0.5 \pm \frac{0.02361}{8} \times 100\% = \pm 0.795\%$$

Similarly the Siemens Sitrans FC430 manual specifies the uncertainty as:

$$E = \pm\frac{0.0556}{\dot{m}} \times 100\%$$

At 8 g/s the uncertainty is:

$$E = \pm\frac{0.0556}{8} \times 100\% = \pm 0.695\%$$

The relative uncertainty was determined by connecting both flow meters in series. From the data in Figure 6.9 the relative uncertainty is estimated to be ±0.69%

Thermocouples

Standard K type thermocouples have a specified maximum error of ±2.2 °C. This may appear to be high, however, as we are dealing with absolute temperatures, this translates to $2.2/292 \times 100 = \pm 0.75\%$ at the typical operating temperature. The relative temperature uncertainty is estimated to be ±0.058%. In both cases this is well below 1%.

Overall Results Uncertainty

The total uncertainty of the results has been estimated using the root mean square error propagation method defined by the following equation (Cooper R J & G, 2006):

$$E_P = \sqrt{\sum_{i=1}^{n} \left(E_1^2 + E_2^2 + \ldots + E_n^2\right)} \tag{6.3}$$

where E_P = probable range in error (±%), n = total number potential error sources and E_1, E_2, E_n = potential error source (±%).

Equation 6.2 defining η is not a simple relation. Hence, strictly speaking the root mean square method illustrated in Equation 6.3 should not be applied directly to the pressures when estimating the uncertainty in the case of η. However, as the equation is raising the pressures to a value less than one, the sensitivity to changes in pressure are reduced. Therefore, applying the root mean squared method directly will give conservative estimation of the total uncertainty of the η results.

There are eight main sources of uncertainty: two flow meters, three thermocouples and three pressure transducers. Evaluating this using Equation 6.3:

$$E_P = \sqrt{3 \times 0.1^2 + 0.795^2 + 0.695^2 + 3 \times 0.75^2} = 1.683\%$$

therefore, the overall results uncertainty is estimated to be less than 2%.

6.2.2 Limitations and Issues

The test rig and instrumentation performed reasonably well. However, several improvements would be beneficial for future experimental tests.

The Coriolis mass flow meter data was very noisy (electrical). Improving this would improve the quality of the data. The mass flow rate been measured was on the lower end of the Coriolis meters' range. Despite this the flow meters performed reasonably well. Referring to Figure 6.6b, the high pressure port mass flow rate data is more compressed around the trend line than the medium port data. This could be attributed to the Coriolis flow meter on the high pressure port been a slightly smaller capacity meter or a more superior device. The high pressure port mass flow rate was measured using the Yokogawa rotaMASS RCCF31, while the medium pressure port was measured using the Siemens Sitrans FC430.

The laboratory air supply was on the smaller end of the required capacity. A larger air supply would allow for testing the device over a larger range of pressure ratios.

Due to the low experimental efficiency and compression relative Kentfield (1969) the focus of this work shifted to investigating the possible causes via computational analysis.

Chapter 7

PEEWR Computational Fluid Dynamics Methodology

Contents

This chapter is dedicated to reporting the computational fluid dynamics methodology developed for analysing the PEEWR. The software used was ANSYS Fluent, which was selected based on availability, past experience using the ANSYS environment and reported use in wave rotor research (Chan et al., 2017; Iancu et al., 2005, 2008).

Both three dimensional (3D) and two dimensional (2D) simulations have been undertaken. The methodology used was similar therefore, unless otherwise specified, the following information will be relevant to both 3D and 2D simulations.

The methodology for simulating the PEEWR was first considered as part of an assignment project undertaken for a CFD course completed at USQ. Refer to Appendix E for more details. The method used in this assignment was very basic and limited to one channel. The channel was simulated in 2D and porting achieved by changing the ends of the channel from wall to pressure inlet/outlet depending on the time step. The methodology used in the assignment did work and the computational cost was low, however it neglected some major aspects such as gradual port opening. It also required a lot of post processing to present the results in a form which could be understood. Therefore, the methodologies discussed here were developed to analyse the PEEWR with more rigour.

7.1 Geometry

The 3D geometry was created in SOLIDWORKS as an assembly. Whereas the 2D geometry was created using DesignModeler within the ANSYS environment. The geometry is based on the PEEWR used in the experimental testing or is based on the port timing calculated using the 1D analysis method developed in Chapter 3. See Figure 7.1 for wave rotor geometries.

7.1.1 Zone Naming

The rotor channels and ports are all assigned a zone name (this can be done in DesignModeler or ANSYS Meshing). This enables the rotor to be defined in Fluent as rotating and allows for patching so a steady solution is achieved more efficiently. See port naming in Figure 7.1.

7.1.2 Boundary Conditions

For the boundary condition types to be correctly assigned automatically when the model is loaded into Fluent, the relevant faces must be defined with the correct name selection. The ends of the channels are named: ‘Rotor In Interface’ and ‘Rotor Out Interface’ respectively. Similarly the contacting face of the ports are named: ‘Stator In Interface’ and ‘Stator Out Interface’. This creates an interface boundary condition between the stator and rotor faces. The inlet and outlet faces on the ports are named as relevant (e.g. ‘L inlet’). The remaining unnamed faces were named as ‘rotor wall’ and ‘stator wall’ depending on the face.

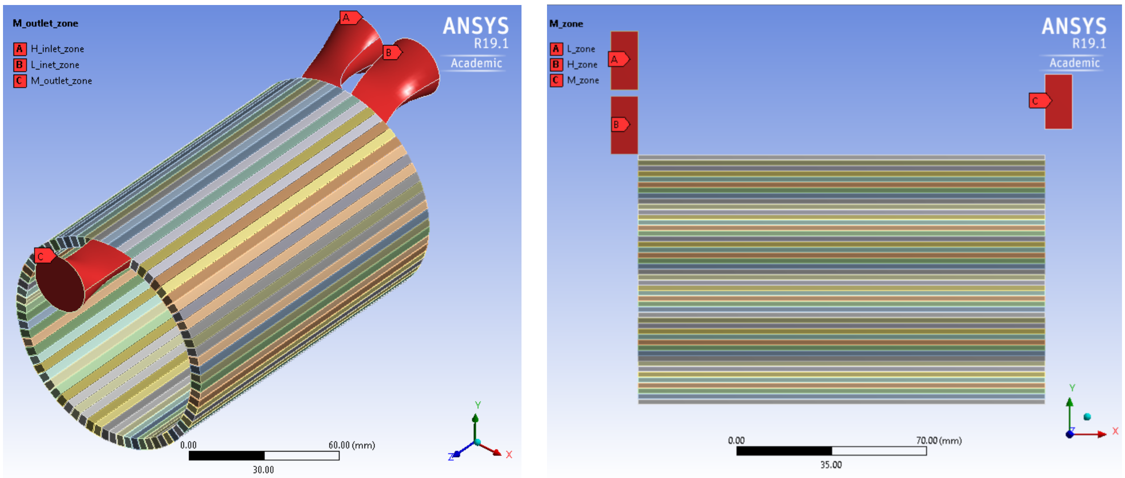

(a) 3D (b) 2D

Figure 7.1: Example geometries

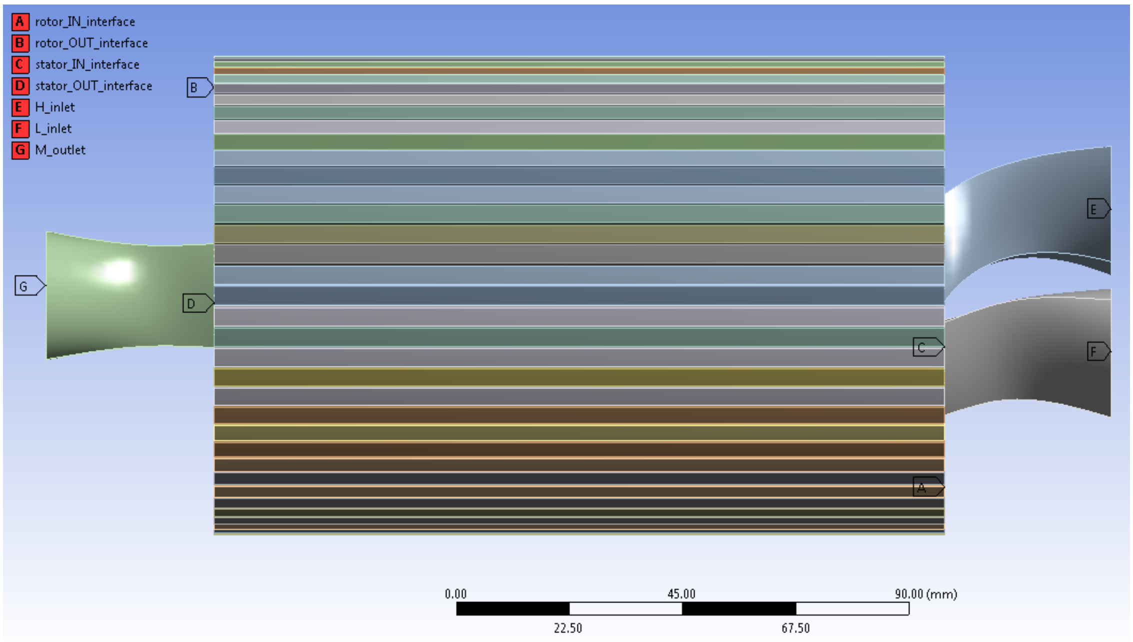

Figure 7.2: Boundary condition naming

7.2 Meshing

Before meshing the contacts are defined between the contacting surfaces. This is important to define so all the channel ends are treated as interfaces. The contacts are defined by inserting a ‘manual contact region’ under the connections tree in ANSYS Meshing. Taking advantage of the name selections defined earlier, the contact is set to ‘Stator In Interface’ and the Target as ‘Rotor In Interface’. Similarly a separate contact is defined for the outlet interfaces.

The 2D mesh was generated by defining the maximum element size and adding a 3× mesh refinement at the interfaces between the ports and rotor channels. This gave a good quality hexa element mesh. The 3D mesh was also mainly hexa elements; in some cases the ports were meshed as tetrahedral elements if the quality was too low using hexa elements, in which case a Multi Zone method was used. Refining the 3D mesh at the interfaces is not possible with hexa elements. It was found to be more element/node efficient to refine the whole hexa mesh than having a tetrahedral mesh with refinements at the interfaces between the ports and rotor channels. Hexa elements are preferable for numerical stability and reduced element count which leads to reduced computational cost.

The mesh quality was assessed by skewness and orthogonal quality. The criteria used for a good quality mesh was minimum orthogonal quality > 0.1 and maximum skewness < 0.95.

The mesh element size is a balance between computational cost and resolving the shock and expansions waves. Smaller element size would resolve the moving shock and expansion waves further within the rotor channels. However, the smaller the mesh the smaller the time step and a finer mesh takes longer to solve and causes an increase in the computational cost. The exact size of the elements was determined through the mesh independence studies which is discussed in the following sections. 0.5 mm was found to be a reasonable element size for the cases simulated. See Figure 7.3 for typical meshes.

7.3 Simulation Setup

The simulation setup was carried out in Fluent on a desktop computer. For large simulations the first time step was solved and then transferred to the university’s high powered computer (HPC). A code template for transferring the desktop case file to the HPC is attached in Appendix D.

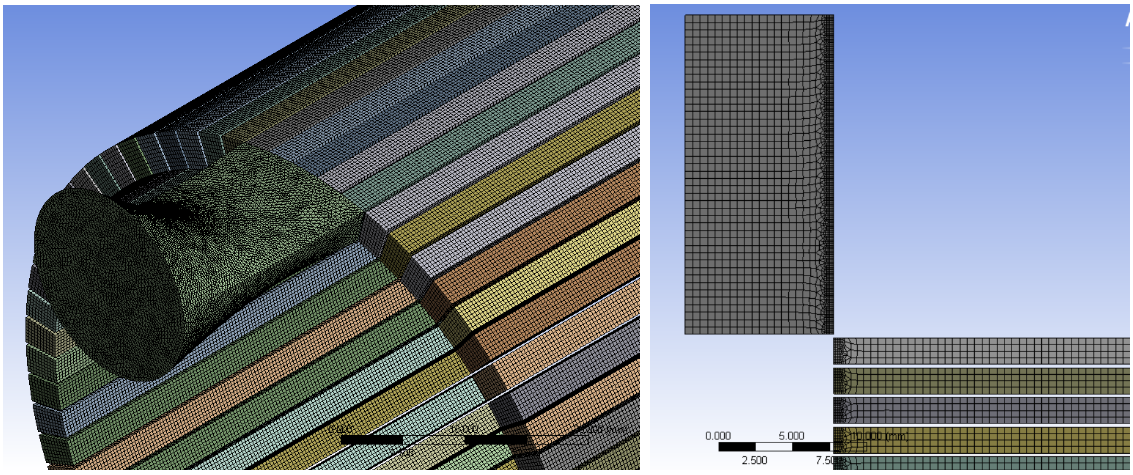

(a) 3D (b) 2D

Figure 7.3: Sample meshes

7.3.1 Setup Procedure

The setup inside Fluent was as follows: the solver was set to density-based and transient. The model was set to inviscid with energy on. An inviscid model was selected for the following reasons: reduced computational cost, correlation with 1D analysis and commonly reported in literature for simulating wave rotors (Chan et al., 2017; Iancu et al., 2005, 2008).

The fluid properties were selected as air with density set to ideal gas. Under cell conditions, the rotor zone was assigned a mesh motion of the rotor design speed (e.g. 5000rpm).

Boundary conditions: the inlet ports were defined as "Pressure Inlet" and the outlet port was defined as a "Pressure Outlet". The total and static pressures were assumed to be equal and were set to given values. The stator and rotor walls are automaticity defined as a wall. The operating conditions were set to absolute. i.e. operating pressure set to zero.

The solution method was set to implicit and second order with the residual absolute criteria set to 1×10^{-5}. The maximum number of iterations per time step was set to 200. See Figure 7.4 for a typical residual plot.

"Reporting Definitions" were set up to record and write an output file for the following variables: flow time, iterations per time step, mass flow rate and pressure for both the

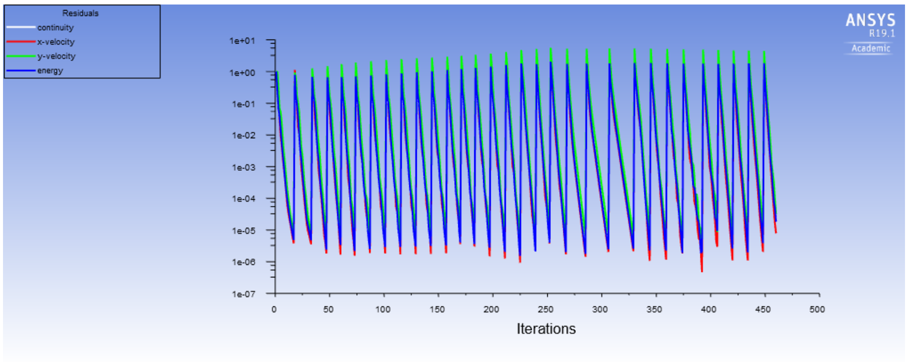

Figure 7.4: Typical Residual plot

inlets and outlet. The simulation was initialised with the channel conditions determined by the 1D analysis described in Chapter 3. The ports were then patched to the conditions of their inlets. Under the "Calculations Activities" the Autosave was set to save solution files at a reasonable interval (e.g. every 1k time steps for a 120k time step simulation).

The time step was determined by the mesh size. This was calculated from the estimated maximum wave velocity calculated by the 1D analysis method and the mesh size. The time step is given by smallest element size divided by the maximum wave speed.

7.4 Mesh Independence

Mesh independence was assessed by comparing the ports' mass flow rates for different mesh sizes. The pressure contour plots were also visually compared. The simulation was deemed to be mesh independent when the mass flow rates varied by <5% for a mesh twice the element count of the other.

Achieving true mesh independence in this case was almost impossible as the finer the mesh, the further resolved the shock and expansion waves become. Also the resolution of the port opening and closing is improved with a finer mesh.

7.5 Reducing Computational Cost

The computational cost of simulating the PEEWR is a major consideration. The 2D setup provides an economical option. However, its biggest disadvantage is the channels only travel past the ports once, hence a steady state is not achieved. This could potentially be overcome by patching the flow field from channels which have passed the ports onto those channels approaching the ports. However, this will require complicated user defined functions. The 3D setup avoids this issue by default. The only disadvantage with the 3D simulation is computational cost. As the model used is inviscid a modified 3D geometry can be used to save computational cost. The 3D geometry can be modified so the channel height is one element high. This is effectively 2D with the radius as the out-of-plane axis.

7.6 Leakage

The methodology discussed here neglects leakage between the channels and porting. Incorporating this into the simulation is relatively simple. However, as the gap between the rotor and end plate is extremely small, the mesh would have to be refined accordingly. This would add considerably to the computational cost which was outside of the resources available for this research.

Chapter 8

Computational Fluid Dynamics Results

Contents

8.1 2D Simulation

The 2D results are computationally efficient, however, as the simulation is not able to achieve a steady state, the results are not a 100% realistic. For a steady state to be achieved the flow conditions in channels that have passed the ports would be equal to the channels moving towards the ports.

The 1D analysis method was used to determine the port timing and initial conditions in the channels. The geometry was based on the experimental PEEWR.

The results presented in Figure 8.1 help visualise the inner workings of the PEEWR. The pressure contour plot (Figure 8.1a) clearly shows the shock and expansion wave positions in each channel (see Chapter 3 for details of expansion and shock wave locations). The temperature contour plot (Figure 8.1b) identifies the gas interfaces between fluids from the high pressure port, low pressure port and fluid already in the channels. To help visualise this better, Figure 8.2 has interface lines drawn into the contour plot. The velocity contour plot presented in Figure 8.1c illustrates how the particle velocity changes as the channel moves past the ports.

The mesh independence was assessed by comparing the mass flow rates of the three ports between two simulations with different mesh sizes. Referring to Table 8.1, the second simulation element size was reduced also to check whether the gradual port opening was affected by a substantially smaller mesh element size. The variation between the two simulations is less than 4%, therefore the results are deemed to be satisfactory from the perspective of assessing the relative significance of PEEWR parameters.

Table 8.1: 2D mesh independence study results

Parameter	**Simulation 1**	**Simulation 2**	**Percentage difference**
Mesh element count	68879	389903	82.3%
Mesh element size (mm)	0.50	0.20	-150.0%
Mass flow rate H inlet (kg/s)	1.48054	1.53127	3.3%
Mass flow rate L inlet (kg/s)	0.47730	0.49064	2.7%
Mass flow rate M outlet (kg/s)	-2.11912	-2.07383	-2.2%

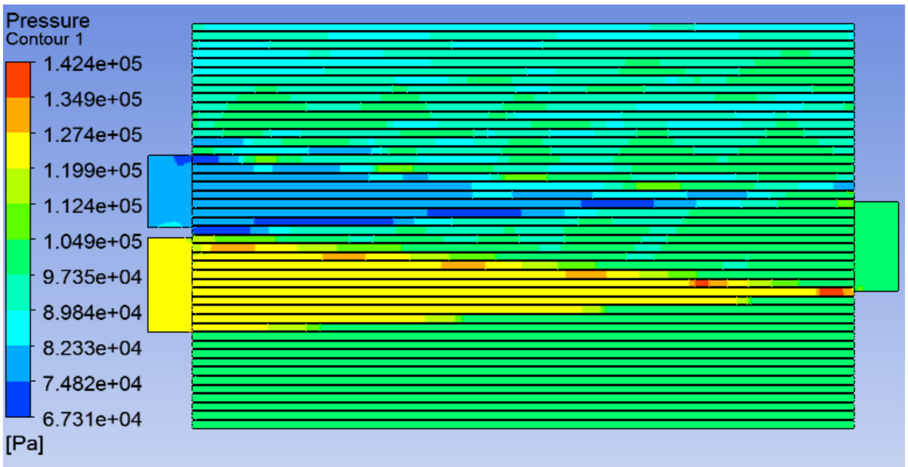

(a) Pressure

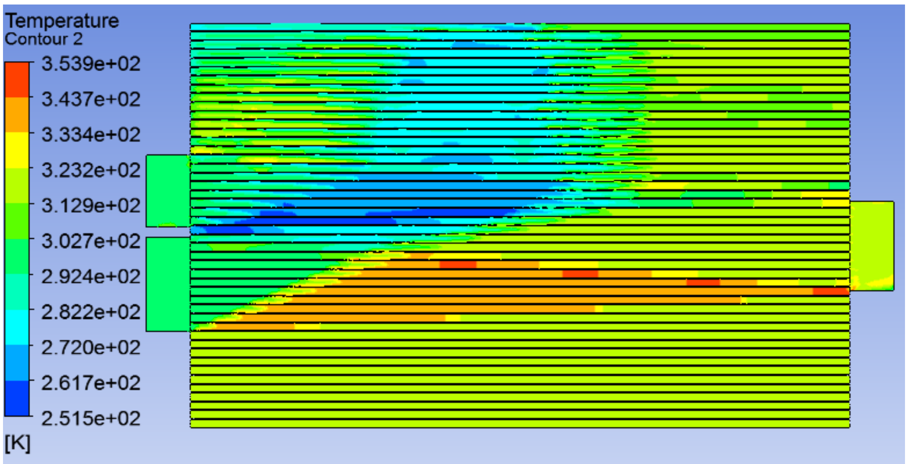

(b) Temperature

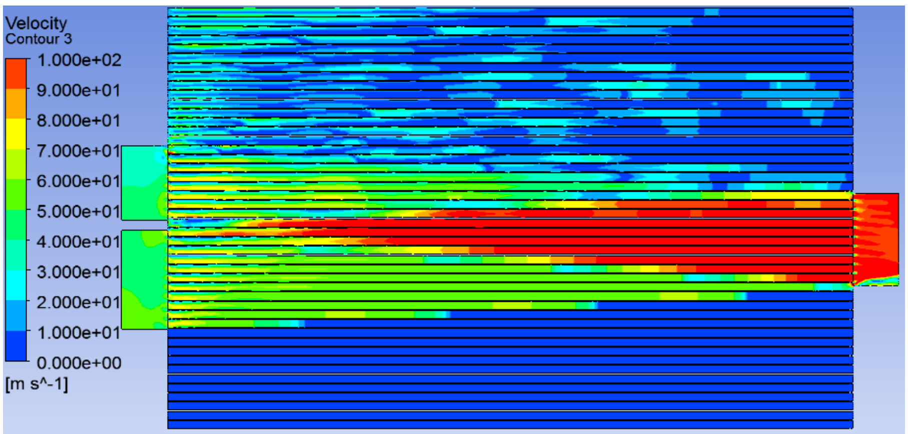

(c) Velocity

Figure 8.1: 2D CFD Contour plots (channels moving up the page)

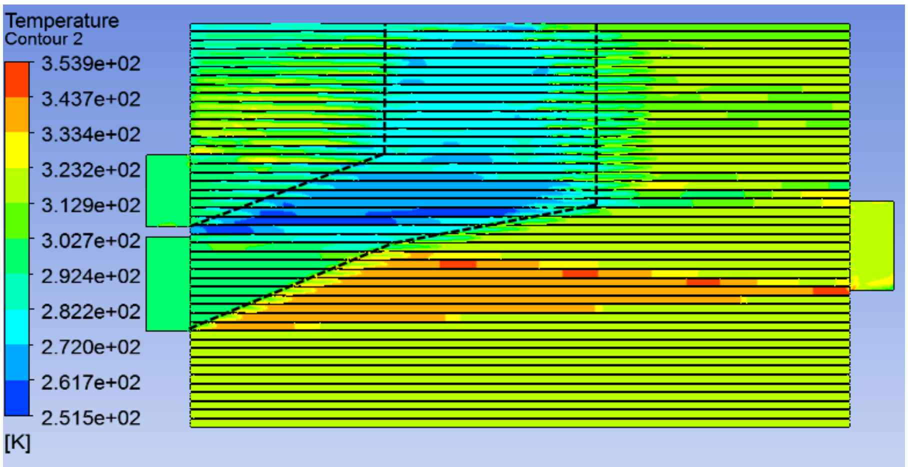

Figure 8.2: 2D CFD contour plot of gas interface markings

8.2 Porting Angle Effects

The experimental performance results obtained in Chapter 6 are substantially lower than predicted by the 1D analysis and experimental results published by Kentfield (1969). Literature has indicated that using suboptimal porting angles causes efficiency drops (Paxson & Wilson, 1995). The optimal angle for the porting is determined by the velocity of the flow in the channel and channel tangential velocity as illustrated in Figure 8.3. Moreover the port angle is the same as the angle of fluid flow resultant velocity in the rotor channels. The quantitative effect of suboptimal port angles is not clear. Hence, in this section the effect of port angles will be examined using CFD.

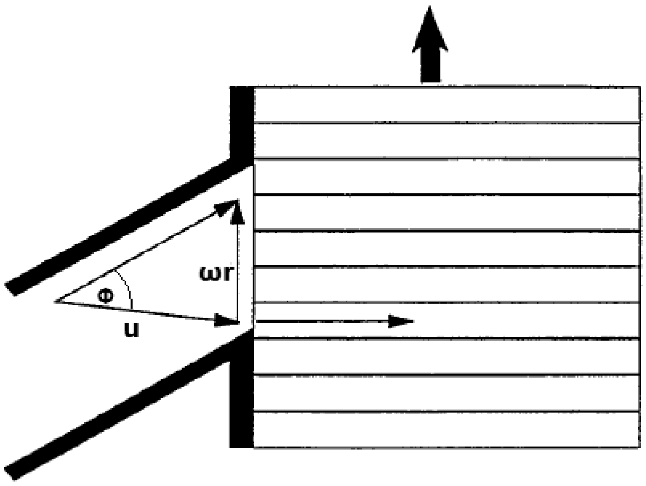

Figure 8.3: Optimal port angle (Paxson & Wilson, 1995)

To save on computational cost the single cell height 3D CFD method was used. As illustrated in Figure 8.4 two different CFD simulations were carried out: one with straight ports and the other with optimal angled ports. The flow field and port timing was determined using the 1D analysis method. The port angles were determined with the following equation:

$$tan\,(\phi) = \frac{\omega r}{u} \tag{8.1}$$

Where: u = fluid velocity entering/leaving channel, ω = rotor angular velocity and r = the mean channel radius.

The rotor geometry is the same as the experimental PEEWR except the channel height is reduced to one cell at the medium channel radius. The boundary conditions were selected

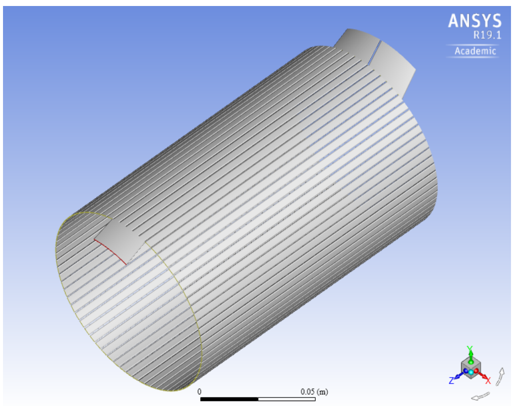

(a) Optimally angled

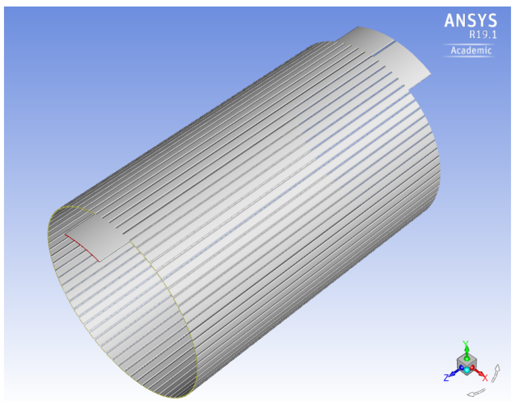

(b) Straight

Figure 8.4: Geometry for the porting comparison CFD simulations

based on the experimental results, as shown in Table 8.2.

Table 8.2: Boundary conditions for the porting comparison CFD simulations

Port	Pressure (kPa)	Temperature (K)
Medium pressure	100	300
High pressure	120	300
Low pressure	80	300

The simulations were run until the mass flow though the ports did not perceptibly change from one cycle to the next. This was determined by monitoring the mass flow rates of each port. This is illustrated in Figure 8.5. The mass entering the PEEWR and leaving is shown by the blue and green line to be the same(i.e. mass entering the PEEWR is equal to the mass leaving). Referring to Figure 8.5, the oscillation in mass flow of each port is caused by the opening and closing of channels as they pass the ports.

As the geometry and operating conditions of the optimally angled and straight port configured simulations are almost identical a mesh independence study was only carried out for the optimally angled port simulation. The results of the mesh independence study are presented in Table 8.3. For both the optimally angled and straight port results presented in Table 8.4, the mesh element size was 0.4mm.

Table 8.3: Mesh independence for optionally angled ports

Parameter	Simulation 1	Simulation 2	Simulation 3	Percentage difference sim 1 & 2	Percentage difference sim 2 & 3
Mesh elements count	150713	241821	965567	37.7%	75.0%
Mesh element size (mm)	0.50	0.40	0.20	-25.0%	-100.0%
ζ	0.20100	0.2120	0.20510	5.0%	-3.1%
η	0.52320	0.49120	0.47540	-6.5%	-3.3%

Table 8.4: Performance comparisons for assessing significance of porting angles

	1D analysis	Optimally angled ports	Straight ports
Efficiency (η)	0.64	0.56	0.40
Performance parameter (ζ)	0.49	0.22	0.17

The velocity vectors in Figures 8.6 and 8.7 illustrate the effects of the angled and straight ports. Looking at the outlet (Figures 8.6), the angled port is aligned with the flow leaving

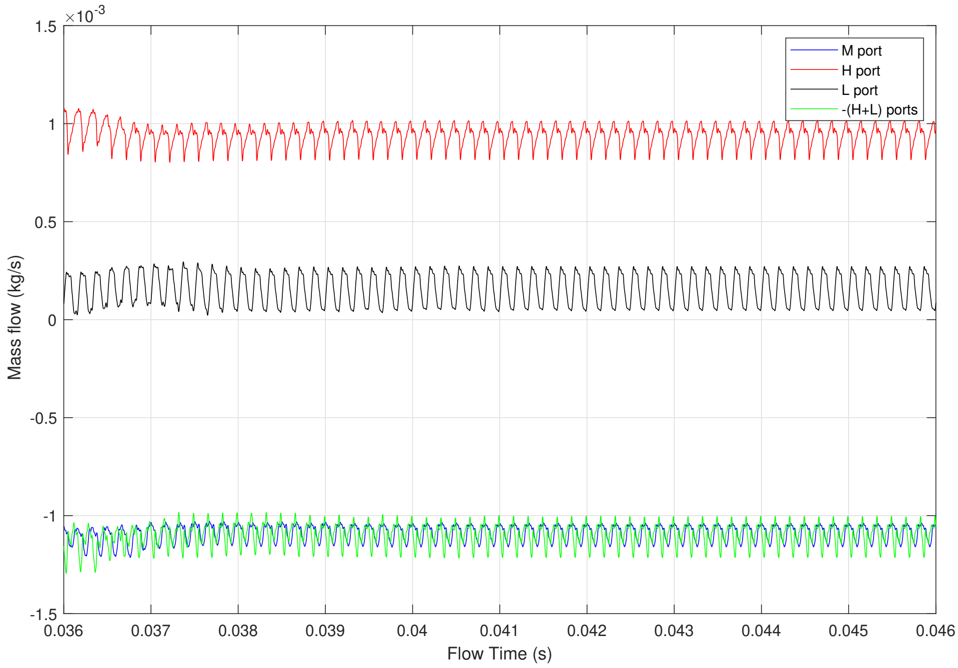

Figure 8.5: Port mass flow rates for assessing change in flow field with rotor rotation

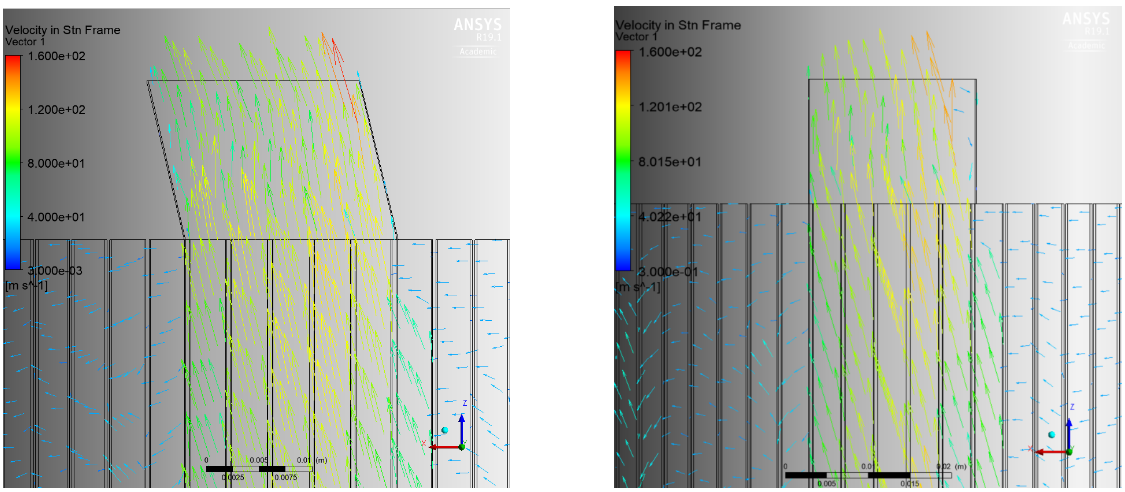

(a) Optimally angled

(b) Straight

Figure 8.6: Outlet velocity vectors for comparing flow field of the straight and angled port simulations

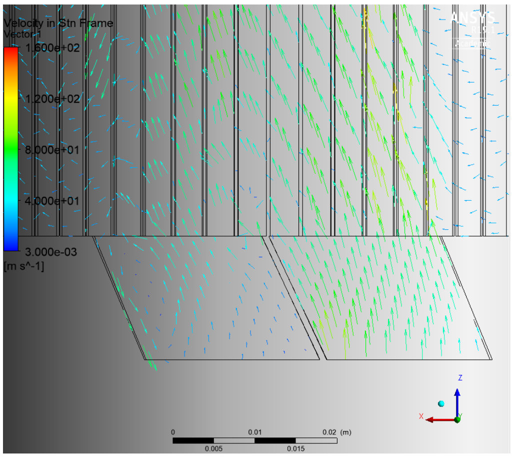

(a) Optimally angled

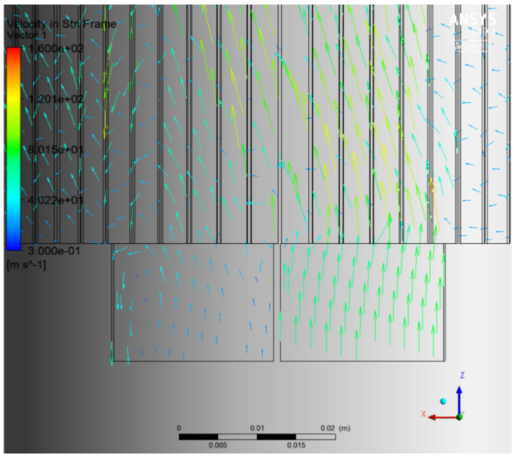

(b) Straight

Figure 8.7: Inlet velocity vectors for comparing flow field of the straight and angled port simulations

the channels whereas flow exiting the channels into the straight port is hitting the left-hand wall and causing a recirculation on the right-hand side of the port. Flow impacting the left-hand wall of the port causes a braking on the rotor, hence energy will be lost, which ultimately will cause an efficiency reduction.

The inlet velocity vectors shown in figure Figures 8.7 are more interesting. The high pressure port behaves largely as expected, however the low pressure port has recirculation present in both the straight and angled ports. As this recirculation is present in both it would be most likely an inaccuracy in the port timing calculation rather than the an effect of port angles.

The difference in the velocity vector fields for the straight and angled ports suggest different PEEWR performance in each case. To analyse this quantitatively, the efficiency and performance parameters have been calculated and presented in Table 8.4. Velocity, temperature and pressure contour plots differed little with port arrangement, hence the are only included in Appendix F. Referring to Table 8.4, the angled ports are notably more efficient compared to the straight ports. The reason for the higher simulated efficiency by the 1D analysis is mainly due to the recirculation in the low pressure port which is present in the CFD simulations.

In conclusion, the porting angles definitely needs to be considered within the design, at least for the present operating conditions. As much as 16% lost efficiency has been simulated for the straight-port case relative to the optimally-angled-port case. Further simulations would be required at different boundary conditions to understand this comprehensively. It must also be noted that if the port angle is too large efficiency will also be lost.

8.3 3D Simulation

Simulating the PEEWR in full 3D with the same port geometry as the experimental device enables a direct comparison to be made between experimental and CFD results. The computational cost for 3D simulations is extremely high, hence only one set of operating conditions has been simulated as shown in Table 8.5. Similarly, due to computation cost and time constraints, a full mesh independence study was not able to be undertaken. However, based on the CFD carried out in the previous sections the mesh element size was selected to be 0.5 mm. Based on the mesh independence studies carried out in the previous sections the results should be reasonably reliable for an approximate solution.

Table 8.5: Boundary conditions for 3D CFD simulations

Port	**Pressure (kPa)**	**Temperature (K)**
Medium pressure	100	300
High pressure	110	300
Low pressure	91	300

8.3.1 Viscous Simulation

It was identified in Chapter 6 that a possible cause of the low efficiency compared to Kentfield (1969) was boundary layers. The CFD carried out so far is limited to inviscid simulations, hence to investigate this a viscous CFD model is required but should a laminar or turbulent boundary layer simulation be performed? As the channels are fairly short, the flat plate Reynolds number is used to provide guidance. Cengel and Ghajar (2015) gives the critical Reynolds number for flat plate boundary layer transition as:

$$Re_{cr} = 5 \times 10^5$$

Therefore, the critical velocity can be calculated. The temperature will be assumed as 293 K therefore, the kinematic viscosity at approximately atmospheric pressure (indicative of the values within the channels) is $\nu = 1.515 \times 10^{-5}\ \mathrm{m^2/s}$ (Cengel & Ghajar, 2015).

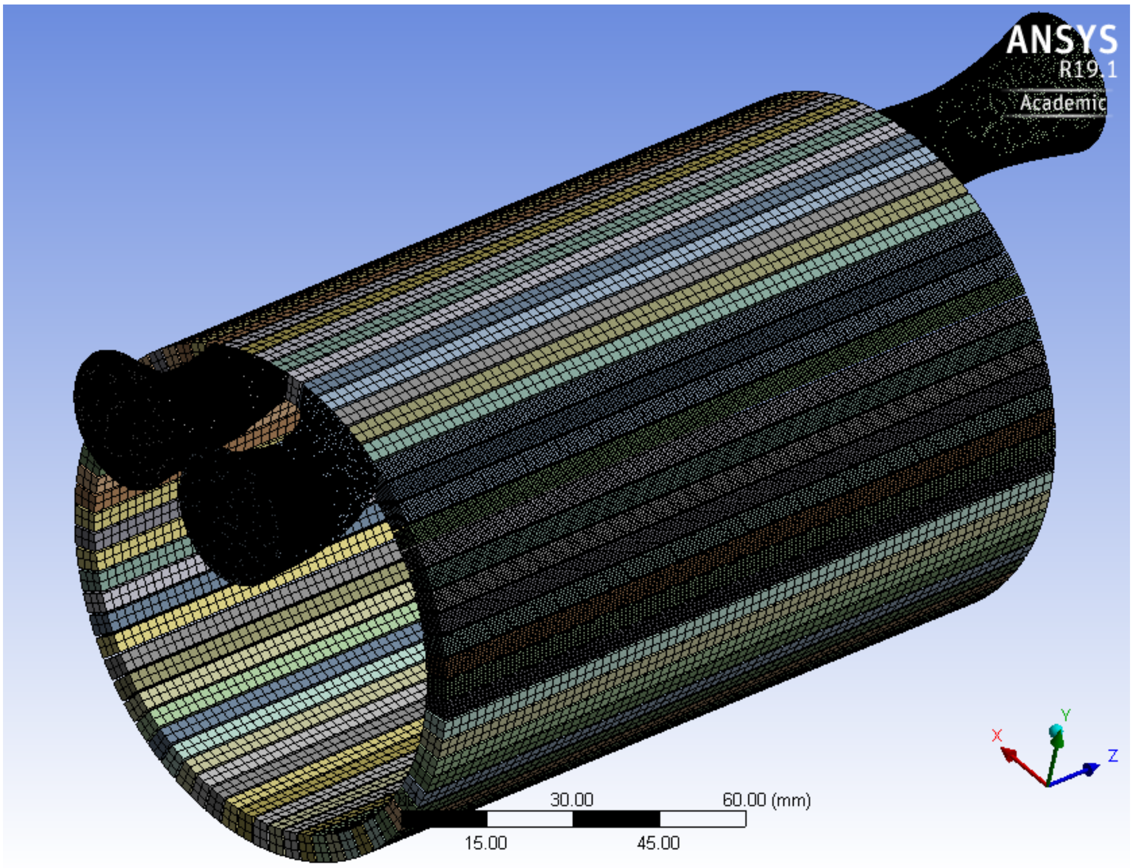

Figure 8.8: Viscous simulation mesh showing refined region

Therefore, the critical channel velocity is

$$Re_{cr} = \frac{u_{cr} l}{\nu} \longrightarrow u_{cr} = \frac{Re_{cr}\nu}{l} = \frac{5 \times 10^5 \times 1.515 \times 10^{-5}}{0.15} = 50.5\,\text{m/s}$$

With the boundary conditions specified in Table 8.5, the 1D analysis simulates a maximum channel velocity of 46 m/s therefore, a laminar CFD model is appropriate for this case.

The 3D methodology described in Chapter 7 was modified to use the laminar model in Fluent. The computational cost was a major issue. This was dealt with by patching the inviscid flow field from the previous inviscid simulation. This saved about five days of computing. Also the mesh was refined only on a selection of channels as illustrated in Figure 8.8. This does introduce an approximation in the flow field analysis. However, all the results were taken when refined channels were aligned with the ports to minimise the effect. If the mesh refined on all the channels, the simulation was projected to solve one rotation of the rotor in 34 days with 80 processes and 500 GB of memory assigned, hence the decision was made to reduce the mesh element count.

8.3.2 Results

The inviscid full 3D simulation was not run until it reached a steady state as computational resources were limited, so it was decided to pursue the laminar simulation in preference to the inviscid simulation. However, a comparison can still be made by comparing the two simulations at the same flow time before the steady state is reached.

The inviscid pressure contour plot presented in Figure 8.9a shows the first shock wave reaching the end of the channel just as the medium pressure port opens. However, the laminar contour plot in 8.9b shows the shock wave failing to reach the end of the channel. This is also the case even when the simulation reaches a steady state as shown by Figure 8.10.

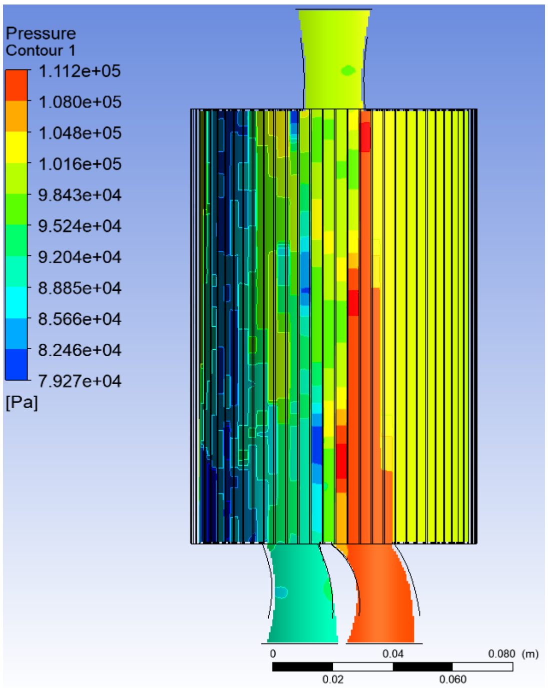

(a) Inviscid

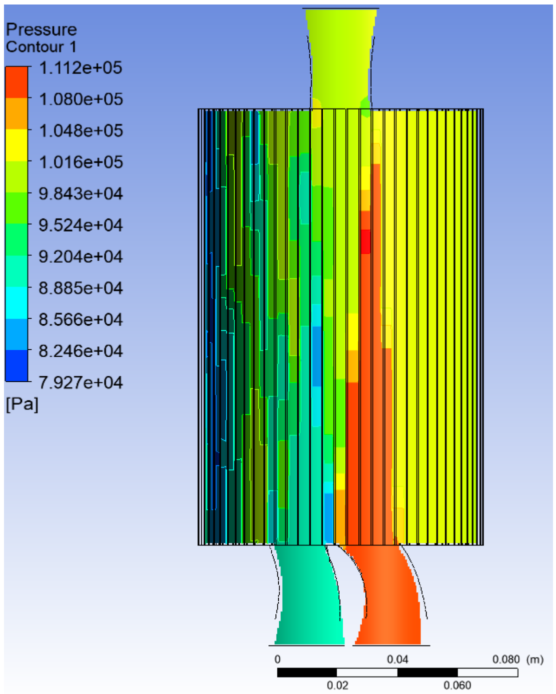

(b) Laminar

Figure 8.9: Pressure contour at mean channel radius for comparing the two simulations

The difference in the velocity contour plots was small aside from the boundary layers being present in the laminar case. Hence, they have been included in Appendix F. The maximum channel velocity was approximately 45.3 m/s for the inviscid case and 46.7 m/s for the laminar case. The steady state laminar velocity contour as illustrated in Figure 8.11 had slightly higher maximum channel velocity of 54.8 m/s. This is slightly higher than the calculated critical velocity for laminar flow. However, as the average velocity at that point in the channel is below the critical laminar velocity, treating it as laminar is probably reasonable.

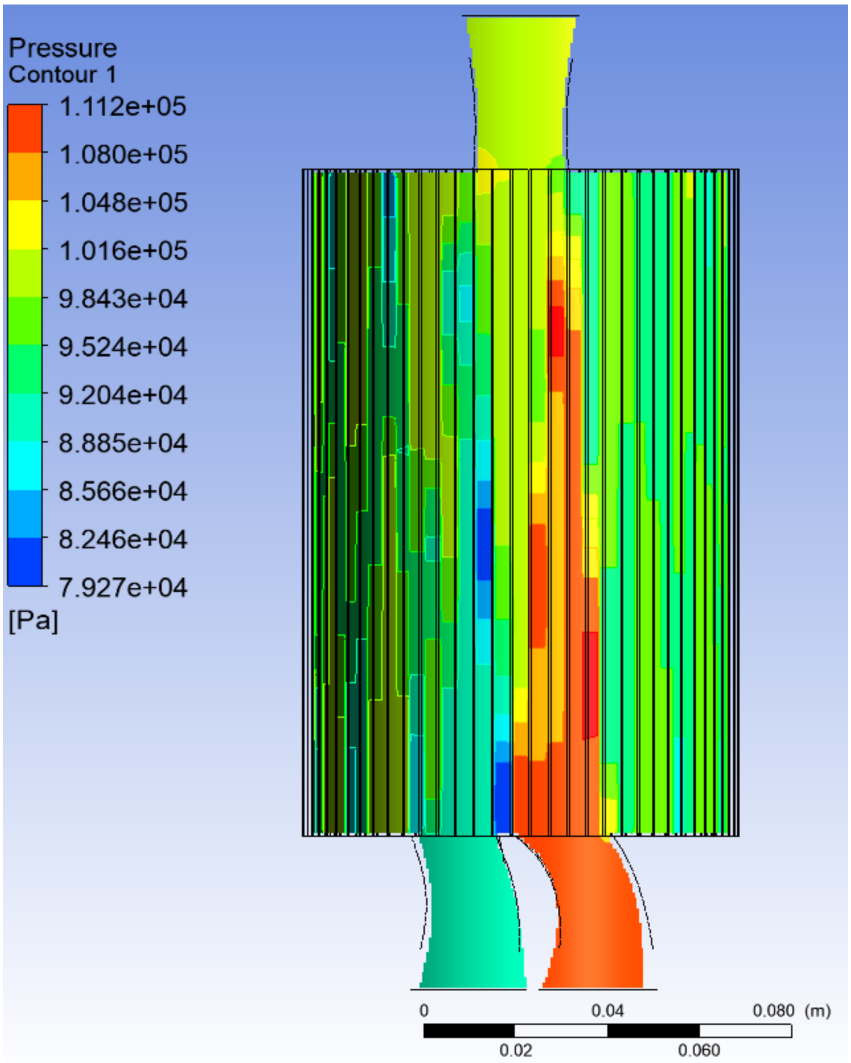

Figure 8.10: Laminar steady state pressure contour for assessing pressure distribution in rotor channels

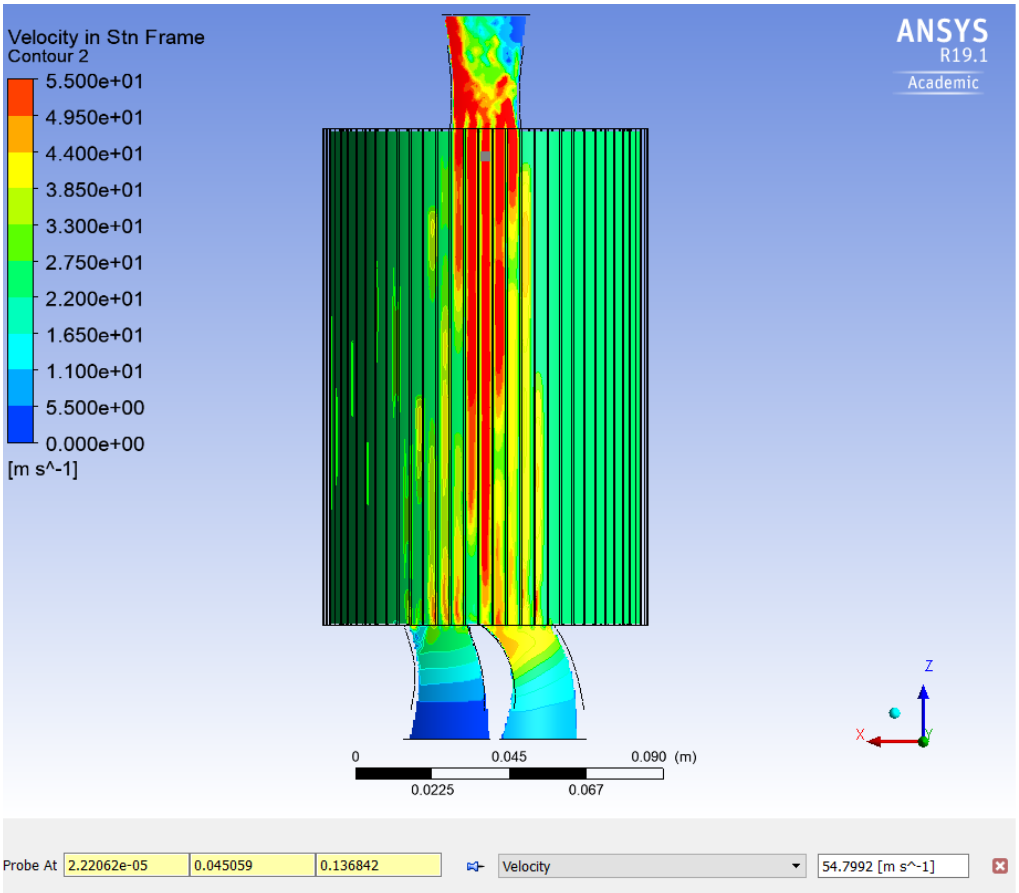

Figure 8.11: Laminar steady state velocity contour for velocity distribution in rotor channels and ports

The steady state laminar temperature contour plot in Figure 8.12 indicates very small entrainment of both low and high pressure fluid per rotation. This could be attributed to the low pressure ratios being simulated.

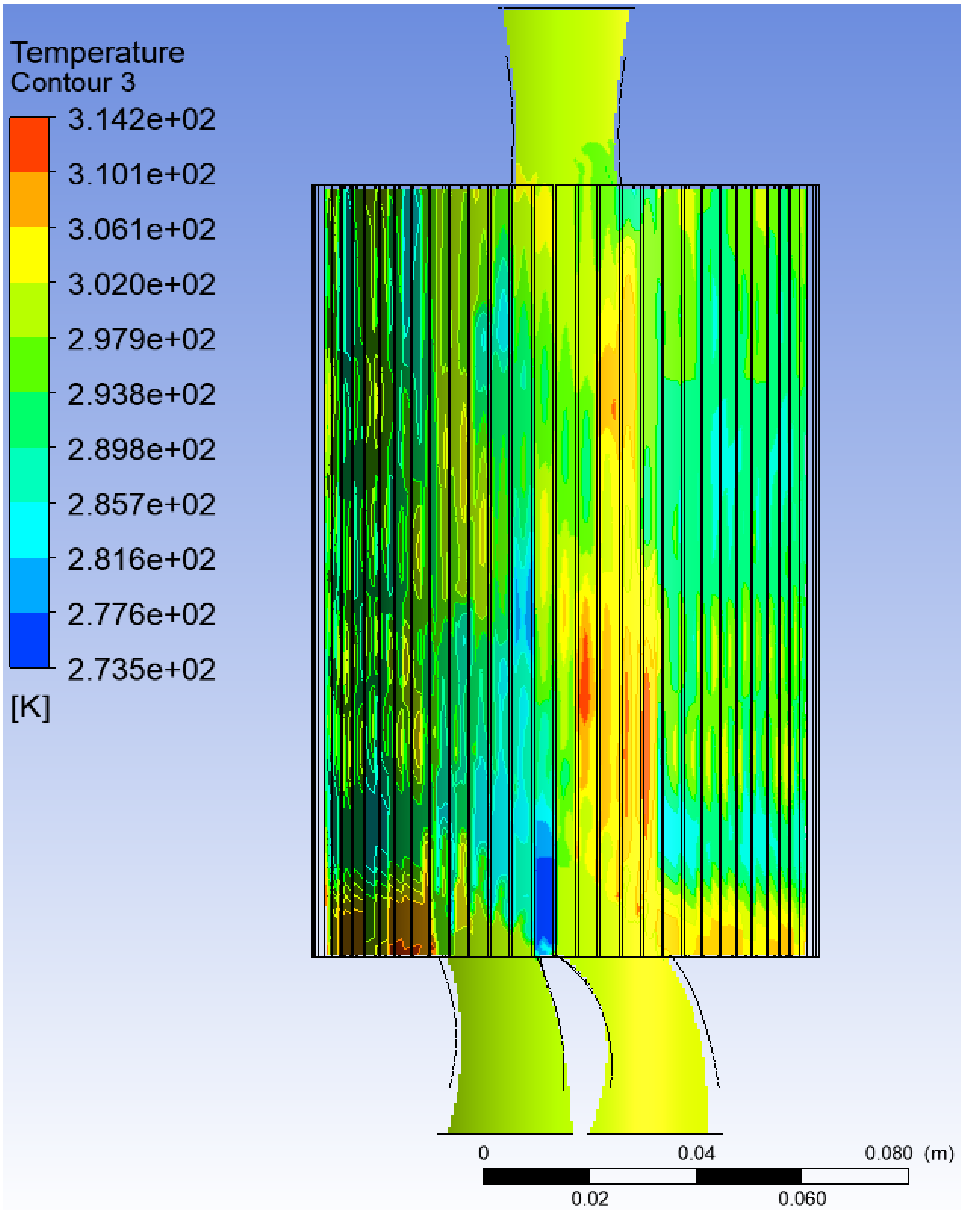

Figure 8.12: Laminar steady state velocity contour illustration temperature distribution in rotor channels

Referring to Figure 8.13, the velocity vectors confirm the port timing is correct for the simulated boundary conditions. It should also be noted, the port angles are far from optimal as most notably illustrated by the medium pressure port in Figure 8.13b.

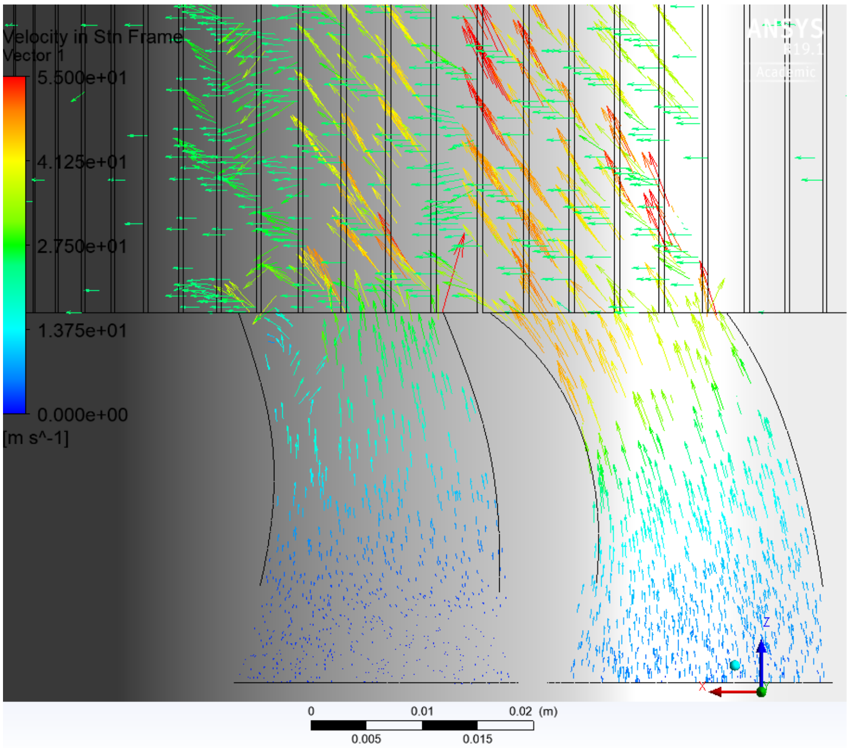

(a) Inlet ports

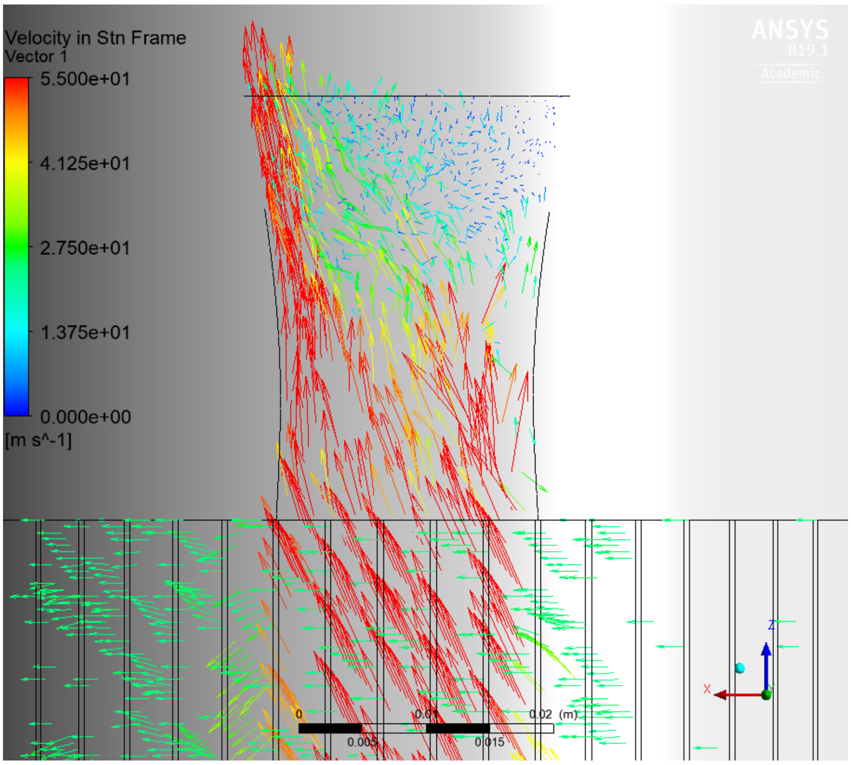

(b) Outlet port

Figure 8.13: Laminar steady state port velocity vectors illustrating the flow field entering and leaving the channels

The boundary layers are best illustrated by the velocity cross sectional contour plots in Figure 8.14. The locations of the cross sections are depicted in Figure 8.15. The boundary layers are reasonably consistent in thickness being slightly thicker at lower velocities. The average boundary layer thickness is approximately 0.6 mm. This may be small, however, considering the 3.5mm $\times$ 5mm channel dimensions, the flow area taken up by boundary layers is approximately

$$A_b = 3.5 \times 5 - (3.5 - 0.6)(5 - 0.6) = 4.74\,\mathrm{mm}^2$$

As a proportion of the channel cross sectional area; the boundary layers occupy

$$4.74/(3.5 \times 5) \times 100\% = 27.1\%$$

As the velocity of the fluid entering from the low pressure port is lower than the other ports, the boundary layers have a larger relative thickness in the channels near the low pressure port. Hence, a reduction in performance would be expected as the effective low pressure port flow area is smaller. Moreover, the smaller the low pressure port flow rates, the lower ζ and η are as they are proportional to $\dot{m}_L/\dot{m}_H$.

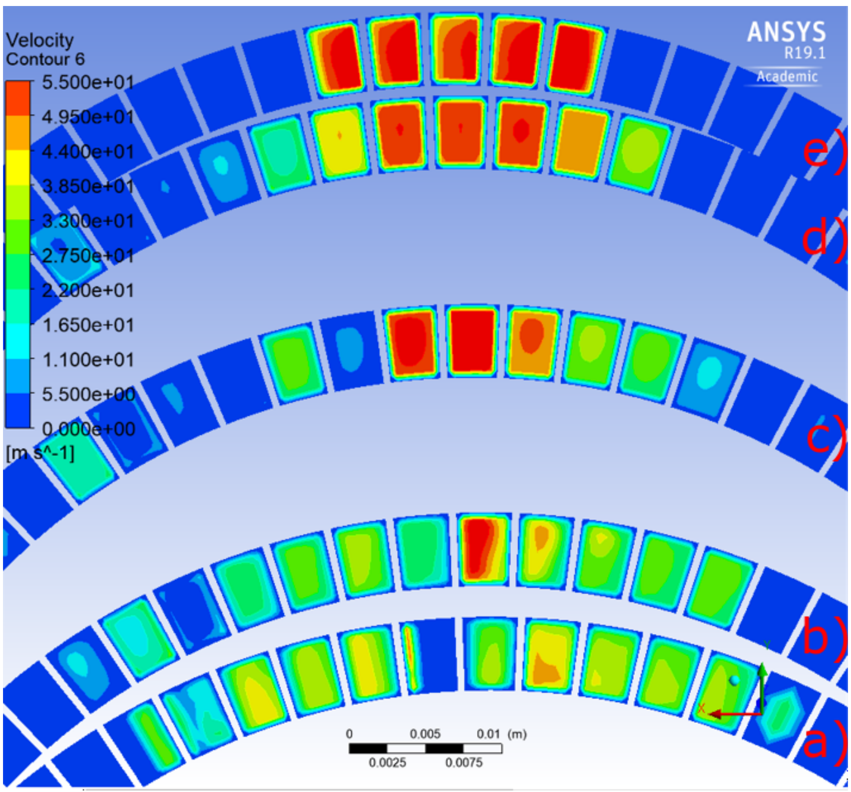

Figure 8.14: Laminar steady state velocity cross sections for assessing boundary layer thickness

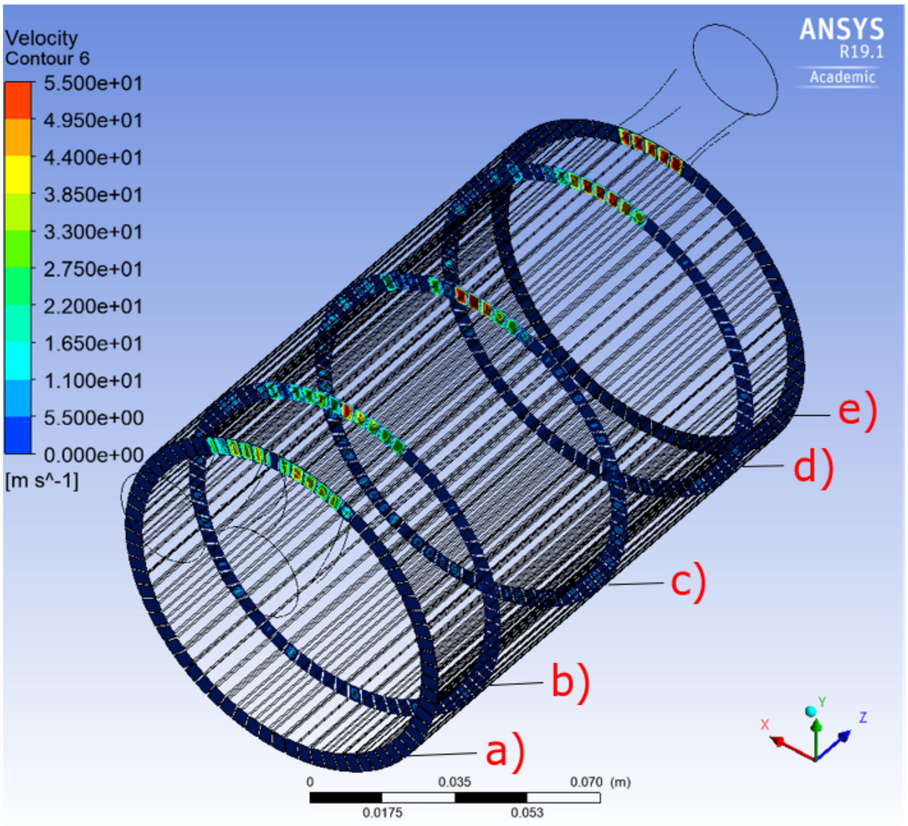

Figure 8.15: Velocity cross section locations presented in Figure 8.14

8.4 Discussion

The contour plots presented in the previous section indicate losses from viscous effects. Table 8.6 compares η and ζ from simulated and experimental data at the given boundary conditions specified in Table 8.5. Although the inviscid CFD simulation was not run until it reached a steady state it has been included for an approximated guide to what would be expected for a steady state inviscid simulation.

Table 8.6: Performance comparisons

	1D analysis	Kentfeild	CFD Inviscid	CFD Laminar	Experimental
Efficiency (η)	0.82	<0.7	0.49	0.40	0.30
Performance parameter (ζ)	0.75	$\approx$ 0.65	0.45	0.37	0.29

The efficiency predicted by the laminar CFD simulation is the closet to the experimental results obtained as part of this work. This is expected as the laminar CFD model is the most realistic out of the simulation methods used not withstanding questions on solution convergence. The difference in results between experimental and laminar CFD would also arise because the laminar simulations neglect end plate leakage, heat transfer from the channel walls and turbulence in the ports.

The CFD results confirm suboptimal port angles and boundary layers are major contributors to the low experimental ζ and η values. However, there is 10% efficiency still unaccounted for which is thought to be caused by factors such as end plate leakage and heat transfer from the channel walls.

Through improved design, most of the inefficiencies discussed above can be minimised or eliminated. Making the channels larger in cross sectional area would greatly reduce the effects of boundary layers and should improve the alignment of the experimental results with the published results by Kentfield (1969). In addition, incorporating the optimal porting angle in the design would improve performance significantly.

Chapter 9

Conclusion

Contents

9.1 Conclusion

Wave rotor research has been stimulated by various potential applications since the 1940s. However, to the present time only one application has been successfully commercialised: internal combustion engine supercharging. Despite this, most of the applications proposed still have merit. Current literature on pressure exchanger equalising wave rotors (PEEWRs) is limited, but as for other types of wave rotors, the potential for practical deployment remains high. This project was aimed at expanding the knowledge of PEEWRs for air pumping applications.

The 1D analysis method developed as part of this work utilises the Euler compressible flow equations to determine the required port timing of a PEEWR for a given set of boundary conditions and simulate the flow field in the rotor channels. The main advantage of the method is the extremely low computational cost. Hence, the method provides a good alternative to CFD for preliminary analysis. As part of this work, the 1D analysis method has been used to generate simulated performance maps that demonstrate on exceptionally good correlational to experimental results published in literature. The 1D simulations have also been used to determine port timing for both CFD geometries and the experimental test rig ports.

The experimental results mapped for the USQ PEEWR have the same trend as Kentfield (1969) however, the maximum overall isentropic efficiency achieved was lower than reported by Kentfield (1969) (35% compared to 70%) and simulated by the present 1D analysis. CFD studies were undertaken to understand the cause of the low efficiency.

Through utilisation of CFD it was identified suboptimal port angles were responsible for as much as 16% loss in efficiency. Also viscous effects were identified to cause losses of approximately 10% in efficiency of the PEEWR at USQ.

Considering the experimental and CFD results, PEEWRs have definite potential to be a competitive alternative to ejectors. With improved design, efficiencies closer to values published by Kentfield (1969) should be achievable. Design improvements would include: larger channel size to reduce the effects of boundary layers and optimising the port angles for the desired operating conditions.

9.2 Further Work

Other losses not studied as part of this work such as end plate leakage and heat transfer between the rotor channels and the fluid are topics for further investigation. From here, redesigning the rotor and ports to incorporate the recommendations discussed in the previous section would be the next logical step in the PEEWR research at USQ. Then, obviously, this would require experimental validation of these design improvements.

References

Akbari, P. & Mueller, N. (2005).
Wave rotor research program at Michigan State University. *41st AIAA/ASME/-SAE/ASEE Joint Propulsion Conference and Exhibit*. doi:10.2514/6.2005-3844

Akbari, P., Nalim, R. & Mueller, N. (2006).
A review of wave rotor technology and its applications. *Journal of Engineering for Gas Turbines and Power-Transactions*, *128*. doi:10.1115/1.2204628

Anderson, J. D. (1990).
Modern Compressible Flow: with Historical Perspective. McGraw-Hill New York.

Azoury, P. (1965).
An Introduction to the dynamic pressure exchanger. *Proceedings of the Institution of Mechanical Engineers*, *180*(1), 451–480.

Berchtold, M. & Gardiner, F. (1958).
The Comprex: a new concept of diesel supercharging. In *ASME 1958 Gas Turbine Power Conference and Exhibit* (V001T01A016–V001T01A016). Citeseer.

Cengel, Y. A. & Ghajar, A. J. (2015).
Heat and Mass Transfer. New York: McGraw-Hill.

Chan, S., Liu, H., Xing, F. & Song, H. (2017).
Wave rotor design method with three steps including experimental validation. *Journal of Engineering for Gas Turbines and Power*, *140*. doi:10.1115/1.4038815

Cooper R J, H. R. L., Slade R M & G, A. J. (2006).
Cumulative uncertainty in measured streamflow and water quality data for small watersheds. *Transactions of the ASABE*, *49*(3), 689–701.

Costiuc, I. & Chiru, A. (2017).
Evolution of the pressure wave supercharger concept. In

IOP Conference Series: Materials Science and Engineering (Vol. 252, *1*, p. 012081). IOP Publishing.

Dai, Y., Cheng, Y., Zou, J. & Hu, D. (2015).
Superheating and supercharging characteristics of moving shock in wet steam flows. *International Journal of Heat and Mass Transfer*, *86*, 351–357.

Fatsis, A. & Ribaud, Y. (1999).
Thermodynamic analysis of gas turbines topped with wave rotors. *Aerospace Science and Technology*, *3*(5), 293–299. doi:https://doi.org/10.1016/S1270-9638(00)86965-5

Gyarmathy, G. (1983).
How does the comprex pressure-wave supercharger work? In *SAE Technical Paper 830234*.

Hermann, H. (1989).
Car tests with a free-running pressure-wave charger-a study for an advanced supercharging system. In *SAE Technical Paper*. doi:10.4271/890453

Hîrceagă, M., Iancu, F. & Müller, N. (2005).
Wave rotors technology and applications. *The 11th International Conference on Vibration Engineering, Romania*.

Hitomi, M., Yuzuriha, Y. & Tanaka, K. (1989).
The characteristics of pressure wave supercharged small diesel engine. In *SAE Technical Paper 890454*.

Hu, D., Yu, Y. & Liu, P. (2018).
Enhancement of refrigeration performance by energy transfer of shock wave. *Applied Thermal Engineering*, *130*, 309–318.

Iancu, F. & Müller, N. (2006).
Efficiency of shock wave compression in a microchannel. *Microfluidics and Nanofluidics*, *2*(1), 50–63.

Iancu, F., Piechna, J. & Müller, N. (2005).
Numerical Solutions for Ultra-Micro Wave Rotors (UmWR). In *35th AIAA Fluid Dynamics Conference and Exhibit* (p. 5034).

Iancu, F., Piechna, J. & Müller, N. (2008).
Basic design scheme for wave rotors. *Shock Waves*, *18*(5), 365–378.

Kentfield, J. A. C. (1963).
An examination of the performance of pressure-exchanger equalisers and dividers (PhD, Imperial College London).

Kentfield, J. A. C. (1969).

The performance of pressure-exchanger dividers and equalizers. *Journal of Basic engineering*, *91*(3), 361–368.

Kentfield, J. A. C. (1998).
Wave rotors and highlights of their development. In
34th AIAA/ASME/SAE/ASEE Joint Propulsion Conference and Exhibit. doi:10.2514/6.1998-3248

Kharazi, A., Akbari, P. & Müller, N. (2004).
An Application of wave rotor technology for performance enhancement of R718 refrigeration cycles. In
2nd International Energy Conversion Engineering Conference.

Kharazi, A., Akbari, P. & Müller, N. (2005).
Preliminary study of a novel R718 compression refrigeration cycle using a three-port condensing wave rotor. *Journal of Engineering for Gas Turbines and Power*.

Leahu, C.-I. & Chiru, A. (2015).
Research on sequential speed driving of the pressure wave compressors. *Annals of the Oradea University*, *10*. doi:10.15660/AUOFMTE.2015-1.13099

Lenoble, G. & Ogaji, S. (2010).
Performance analysis and optimization of a gas turbine cycle integrated with an internal combustion wave rotor. *Proceedings of The Institution of Mechanical Engineers Part A-journal of Power and Energy*, *1*, 1–12. doi:10.1243/09576509JPE984

Mardarescu, V., Hirceaga, M., Radu, G.-A. & Leahu, C.-I. (2010).
A study of parameters influencing the performance of a pressure wave supercharger (PWS) (tech. rep. No. CONAT20101001). Transilvania University Press.

Mataczynski, M. R. (2014).
Design and simulation of a pressure wave supercharger for a small two-stroke engine (Master’s, Air Force Insititute of Technology, USA Ohio).

Mayer, A., Oda, J., Kato, K., Haase, W. & Fried, R. (1989).
Extruded ceramic-a new technology for the Comprex®-rotor. In
SAE Technical Paper 890425.

Paxson, D. E. & Wilson, J. (1995).
Recent improvements to and validation of the one dimensional NASA wave rotor model (tech. rep. No. NASA-TM-106913). NASA Lewis Research Center; Cleveland, OH, United States.

Shreeve, R. & Mathur, A. (1985).
Proceedings of the 1985 ONR/NAVAIR wave rotor research and technology workshop. Naval Postgraduate School California United States.

Swissauto. (2019). Retrieved from https://www.swissauto.com

Tüchler, S. & Copeland, C. D. (2019).
Experimental results from the bath μ-wave rotor turbine performance tests. *Energy Conversion and Management*, *189*, 33–48.

Weatherston, R. & Hertzberg, A. (1967).
The Energy exchanger, a new concept for high-efficiency gas turbine cycles. *Journal of Engineering for Power*, *89*(2), 217–227.

Wilson, J. (1998).
An Experimental determination of losses in a three-port wave rotor. *Transactions-American Society of Mechanical Engineers Journal of Engineering For Gas Turbines And Power*, *120*, 833–842.

Wilson, J. & Fronek, D. (1993).
Initial results from the NASA Lewis wave rotor experiment. In *29th joint propulsion conference and exhibit* (NASA-TM-106148), Monterey, CA; United States.

Yuqiang, D., Jiupeng, Z., Che, Z., Peiqi, L., Jiaquan, Z., Liming, Z. & Dapeng, H. (2010).
Thermodynamic analysis of wave rotor refrigerators. *Journal of Thermal Science and Engineering Applications*, *2*(2).

Zhao, J. & Hu, D. (2017).
An improved wave rotor refrigerator using an outside gas flow for recycling the expansion work. *Shock Waves*, *27*(2), 325–332.

Appendix A

Project Specification

ENG 4111/2 Research Project

Project Specification

For:	**Liam Channer**
Topic:	Investigating wave rotor performance characteristics for air pumping applications
Supervisors:	Professor David Buttsworth
Sponsorship:	Faculty of Health, Engineering & Sciences
Project Aim:	Current literature on wave rotors do not provide enough detail to confidently build a working device. The aim of this project is to finish building and commission a 3 port wave rotor already designed and mostly manufactured at USQ. Once the device is commissioned the performance will be mapped and compared to limited results presented in current literature. Reporting detailed wave rotor performance maps and notes on the manufacturing, assembly, commissioning and testing will help fill the lacking detail in current literature, while hopefully improving understanding of wave rotors for air pumping applications. If time and resources permit possible design improvements will also be investigated.

Program:

1. Conduct further background research on wave rotors.
2. Finish building, assembling and commissioning of the wave rotor at USQ.
3. Perform experiments to quantify the performance of the wave rotor.
4. Analyse wave rotor performance maps.
5. Report the findings and draw conclusions.

As time and resources permit:

1. Investigate modifying the operating cycle to improve efficiency.
2. Conduct CFD simulations of baseline and improved cycles.
3. Try and source a Comprex wave rotor (commercially produced wave rotor in the 1990s) to analyse the engineering of this device.

Agreed:

Student Name:	Liam Channer
Date:	19/03/2019
Supervisor Name:	David Buttsworth
Date:	19/03/2019

Appendix B

1-D Analysis MATLAB code

```
% Pressure Exchanger Equalising Wave Rotor One Dimensional Analysis Code
%
% INPUT
% Port pressures and temperatures under "inputs' section.
% OUTPUT
% The code returns the required port timing for optimal operating cycle.
% Simulated Isentropic efficiency and performance parameter
%
% Refer to thesis chapter 3 for diagram and explanation of equations.
%
%
% Written by: L. Channer
%
% Written July 2019
%
% Last updated on: 14/08/2019
%
%
close all
```

```
clear
clc
%% inputs
P_H= 125e3; T_H = 300;
P_L = 80e3; T_L = 300;
P_M = 100e3;
gam=1.4; R= 287.05;
t_Ho = 0;  % H port open time
l = 0.15; % channel length (m)

% Assumed initial zone A conditions
P_A = P_L;
T_A1 = T_L;
T_A2 = T_A1;
a_A1 = sqrt(gam*R*T_A1);
a_A2 = sqrt(gam*R*T_A2);
x1 = 0.05;

% Iterate to find actual conditions in zone A
for ii = 1:100

    disp(['Iteration ',int2str(ii),', P_A = ',num2str(P_A
       /1e3),' kPa, T_A1 = ',num2str(T_A1),' K'])

    if ii <=60  % reset error for next iteration.

        ERROR =0;

    end
%% first shock wave S_1
    PI_s1NEW =2; % values to start loop
    PI_s1 = 5; % values to start loop
    count_1 = 0;
    while round(PI_s1,3)~=round(PI_s1NEW,3)
        PI_s1 =(PI_s1+PI_s1NEW)/2; % assuming the pressure
            ratio (average of previous assumptions and
           calculated)
```

```

        P_B=PI_s1*P_A; % finding pressure in B1

        if P_B > P_H   % Checking assumption is reasonable
            i.e P_B1 can not be > P_H
            PI_s1NEW=PI_s1*.9;
        else
            Ma_B3 = sqrt( ((P_H/P_B).^((gam-1)/gam)-1)*2/(
                gam-1)); %EQ h1 Calculating mach number in
                B3

            a_B3 = (P_B./P_H).^((gam-1)./(2*gam)).*sqrt(
                gam*R*T_H); % isentropic pressure and speed
                of sound relation

            u_B=Ma_B3.*a_B3;

            PI_s1NEW = 1 + gam.*u_B./(a_A1.*sqrt((2.*gam/(
                gam+1))./(PI_s1+(gam-1)./(gam+1)))); %EQ h2

            count_1= count_1 +1;

            if count_1 > 1e4 % break loop if not
                converging
                ERROR=1;
                fprintf(2,'\n\n!! While Loop S1 ERROR !! '
                    );
                break
            end

        end
    end

    u_S1_1 = a_A1*sqrt((gam+1)/2/gam*(PI_s1-1)+1);   %
        shock wave speed
    u_S1_2 =a_A2*sqrt((gam+1)/2/gam*(PI_s1-1)+1);

```

```
    T_B1 = PI_s1*((gam+1)/(gam-1)+PI_s1)/(1+(gam+1)/(gam-1)*PI_s1)*T_A1;

    T_B2 = PI_s1*((gam+1)/(gam-1)+PI_s1)/(1+(gam+1)/(gam-1)*PI_s1)*T_A2;

    T_B3 = T_H/(1+(gam-1)/2*Ma_B3^2); % isentropic temp and mach number relation

    a_B1=sqrt(gam*R*T_B1);    % isentropic temp and speed of sound relation

    a_B2=sqrt(gam*R*T_B2);    % isentropic temp and speed of sound relation

    t_x1 = t_Ho + x1/u_S1_1; % time shock crosses interface

    t_Mo = t_x1 +(1-x1)/u_S1_2; % opening time of M port

%% expansion wave E_1

    a_C1 = (P_M/P_B)^((gam-1)/(2*gam))*a_B1;
    u_C1 = (2*a_B1-2*a_C1+(gam-1)*u_B)/(gam-1); % conditions in sub zone C1
    Ma_C1 = u_C1/a_C1;

    a_C2 = (P_M/P_B)^((gam-1)/(2*gam))*a_B2;
    u_C2 = (2*a_B2-2*a_C2+(gam-1)*u_B)/(gam-1); % conditions in sub zone C2
    Ma_C2 = u_C2/a_C2;

    a_C3 = (P_M/P_B)^((gam-1)/(2*gam))*a_B3;
    u_C3 = (2*a_B3-2*a_C3+(gam-1)*u_B)/(gam-1); % conditions in sub zone C3
    Ma_C3 = u_C3/a_C3;
```

```
    P_C1 = P_M;
    P_C2 = P_M;     % assuming the pressure in zone C1, C2
        and C3 is = to M pressure
    P_C3 = P_M;

    T_C1 = (a_C1/a_B1)^2 * T_B1;
    T_C2 = (a_C2/a_B2)^2 * T_B2;
    T_C3 = (a_C3/a_B3)^2 * T_B3;

% wave head calcs

    x2 = u_B*(t_Mo-t_Ho);  % Location of x2

    x3 = u_B*(t_Mo-t_x1) +x1; % Location of x3

    t_x5 = (l-x3)/a_B2; % time from M to x5

    x5 = l- t_x5*(a_B2-u_B); % location of x5 when wave
       head crosses interface

    t_x4 = (x3-x2)/a_B1; % time from x5 to x4

    x4 = x5- t_x4*(a_B1-u_B); % location of x4 when wave
       head crosses interface

    t_Hc = t_Mo + t_x5 +t_x4 + x4/(a_B3-u_B); % time head
       reaches the divider wall

% tail of wave calcs
    t_x5t =(l-x3)/a_C3;

    x5t = l - (a_C3-(u_B+u_C2)/2)*t_x5t;

    t_x4t = (x3-x2)/a_C1; % time from x5 to x4

    x4t = x5t- t_x4t*(a_C1-(u_B+u_C1)/2); % location of x4
        when wave tail crosses interface
```

```

    t_tailE1  = t_Mo + t_x5t +t_x4t + x4t/(a_C3-(u_C3)/2); % time tail reaches the divider wall
    t_Lo =t_tailE1;
%% expansion wave E_2
    x_=( t_Hc - t_Mo- t_x5t - t_x4t ) *(a_C3-u_C3); % location of x'

    a_x = (a_B3+a_C3)/2;
    u_x = (u_B + u_C3)/2;

    x = x_/(1+(a_C3-u_C3)/(a_x+u_x)); % x distances

    t_x =x/(u_x+a_x); % time to cross x

    t_Mc = t_Hc+ t_x +  (1-x)/(u_C3+a_C3);   % head hits wall

    a_C4 = a_C3+(gam-1)/2 *(-u_C3);  %  flow behind wave zero

    T_C4 = a_C4^2  /(R*gam);

    P_C4 = (a_C4/a_C3)^(2*gam/(gam-1)) *P_C3;
%% shock wave S_2
    PI_s2NEW  =3; % values to start loop
    PI_s2 = 2; % values to start loop
    count_1 = 0;
    while round(PI_s2,3)~=round(PI_s2NEW,3)
        PI_s2 = (PI_s2+PI_s2NEW)/2;

        P_D=PI_s2*P_C4; % finding pressure in D2

        if P_D > P_L
          PI_s2NEW=PI_s2/1.1;
        else

```

```
                Ma_D1 = sqrt( ((P_L/P_D)^((gam-1)/gam)-1)*2/(
                    gam-1));

                a_D1 = (P_D/P_L)^((gam-1)/(2*gam))*sqrt(gam*R*
                    T_L); % isentropic pressure and speed of
                    sound relation

                u_D=Ma_D1*a_D1;

                PI_s2NEW = 1 + gam*u_D/(a_C4*sqrt((2*gam/(gam
                    +1))/(PI_s2+(gam-1)/(gam+1))));

                count_1= count_1 +1;
            end
            if count_1 > 1e4
            ERROR=1;
            fprintf(2,'\n\n!! While Loop S2 ERROR !! ');
            break
            end

        end
        u_S2 = a_C4*sqrt((gam+1)/2/gam*(PI_s2 -1)+1);  % sock
            wave speed

        T_D1 = T_L/(1+(gam-1)/2*Ma_D1^2); % isentropic temp
            and mach number relation

        T_D2 = PI_s2*((gam+1)/(gam-1)+PI_s2)/(1+(gam+1)/(gam
            -1)*PI_s2)*T_C4;

        a_D2 = sqrt(gam*R*T_C4);
%%% shock 3
        PI_s3NEW =2;
        PI_s3 = 0;
        count = 0;
        while round(PI_s3,3)~=round(PI_s3NEW,3)
            PI_s3 = PI_s3NEW;
```

```
            PI_s3NEW = 1 + (u_D/a_D2)* gam * sqrt(((gam+1)/(2*
                gam))*PI_s3+(gam-1)/(2*gam));
            count= count +1;
        end
        W_s3_D2=a_D2*sqrt((gam+1)/(2*gam) *(PI_s3 -1)+1);
        W_s3_D1=a_D1*sqrt((gam+1)/(2*gam) *(PI_s3 -1)+1);

        u_s3_D2 = W_s3_D2 - u_D;
        u_s3_D1 = W_s3_D1 - u_D;

        x9 = u_D*(t_Mc-t_Lo);

        t_x1D2 = (1-x9 )/W_s3_D2;

        t_x1D1 = (1-u_s3_D2*t_x1D2)/u_s3_D1;

        t_Lc = t_Lo+ 1/u_S2 + t_x1D1+t_x1D2;

        x1 =x9+u_D*t_x1D2;
%%
        P_A = PI_s3*P_D;
        T_A1=PI_s3*(  ((gam+1)./(gam-1)+PI_s3) ./ (1+ ((gam+1)
            ./(gam-1))*PI_s3))*T_D1;
        T_A2=PI_s3*(  ((gam+1)./(gam-1)+PI_s3) ./ (1+ ((gam+1)
            ./(gam-1))*PI_s3))*T_D2;
        a_A1 = sqrt(gam*R*T_A1);
        a_A2 = sqrt(gam*R*T_A2);

        if P_A > P_H
            P_A = P_H*.99;
        end

%% Breaks the for loop if converged
        cont_1(ii) = P_A;
        cont_2(ii) = T_A1;
        if ii > 15
            PA = std(cont_1(end-5:end))/mean(cont_1(end-5:end)
```

```
            ); % pressure standard deviation / mean
        TA = std(cont_2(end-5:end))/mean(cont_1(end-5:end));
    if (PA < 1e-3 && TA < 1e-6)
        break
    end
    end

end
%% mass per unit A
%H port
t_B3 = t_Hc-t_Ho;
m_H = P_B*Ma_B3*sqrt(gam/(R*T_B3))*t_B3;
%M port mass is attemted to be calculated as a check results
t_C2 =((1-x5t)/(u_C2+u_C1)/2)+t_x5t;
m_C2 = P_C2*Ma_C2*sqrt(gam/(R*T_C2))*t_C2;

t_C1 = ((1-x4t)/(u_C1))-t_C2+t_x4t;
m_C1 = P_C1*Ma_C1*sqrt(gam/(R*T_C1))*t_C1;

t_C3 =t_Mc -t_Mo -t_C2 -t_C1;
m_C3 = P_C3*Ma_C3*sqrt(gam/(R*T_C3))*t_C3;

m_M =m_C1+m_C2+m_C3;

m_L =P_D*Ma_D1*sqrt(gam/(R*T_D1))*(t_Lc -t_Lo);

massNET = ((m_L+m_H)/m_M-1 )*100;

if massNET > 16 % checking continuity (if < 16% the result is discarded)
    ERROR=1;
    fprintf(2,'\n\n!! Mass ERROR !! \n');
end

if ERROR == 1 % if error has occurred the solution is
```

```
    cancelled
        z = nan;
        n = nan;
else
        z = m_L*T_L/(m_H*T_H)  % performance parameter
        n = z*(   ((P_M/P_L)^((gam-1)/gam)-1)/(1-(P_M/P_H)^((
           gam-1)/gam)))*100 % isentropic efficiency
end

%% Plotting on Kentfield data
figure(2)
img = imread('equliserMAP.PNG');
image('CData',img,'XData',[1 1.6],'YData',[1 0.5])
axis([1 1.6 0.5 1])
set(gca,'XAxisLocation','top')
hold on
labels = [' \eta = ' num2str(n/100,2)];
plot(P_H/P_M,P_L/P_M,'r*','LineWidth',4)
h=text(P_H/P_M,P_L/P_M,labels,'VerticalAlignment','bottom'
    ,'HorizontalAlignment','left');
set(h, 'Color','r','FontSize', 12)
labels = [' \zeta = ' num2str(z,2)];
h=text(P_H/P_M,P_L/P_M,labels,'VerticalAlignment','top','
    HorizontalAlignment','left');
set(h, 'Color','r','FontSize', 12)
hold off
xlabel('P_0_H/P_0_M')
ylabel('P_0_L/P_0_M')
%% calculating port angles based on rotor speed and
    calculated port timing
N =5000; % rotor speed RPM
w = N/60 *2*pi; % angular rotor speed omega
Theta = rad2deg([t_Ho t_Mo t_Hc t_Lo t_Mc t_Lc]*w); % port
      opening angles
```

Appendix C

Additional Experimental Results Figures

C.1 Additional Performance Curves

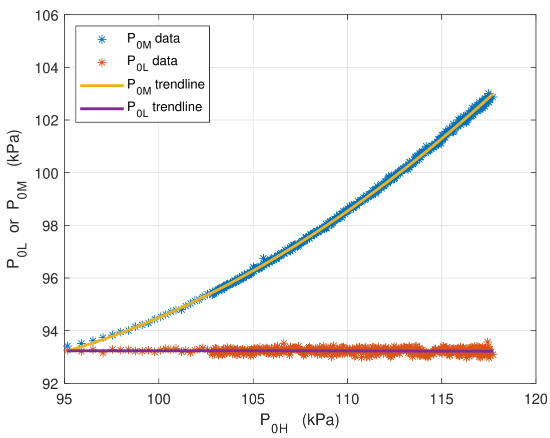

(a) Pressure trendline

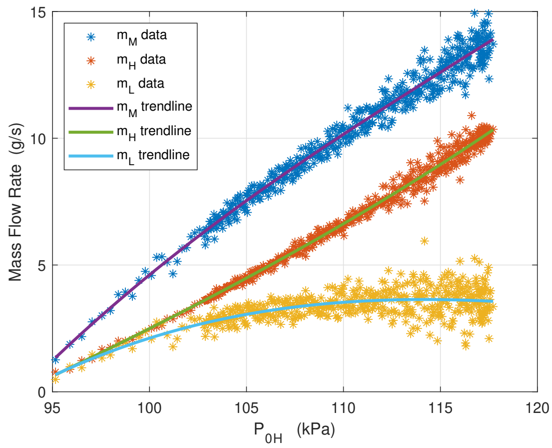

(b) Mass flow trendline

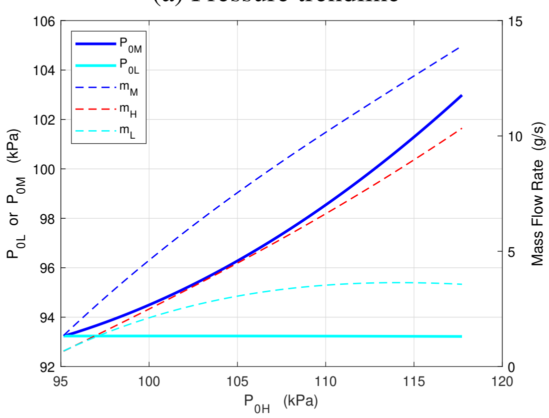

(c) Mass flow and pressure plot

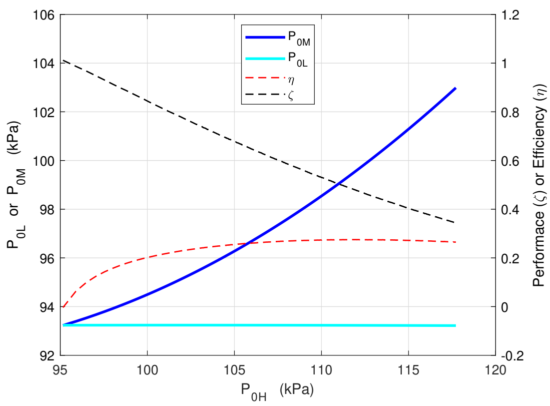

(d) Performance, efficiency and pressure plot

Figure C.1: Valve 90° performance curves

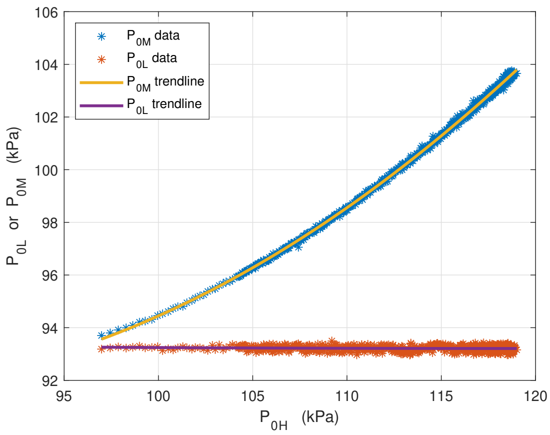

(a) Pressure trendline

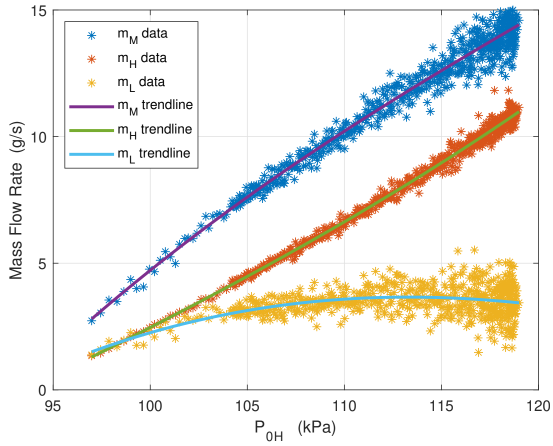

(b) Mass flow trendline

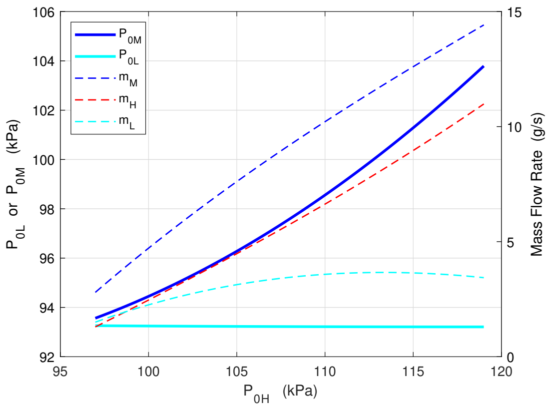

(c) Mass flow and pressure plot

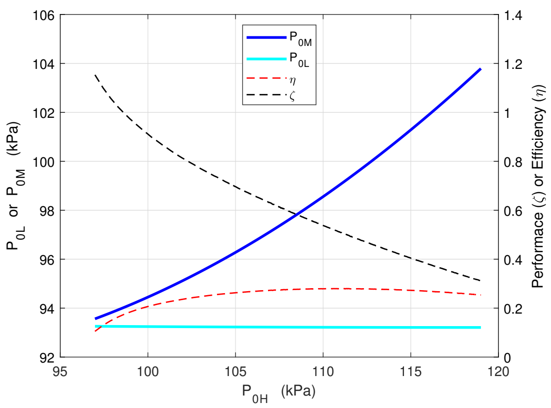

(d) Performance, efficiency and pressure plot

Figure C.2: Valve 80° performance curves

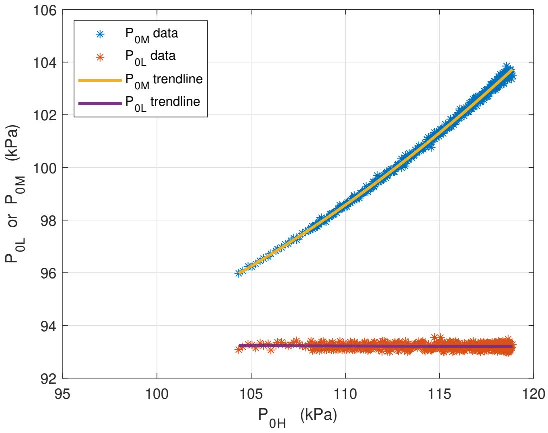

(a) Pressure trendline

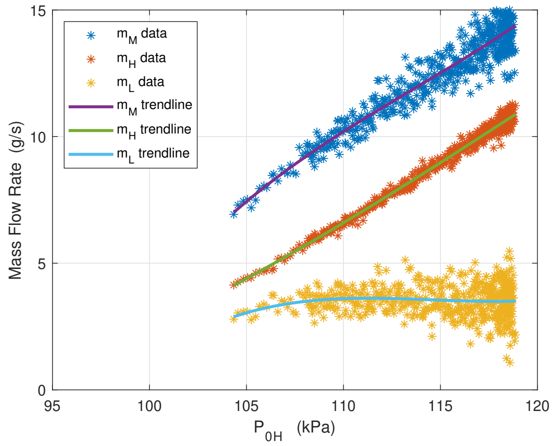

(b) Mass flow trendline

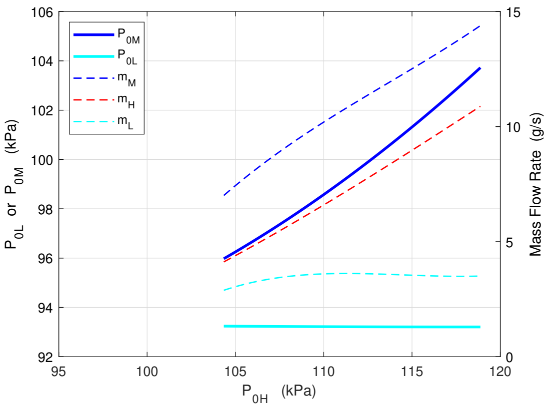

(c) Mass flow and pressure plot

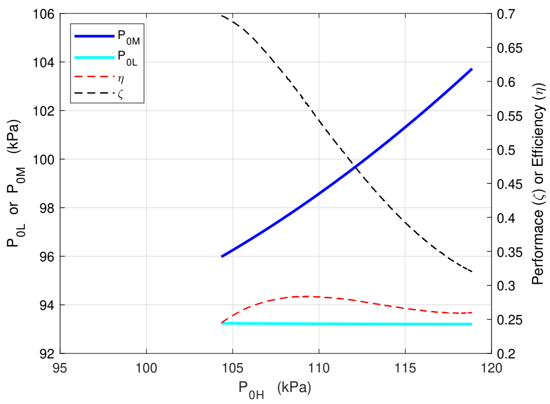

(d) Performance, efficiency and pressure plot

Figure C.3: Valve 70° performance curves

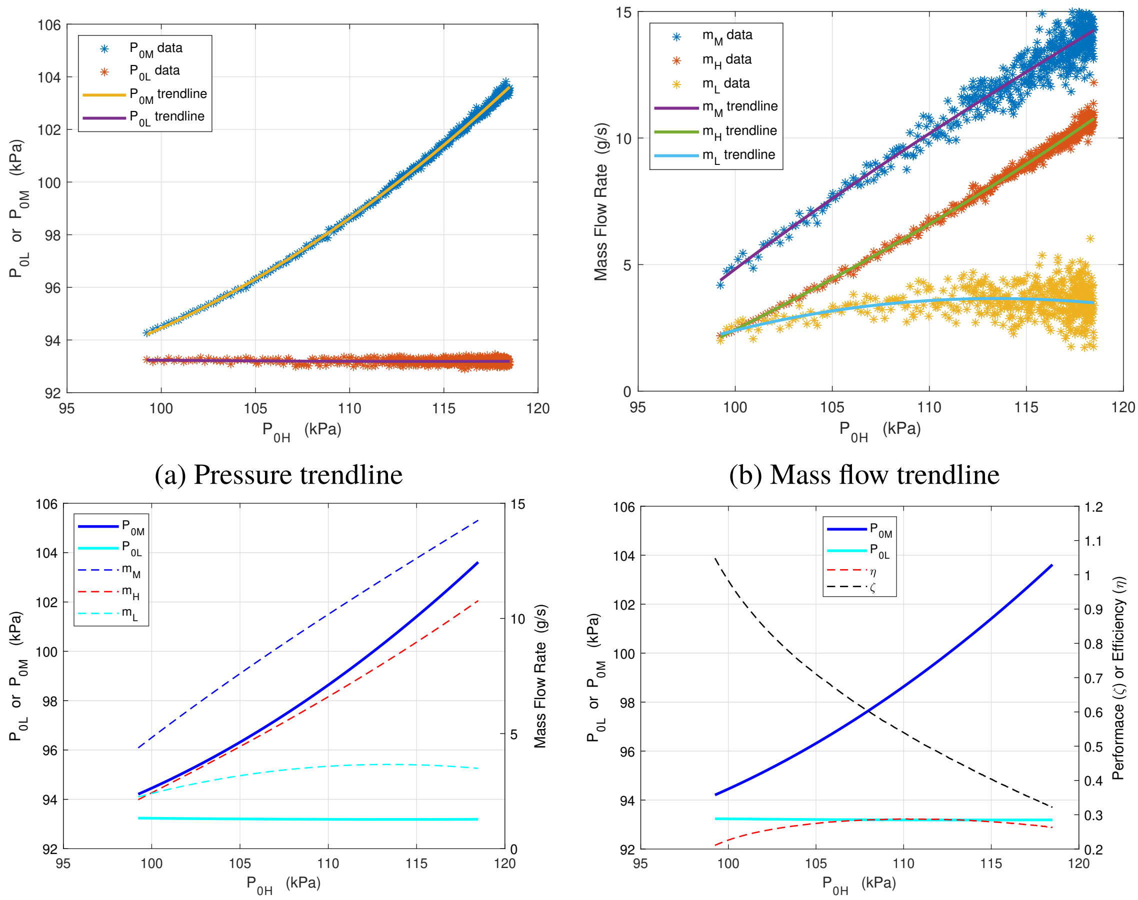

(a) Pressure trendline

(b) Mass flow trendline

(c) Mass flow and pressure plot

(d) Performance, efficiency and pressure plot

Figure C.4: Valve 60° performance curves

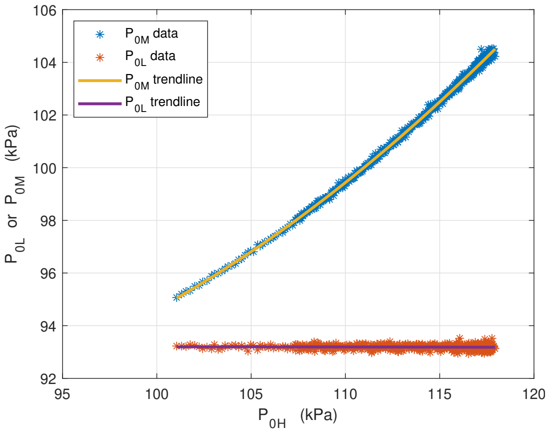

(a) Pressure trendline

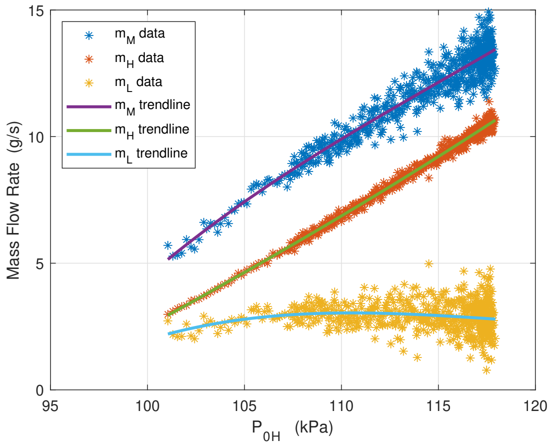

(b) Mass flow trendline

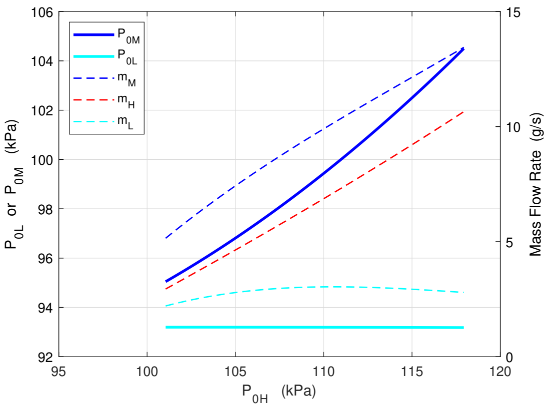

(c) Mass flow and pressure plot

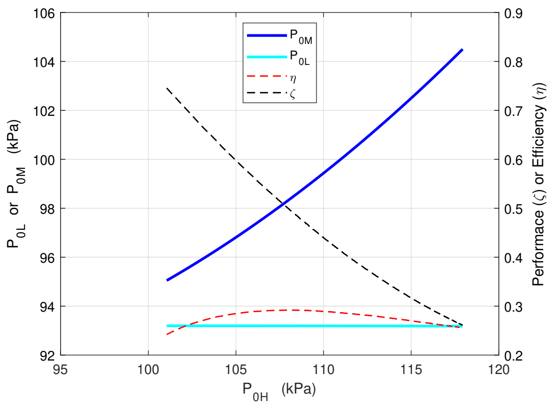

(d) Performance, efficiency and pressure plot

Figure C.5: Valve 40° performance curves

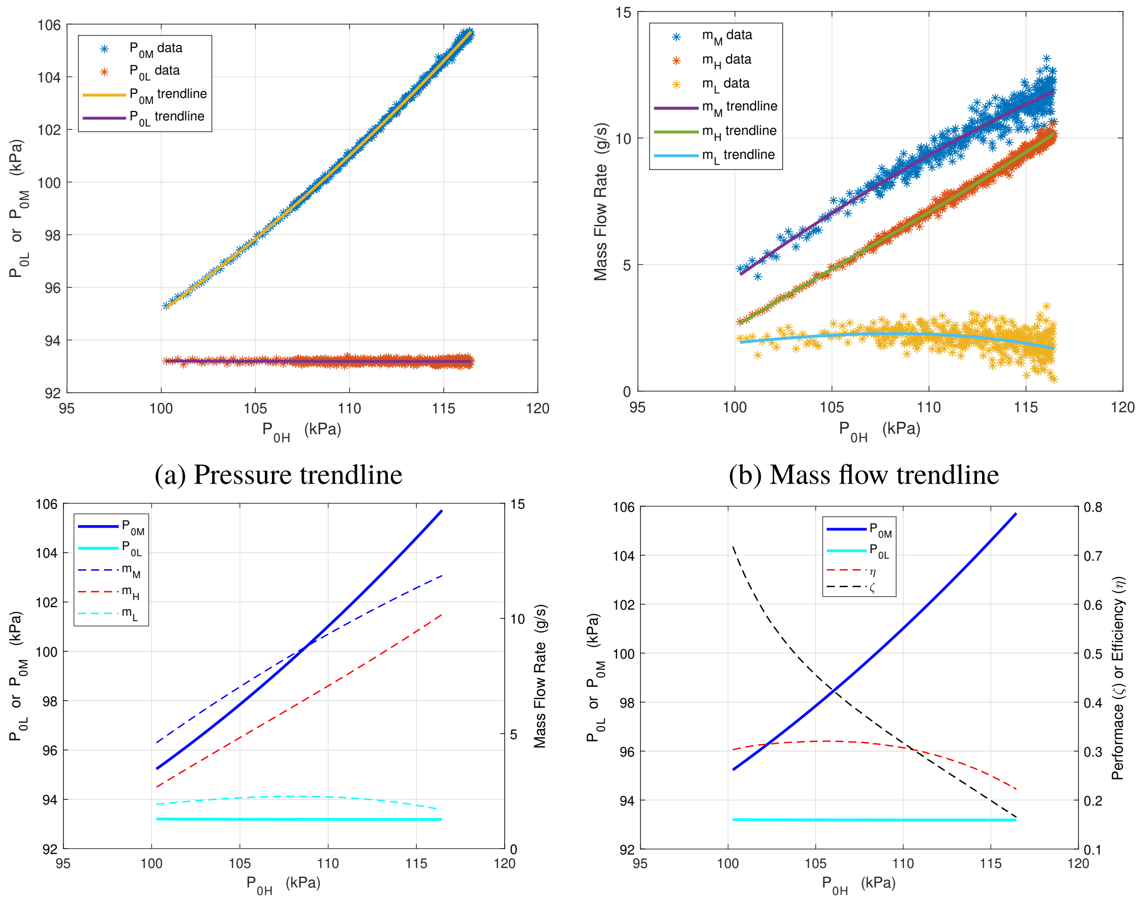

(a) Pressure trendline

(b) Mass flow trendline

(c) Mass flow and pressure plot

(d) Performance, efficiency and pressure plot

Figure C.6: Valve 30° performance curves

Appendix D

HPC Code

ANSYS Fluent Journal File Template

```
file read-case-data [CASE FILE NAME.cas]
solve dual-time-iterate [NUMBER OF TIME STEPS] [ITERATIONS PER TIME STEP]
file/auto-save/data-frequency [SAVE FREQUENCY]
solve set time-step [TIME STEP IN SECONDS]
solve dual-time-iterate [NUMBER OF TIME STEP TO SOLVE] [MAX ITERATIONS PER TIME STEP]
file write-case-data final.cas
exit
yes
```

HPC Job Script Template (modified from USQ HPC example code)

```
#!/bin/bash
#
#### Set shell
#PBS -S /bin/bash
#
#### Job Name
```

```
#PBS -N [NAME OF JOB]
#
#### Set default resources requirements for job
#### (40 processor on 2 node requesting 150 hours 30 minutes of runtime and 180G of ram)
#### - these can be overridden on the qsub command line
#PBS -l nodes=2:ppn=20
#PBS -l walltime=150:30:00
#PBS -l mem=180g
#
#### Request that regular output (stdout) and
#### terminal output (stderr) go to the same file
#PBS -j oe
#
#### Set mail options to send job notifications
#
#### Set the queue to run job on
#PBS -q default

#### Set number of processors to run on
#### (list of node names is in file $PBS_NODEFILE)
nprocs=`wc -l $PBS_NODEFILE | awk '{ print $1 }'`

#### Load ansys module so that we find the fluent command
module load ansys

#### Specifies the version of ANSYS FLUENT to run
version=3ddp

#### Specifies journal file to use
journal=[JOURNAL FILE NAME]

#### Change to the directory from which you submitted the job
cd $PBS_O_WORKDIR

#### Start computation
```

```
fluent $version -t$nprocs -cnf=$PBS_NODEFILE -g -i
    $journal
```

Appendix E

CFD Assignment

This assignment material is included here to demonstrate a simple and basic alternative method. While the PEEWR device which is the subject of the dissertation was also work for credit towards the course MEC5100, the work performed for the dissertation, while building on the MEC5100 material is substantially different and more sophisticated.

Wave Rotor Simulation

Assignment 3

Computational Fluid Dynamics
MEC5100

Semester 1

2019

Liam Channer

Sn. U1085095

Table of Contents

Introduction / Background

A wave rotor is a device used for pumping gas though the manipulation of shock and expansion waves generated by the rapidly changing boundary conditions. Each channel in a wave rotor can be thought of as a shock tube which gets opened and closed to different pressure gasses creating shock and expansion waves. The opening and closing of the channel is manipulated so the waves create a pumping effect.

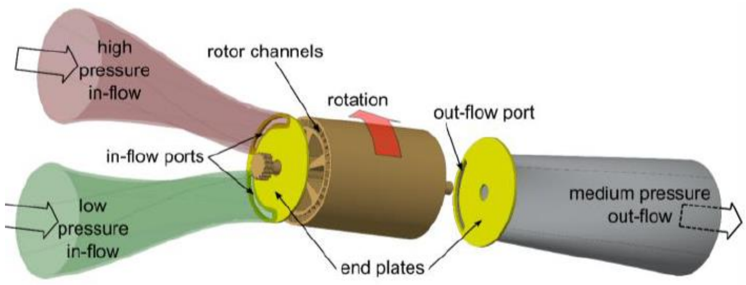

Figure 1 Wave rotor (Source: David Buttsworth)

Referring to the above figure each channel goes through the following cycle: high pressure opens, medium pressure of opens, high pressure closes, low pressure opens, medium pressure closes, and low pressure closes.

Aim

The aim of the project is to setup a simulation of one channel in a wave rotor and analyse the fluid flow over time. The geometry and boundary conditions are based on a wave rotor currently been tested at P10 USQ. The focus is on developing a suitable methodology for simulating the fluid flow in a channel. Further work will be conducted as part of my final year project.

Simplifications

The CFD simulations will have several simplifications. The ports will be either open or closed where in reality the ports would open and close over time. Also, to reduce computational cost the simulation will be conducted as a two-dimensional model. Other factors such as heat transfer from the channel walls and leakage between the channels and endplates are ignored.

Geometry

The rotor channels are 5mm by 5mm square by 150mm long. To minimise element numbers the channel will simulated two-dimensionally and with symmetry. Therefore, as presented in figure 2 the geometry will be 2.5mm by 150mm surface.

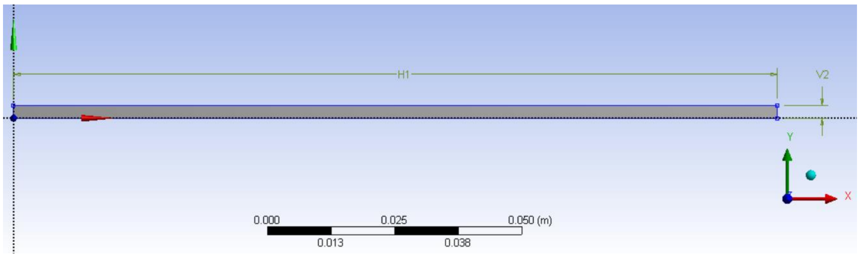

Figure 2 Geometry: H1 = 150mm and V2 = 2.5mm

Three dimensional simulations are generally more realistic. However, the added computational cost of a 3d simulation and nature of the case been simulated it is deemed that 2d simulation is a reasonable simplification. Also, with moving shock and expansion waves the smaller the elements the better as the waves can be further resolved. Hence, using the extra element numbers to reduce the element size in a 2D simulation would be better spent than investing in a 3D simulation.

Mesh

The mesh was generated using defaults setting except changing the max element size to 0.5mm. This gave good quality mesh with square elements aligning exactly with one another.

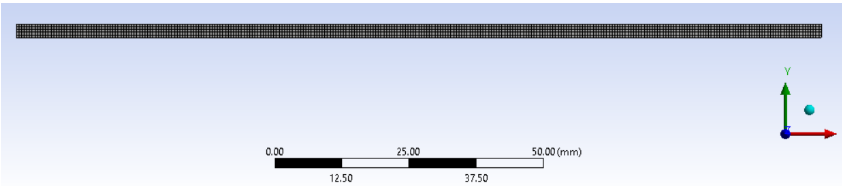

(a) Overall view

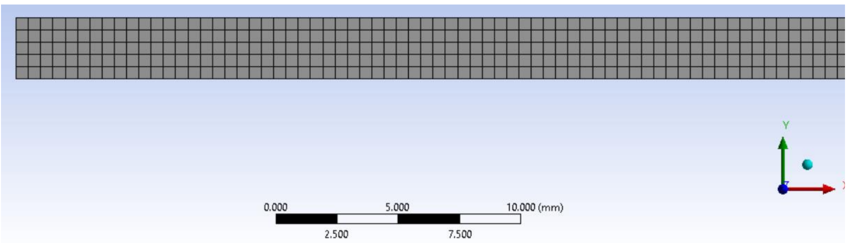

(b) Zoomed view

Figure 3 Mesh: 1806 nodes and 1500 elements

Smaller element would resolve the moving shock and expansion waves further. However, the smaller the mesh the smaller the time step. Hence, finer mesh takes longer to solve and requires to be solved for more time steps which increases the computational cost. Referring to figure 3a, the mesh is fine enough, so each element is hard to identify hence, variation across an element will be hard to see in the result.

The model used to solve the solution is inviscid hence, no need for wall inflations. Also, as the shock and expansion waves travel down the whole length of the channel, mesh refinements aren't relevant in this application unless a dynamic mesh is used.

Boundary Conditions

The model has 4 different boundary conditions: inlet, wall, symmetry and outlet. The location of each boundary condition is displayed in figure 4.

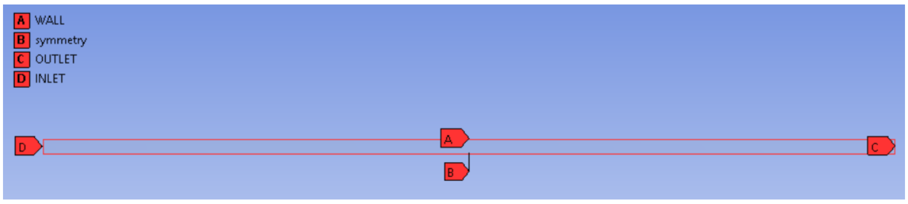

Figure 4 Channel boundary conditions

The wall defines the wall of the channel where the symmetry boundary condition is required as only half the channel is been simulated. Hence for the simulation to solve correctly the solver needs to know about the symmetry.

The inlet boundary will be a pressure inlet when the high or the low-pressure port is open and a wall to when closed. Similarly, the outlet will be a pressure outlet when the medium pressure port is open and a wall when closed.

Pressure inlets and pressure outlets where used as the design pressure is known for each port.

The inlet and outlet boundary conditions are summarised in the following table with respect to time.

The rotor spins at 5000 RPM therefore the rotor rotates one degree in:

$$t_d = \frac{60}{5000} / 360 = 33.333 \times 10^{-6} s / degree$$

Table 1 Boundary conditions: inlet and outlet

Degrees of rotation	Inlet boundary	Outlet boundary	Time (ms)	Time steps
Initial state (channel pressure 80kPa abs)	wall	wall		
0	High pressure port opens: Pressure inlet 200kPa abs		0	0
12		Medium pressure port opens: Pressure inlet 140kPa abs	0.4	600
27	High pressure port closes: Wall		0.9	1350
33	Low pressure port opens: Pressure inlet 80kPa abs		1.1	1650
43.5		Medium pressure port closes: Wall	1.45	2175
58	Low pressure port closes: Wall		1.9333	2900
360	Same as 0 degrees	Wall	12	18000

It must be noted that in reality the inlet and outlet will open gradually over time hence changing the inlet and outlet boundary condition instantly is a simplification.

The time step used in the simulation is $t_s = 6.666\times10^{-7} s$ so 50 time steps is one degree of rotation. The solver used is implicit. Hence, the time step needs to be sufficiently small, so nothing skips a mesh cell. The rule of thumb is nothing should travel further than half a cell. The fastest event is the speed of the fist shock wave which can be calculated as follows:

Speed of sound:

$$a_1 = \sqrt{\lambda RT} = \sqrt{1.4\times287\times300} = 347.2m/s$$

Wave speed (P_2 was found when conducting a preliminary simulation)

$$W = a_1\sqrt{\frac{\gamma+1}{2\gamma}\left(\frac{P_2}{P_1}-1\right)+1} = 347.2\sqrt{\frac{1.4+1}{2\times1.4}\left(\frac{162}{80}-1\right)+1} = 476.5m/s$$

Therefore, with the time step of 0.666us the distance travelled is:

$$x = Wt_s = 476.5\times6.666\times10^{-7} = 317.67\mu m = 0.3mm$$

This is a bit more than half the 0.5mm cell length however, as the time step gives hole integers for changing boundary conditions it will be accepted.

Simulation Setup and Solving

Inviscid model was used for solving the simulation, so the results match hand calculations (hand calculations are based on Euler equations) and the shock and expansion waves can be seen clearly in the results. Neglects fluid viscosity in this application is deemed to be a reasonable assumption. Also, in literature Inviscid model is the popular choice.

The simulation was solved using Fluent with the following setup: Density based solver, transient, energy on, inviscid model. material set to air ideal gas. The solution method was set to implicit and second order with the residual absolute criteria set to 1e-5. The operating conditions set to absolute. i.e. operating pressure set to zero. The max iterations per time step was set to 200.

Reporting definitions where set up to record and write an output file for the following variables: flow time, iterations per time step, mass flow rate, pressure and total pressure for both the inlet and outlet.

The simulation was initialised with the initial values: pressure = 80kPa, velocities = 0 and temperature = 300K.

Under the Calculations Activities the Autosave was set to 25 time steps which means a solution file is saved every half degree of rotor rotation.

Under Calculation Activities – Execute Commands a macro is defined to change the boundary conditions based on time steps using Text User Interface (TUI). The command is set to execute the macro every time step which runs through the following code:

```
;open high pressure inlet
(if (= (rpgetvar 'time-step) 0)
(ti-menu-load-string (format #f "define/boundary-condition/modify-
zone/zone-type inlet pressure-inlet")))
(if (= (rpgetvar 'time-step) 0)
(ti-menu-load-string (format #f "/define/boundary-
conditions/pressure-inlet inlet yes no 200000 no 200000 no 300 no
yes")))
;
;Opening outlet code  12 deg
(if (= (rpgetvar 'time-step) 600)
(ti-menu-load-string (format #f "define/boundary-condition/modify-
zone/zone-type outlet pressure-outlet")))
(if (= (rpgetvar 'time-step) 600)
(ti-menu-load-string (format #f "/define/boundary-
conditions/pressure-outlet ou/tlet yes no 140000 no 300 no yes yes
yes no no")))
;
;Code for setting closing inlet 27 deg
(if (>= (rpgetvar 'time-step) 1350)
(ti-menu-load-string (format #f "/define/boundary-
condition/modify-zone/zone-type inlet wall")))
;
;open low pressure inlet  33 deg
(if (>= (rpgetvar 'time-step) 1650)
(ti-menu-load-string (format #f "define/boundary-condition/modify-
zone/zone-type inlet pressure-inlet")))
(if (>= (rpgetvar 'time-step) 1650)
```

```
(ti-menu-load-string (format #f "/define/boundary-
conditions/pressure-inlet inlet yes no 80000 no 80000 no 300 no
yes")))
;
;Code for setting closing outlet  43.5 deg
(if (= (rpgetvar 'time-step) 2175)
(ti-menu-load-string (format #f "/define/boundary-
condition/modify-zone/zone-type outlet wall")))
;
;Code for setting closing inlet  58 deg
(if (>= (rpgetvar 'time-step) 2900)
(ti-menu-load-string (format #f "/define/boundary-
condition/modify-zone/zone-type inlet wall")))
```

The code above could be optimised however, as it works and limited time available to spend optimising it was left as above. On reflection rather than using time step for the if statements it would be advised to change to flow time, so the time step can be made independent of the code.

The code is written in Scheme. The syntax for changing the boundary conditions "/define/boundary-conditions/pressure-inlet inlet yes no 200000 no 200000 no 300 no yes" is developed by writing "/define/boundary-conditions/pressure-inlet inlet” into the Fluent console and answering the questions. The answers to the question are then added to the command string.

```
Console
/define/boundary-conditions/pressure-inlet inlet
(inlet)
Reference Frame: Absolute [yes]
Use Profile for Gauge Total Pressure? [no]
Gauge Total Pressure (pascal) [200000]
Use Profile for Supersonic/Initial Gauge Pressure? [no]
Supersonic/Initial Gauge Pressure (pascal) [200000]
Use Profile for Total Temperature? [no]
Total Temperature (k) [300]
Direction Specification Method: Direction Vector [no]
Direction Specification Method: Normal to Boundary [yes]

>
```

Figure 5 Console questions

The inlet total pressure is assumed to be equal to the static pressure. This assumption is reasonable as the cross-sectional area of the port is substantially bigger than the channel. When the experimental data is known the total pressure will be know by deriving it from measured static pressure and mass flow rate.

The residuals all dropped below 1e-5 for evert time step. It took between 8 and 20 iterations per time step. See following figure of the residual monitor for the first few time steps.

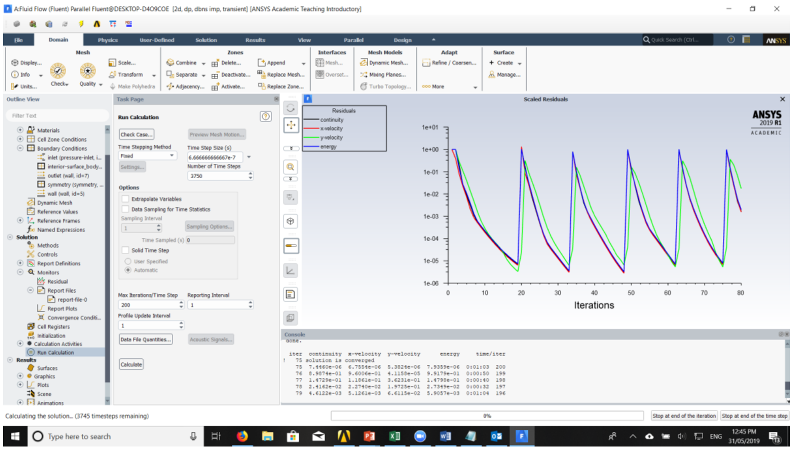

Figure 6 Residual monitor plot

The simulation was run for 3750-time steps which corresponds to 75 degrees of rotor rotation. This captures the opening and closing of all the ports and some time after. Simulating a full 360 degrees would require more computational time. Solving 3750-time steps took more than 30 hours. However, it was noticed that the more time steps that were solved the slower the simulation became. Stopping and then restarting the simulation improved the speed. Hence, stopping the simulation every 500 time steps would dramatically improve the computational time.

Mesh independence and results validation

The simulation was tested with a courser mesh to check mesh independence and validated by calculating the speed of the first shock and particle speed behind the shock wave. These tests are only carried out on the first part of the wave rotor cycle for reduced computational cost and calculation simplification.

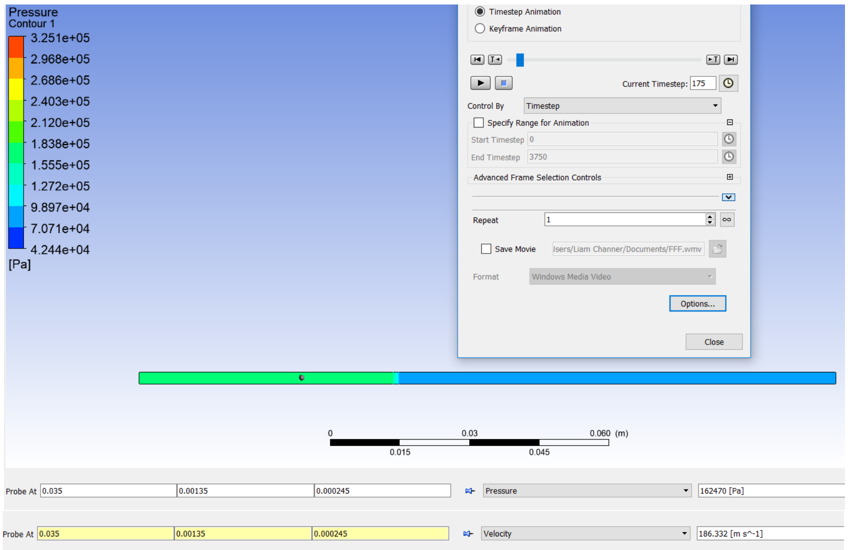

(a) Pressure and particle velocity behind the shock wave 1500 cell mesh

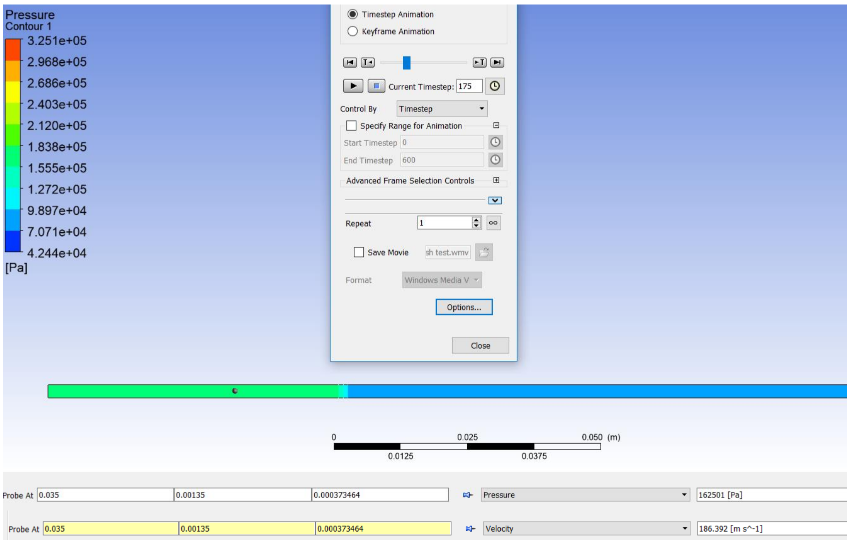

(b) Pressure and particle velocity behind the shock wave 600 cell mesh

Figure 7 Validation measurements

Hand calculations

Using pressures from figure 7.

Speed of sound:

$$a_1 = \sqrt{\gamma RT} = \sqrt{1.4 \times 287 \times 300} = 347.2 m/s$$

Shock wave speed main results:

$$W = a_1 \sqrt{\frac{\gamma+1}{2\gamma}\left(\frac{P_2}{P_1}-1\right)+1} = 347.2\sqrt{\frac{1.4+1}{2\times 1.4}\left(\frac{162470}{80000}-1\right)+1} = 476.51 m/s$$

Particle speed:

$$u_p = W\left(1-\frac{\rho_1}{\rho_2}\right) = \frac{a_1}{\gamma}\left(\frac{P_2}{P_1}-1\right)\left(\frac{\frac{2\gamma}{\gamma+1}}{\frac{P_2}{P_1}+\frac{\gamma-1}{\gamma+1}}\right)^{1/2} = \frac{347.2}{1.4}\left(\frac{162470}{80000}-1\right)\left(\frac{\frac{2\times 1.4}{1.4+1}}{\frac{162470}{80000}+\frac{1.4-1}{1.4+1}}\right)^{1/2} = 186.28 m/s$$

Shock wave speed mesh test results:

$$W = 347.2\sqrt{\frac{1.4+1}{2\times 1.4}\left(\frac{162501}{80000}-1\right)+1} = 476.56 m/s$$

Particle speed:

$$u_p = \frac{347.2}{1.4}\left(\frac{162501}{80000}-1\right)\left(\frac{\frac{2\times 1.4}{1.4+1}}{\frac{162501}{80000}+\frac{1.4-1}{1.4+1}}\right)^{1/2} = 186.35 m/s$$

Discussion

Table 2 Validation and mesh independence

Parameter	Main simulation	Mesh test simulation
Mesh cell	1500	600
Mesh cell length (mm)	0.5	0.75
Time step (us)	2/3	2/3
Pressure in front of shock wave (Pa)	80 000	80 000
Pressure behind the shock wave (Pa)	162470	162501
Particle velocity Fluent (m/s)	186.33	186.39
Particle velocity hand calc (m/s)	186.28	186.35
Calculated shock speed (m/s)	476.51	476.56

Referring to the above table. The particle velocity and pressure does not very significantly between mesh sizes. Also, the calculated particle velocity shows extremely good correlation. The first shock wave velocity is calculated to be almost identical for the two mesh sizes.

From the shock speed one can calculate the time the shock wave reaches the end of the channel. As the length of the channel is 150mm and the time step is 2/3 micro seconds the time step can be determined also.

$$t_f = \frac{0.15}{477} = 314 \times 10^{-6} s$$

$$t_{step} = 314/(2/3) = 471$$

The following figure shows the shock is traveling approximately at the calculated velocity. The closet recoded results file is at time step 475 where the shock has just been reflected. Looking at the recorded files either side of the 475 the as well 475 the actual is very close to the calculated speed.

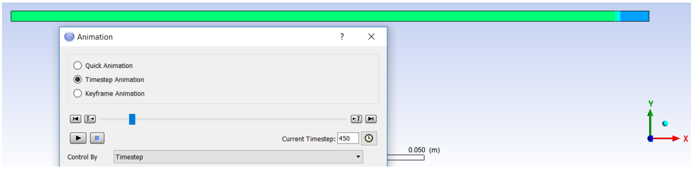

(a) Shock approaching end channel

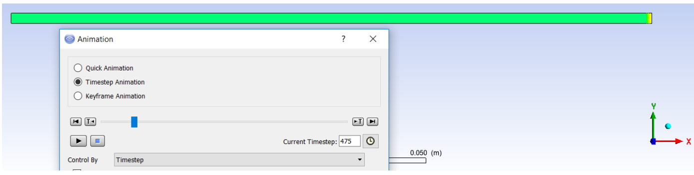

(b) Shock reached end of channel

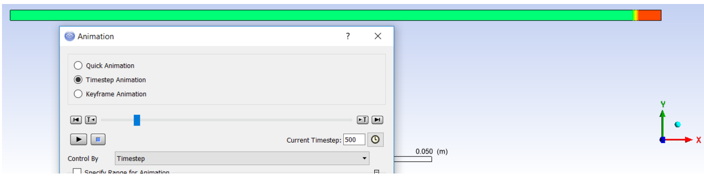

(c) Shock reflected

Figure 8 Validation of shock speed

Results

The main variables of interest of a wave rotor CFD simulation is the pressure and temperature contours in the channel and how they change over time. Partial velocity and port mass flow rates are also of interest. The best way to view these variables is though x t plots.

The results displayed in figure 9 follows expectation. The results show the medium pressure port is opening too late. Hence, the reflected shock wave instead of an expansion wave. The medium pressure port should open just before the primary shock wave reaches the end of the channel. It was determined earlier the shock wave reaches the end of the channel after approximately 471-time steps hence, the medium pressure port should open at time step 471 not 600. This delayed port opening does affect the rest of the cycle as the reflected shock wave slows the particle speed. This consequence can be seen clearly in figure 10 where the entrainment of low-pressure air is small and back flow is present. If the medium pressure port opens before the shock wave is reflected an expansion wave will occur rather than a reflected shock. This would increase the particle speed and improve entrainment of low pressure air.

The velocity vector in figure 9 are had to see hence please view in CFD Post or zoom in.

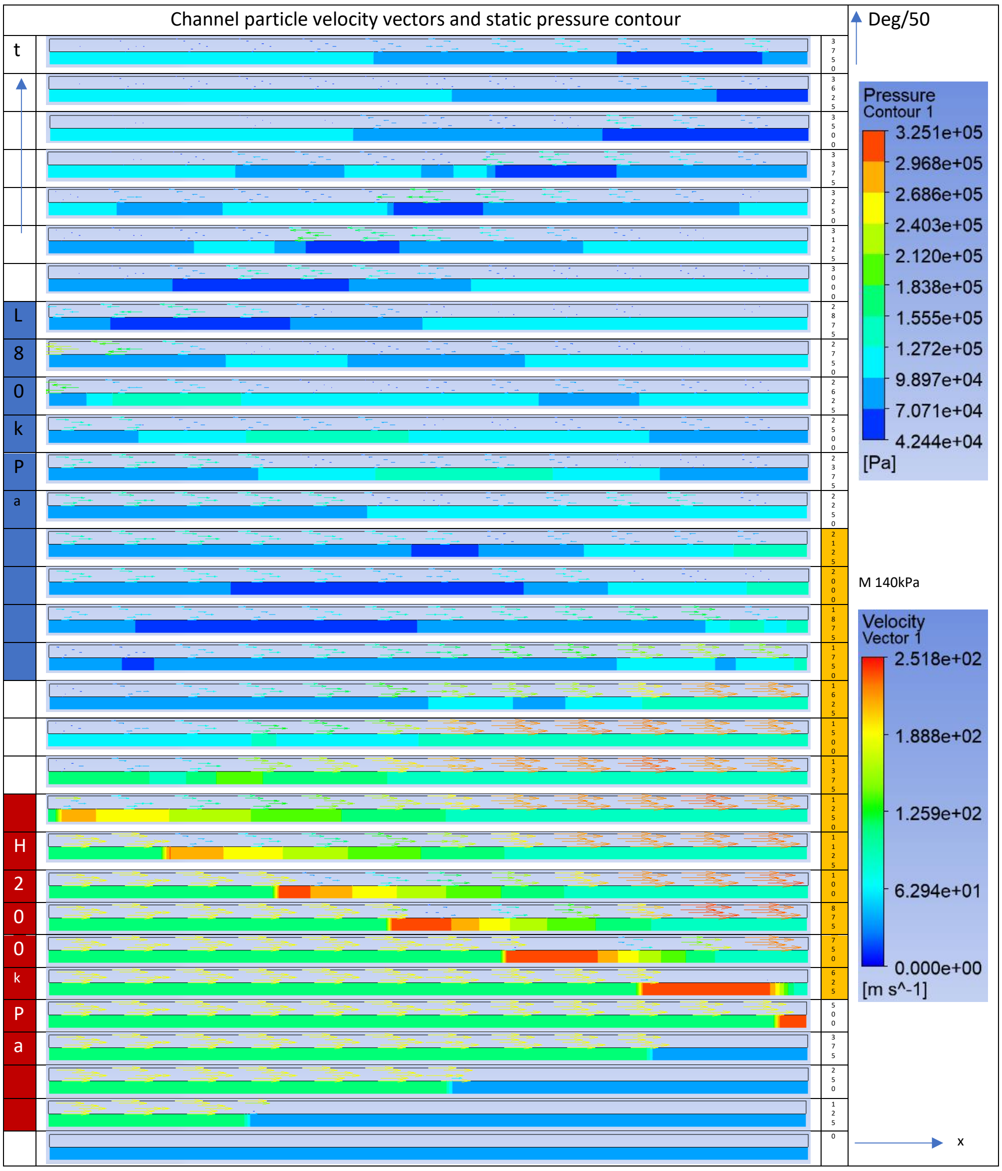

Figure 9 x t pressure and velocity plot

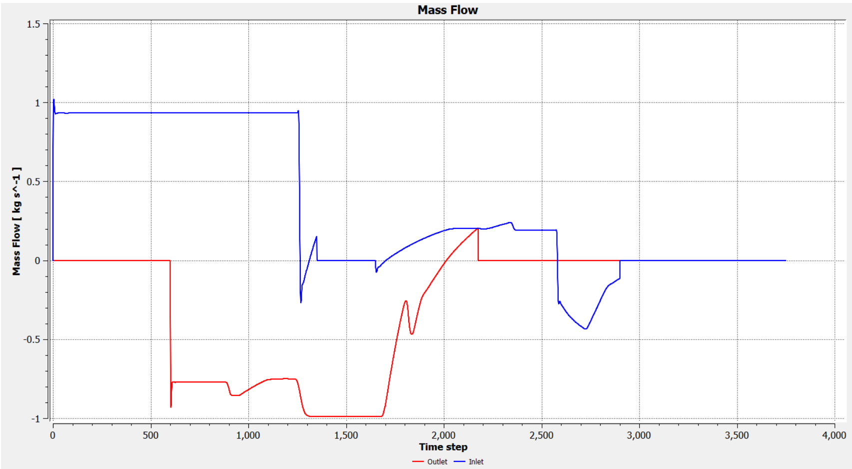

Figure 10 channel port mass flow rates (inlet = high pressure when < 1500-time steps else low pressure)

Figure 11 shows the temperature contour of in the channel and how it changes over time. The abrupt temperature change allows the interface between the original air in the channel, high pressure and low pressure air to be identified. This allows one to see how the particles travel through the channel. The interfaces have been marked in figure 12. One can clearly see the effect of the reflected shock wave and how it slows the particle speed.

The low pressure air entrainment by mass flow rate in figure 10 follows the same trend as looking at the interface between the air from the low pressure port and the air from the high pressure port in figure 12.

The particle velocity is presented in figures 13 and 14. Figure 13 shows the particle velocity in the positive x direction where figure 13 shows the particle velocity in the negative x direction. Splitting the particle velocity in two contour plots like this allows one to easily identify the direction of the flow.

Referring to figure 13. The negative flow just before the medium pressure port closes and the negative before the low-pressure port closes points to the ports closing too late.

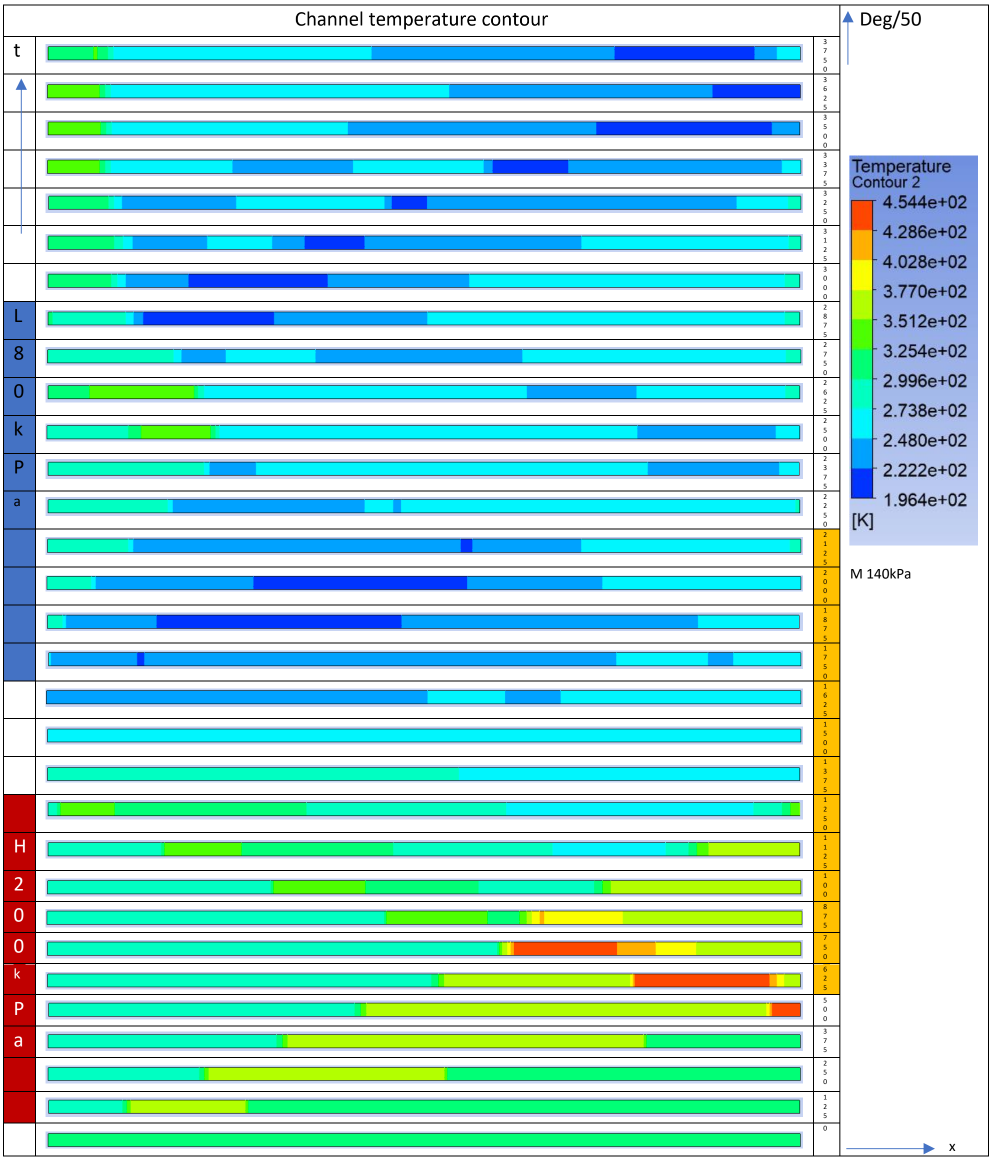

Figure 11 x t Temperature contour plot

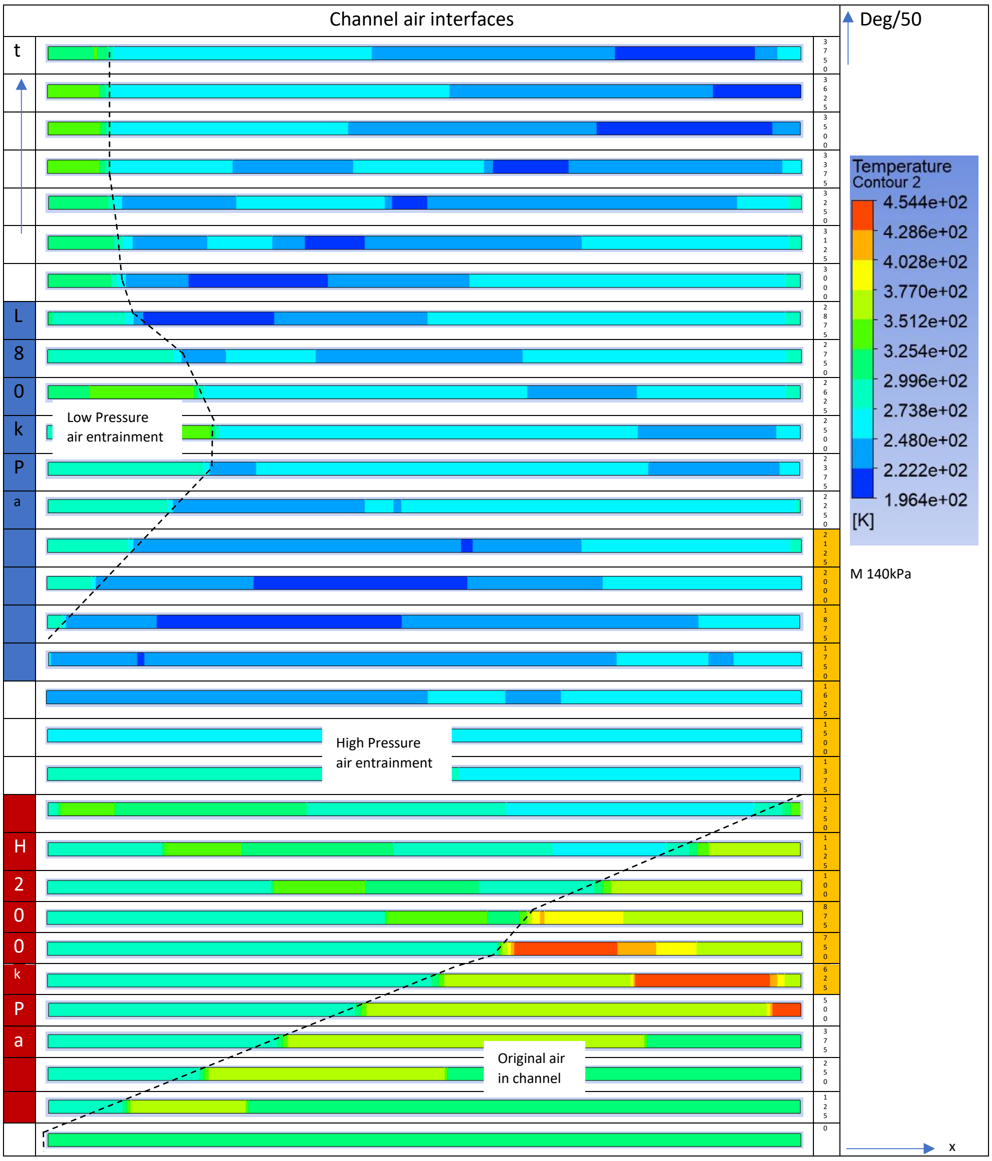

Figure 12 x t air interface in channel

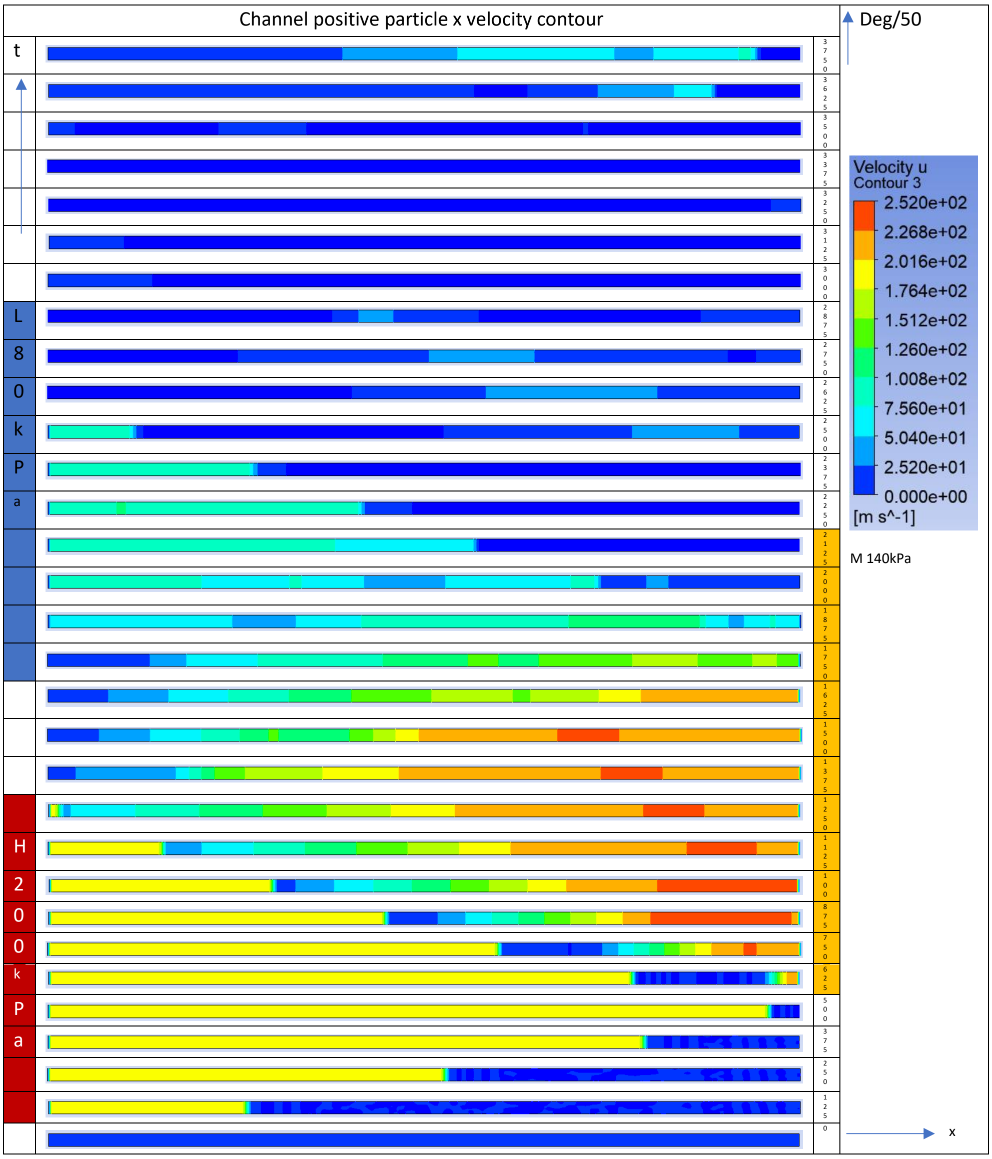

Figure 13 x t Positive particle velocity

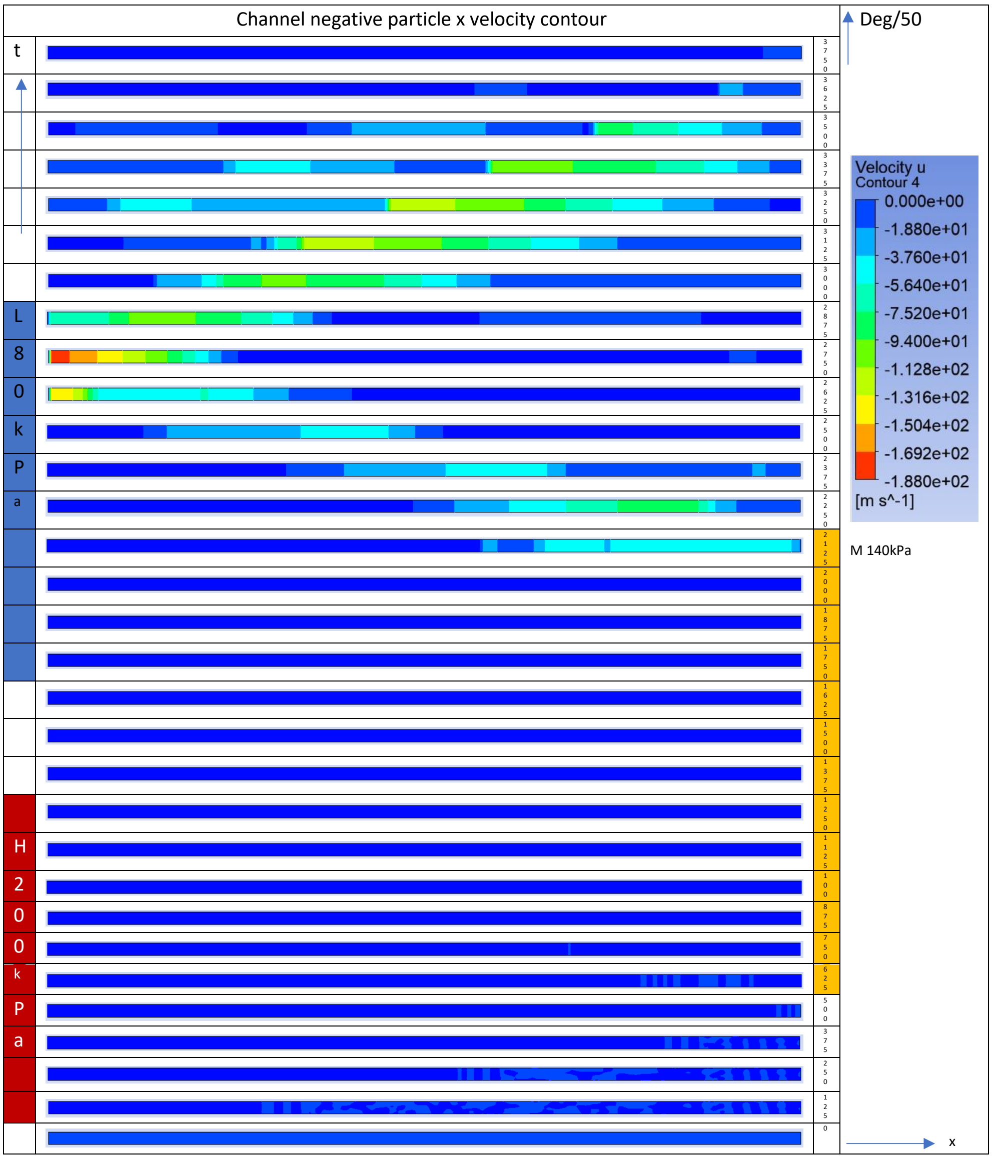

Figure 14 x t Negative x particle velocity

NOTE (project spec):

Comparing the results to results obtained using Elimer at USQ P10 is difficult as the port timing in this simulation needs correcting. Also, the boundary conditions used in the Elimer simulation is not known to me at this moment. Hence, the results will not be compared in this report.

Further work

The simulation setup and procedure developed during this project is robust enough for further simulations to be carried out. The next steps will be:

1. Determine the actual boundary conditions. This will be derived from measured results of the USQ P10 wave rotor once available.
2. Run the simulation with the actual boundary conditions and compare results with the measured results.
3. Adjust the port timing in the simulation so optimal performance is achieved. The corrected port timing will then be applied to the USQ P10 wave rotor and tested to see if this improves the actual performance of the device.
4. Simulating the device for multiple cycles could also be investigated. This would allow the pressure in the channel at the start of the cycle to be set to the pressure at the end of the last cycle which would be more realistic than assuming it to be the same as the low-pressure port.

Other areas to investigate would be including: gradual port opening, leakage and 3d channels in the simulation.

Appendix F

Additional CFD Figures

F.1 Porting Angle Effects Additional Contour Plots

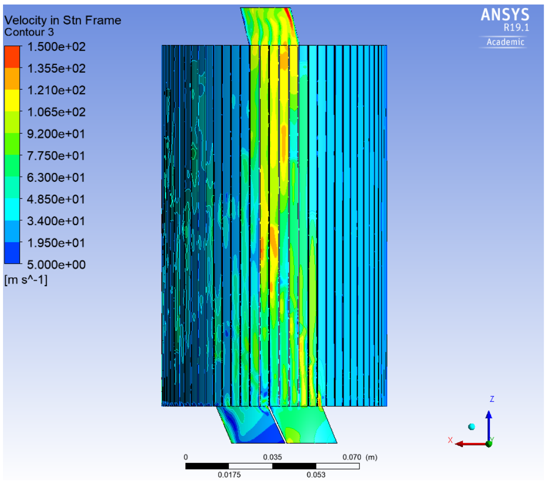

(a) Optimally angled

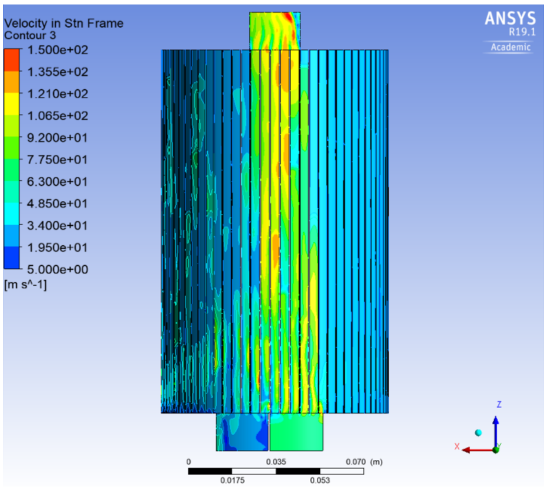

(b) Straight

Figure F.1: Velocity contour plot

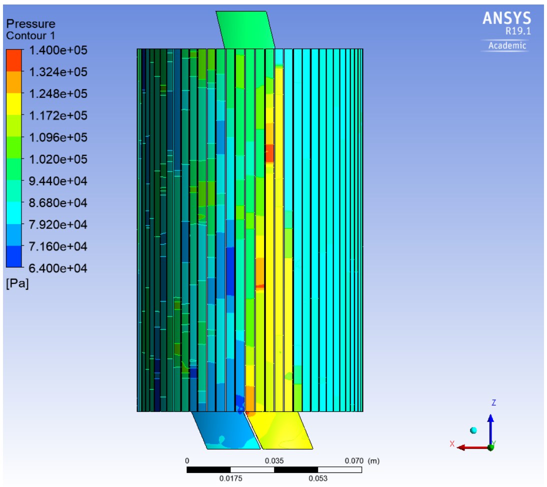

(a) Optimally angled

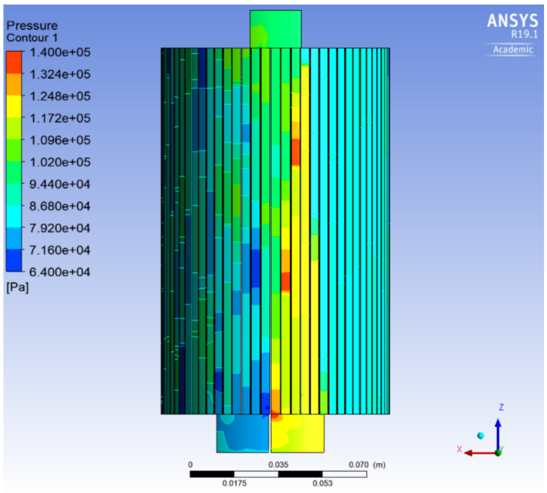

(b) Straight

Figure F.2: Pressure contour plot

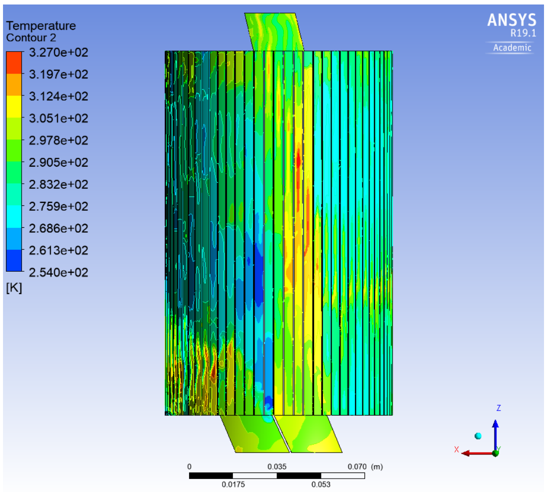

(a) Optimally angled

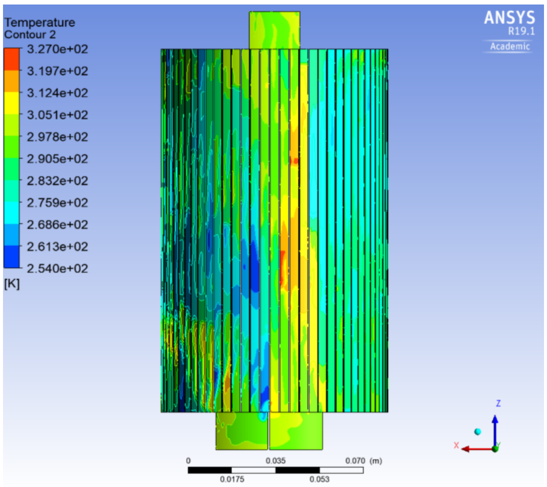

(b) Straight

Figure F.3: Temperature contour plot

F.2 3D CFD Additional Figures

F.2.1 Inviscid vs Laminar

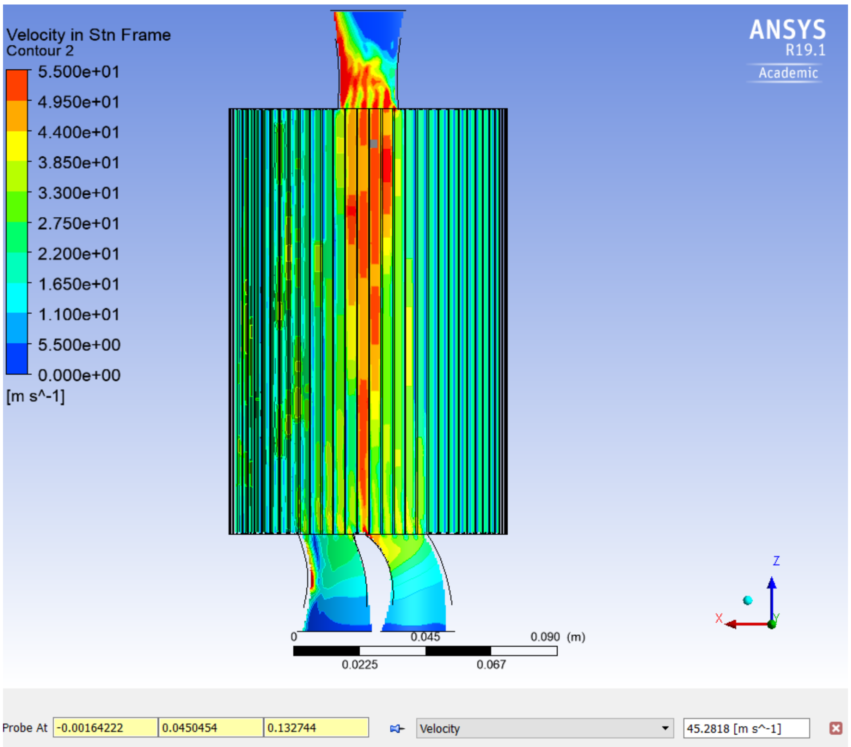

(a) Inviscid

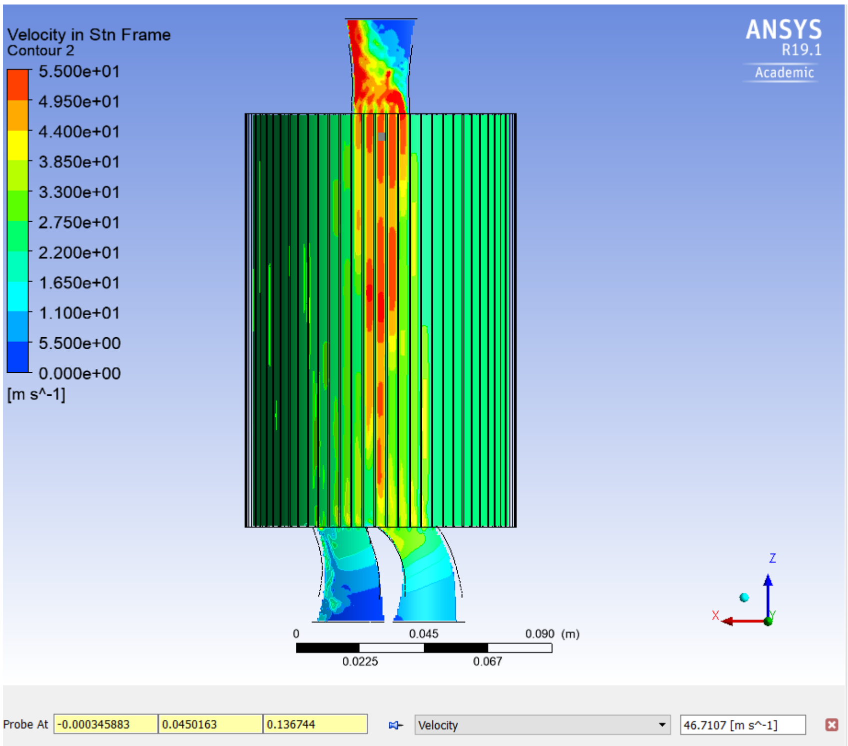

(b) Laminar

Figure F.4: Velocity contour at mean channel radius

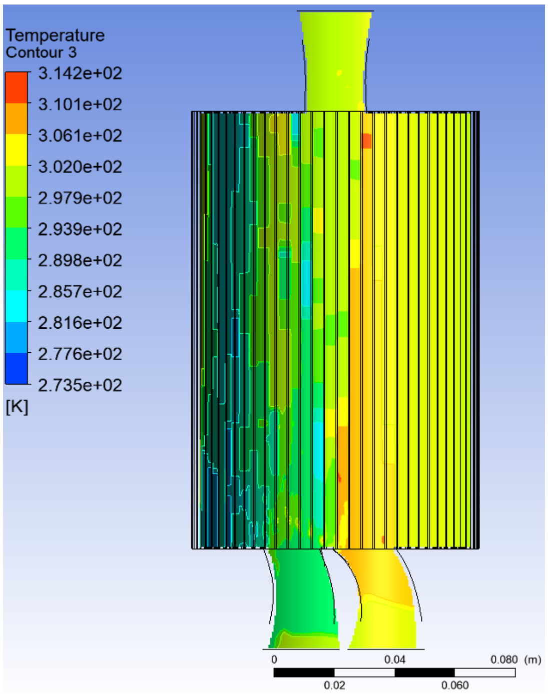

(a) Inviscid

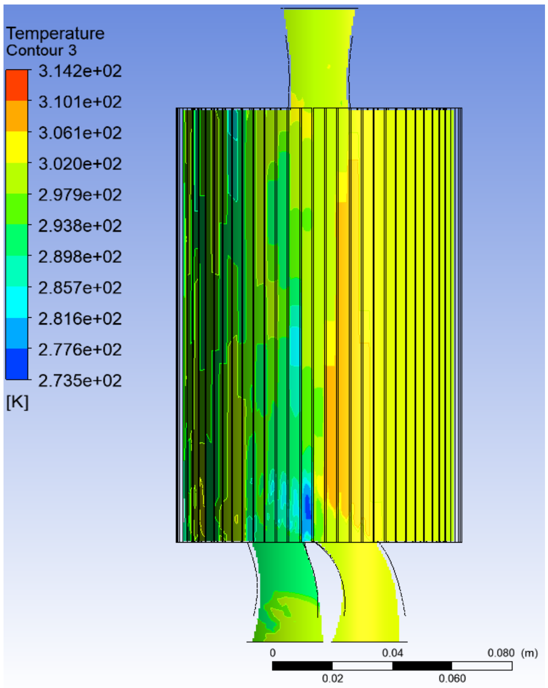

(b) Laminar

Figure F.5: Temperature contour at mean channel radius

F.2.2 Laminar

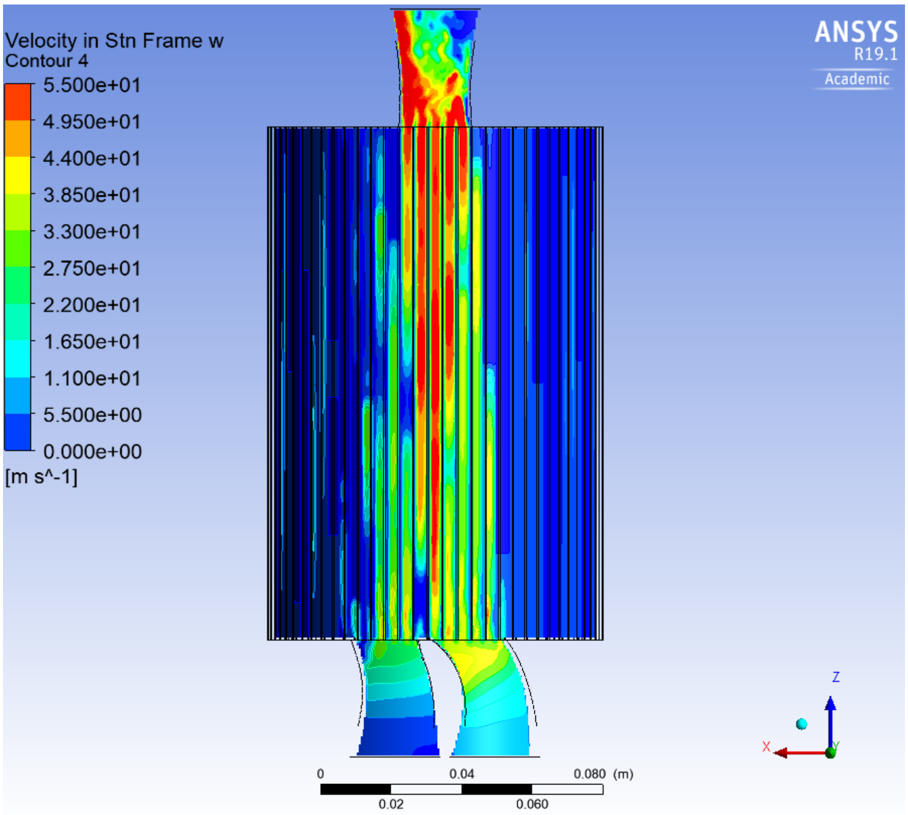

(a) Positive Z direction velocity

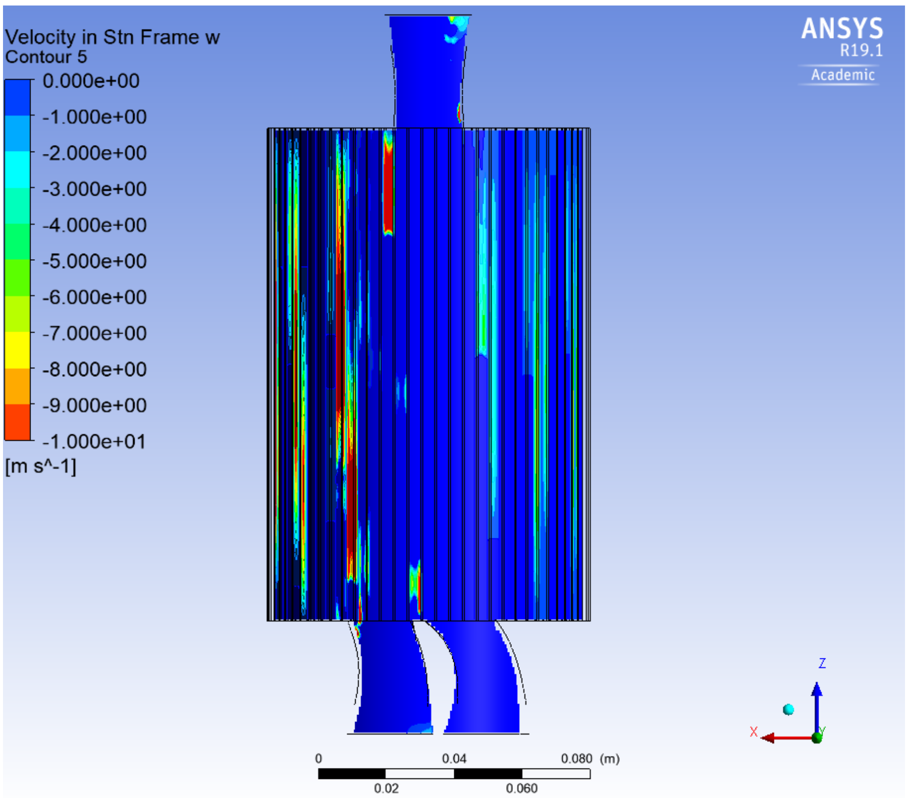

(b) Negative Z direction velocity

Figure F.6: Velocity direction plots

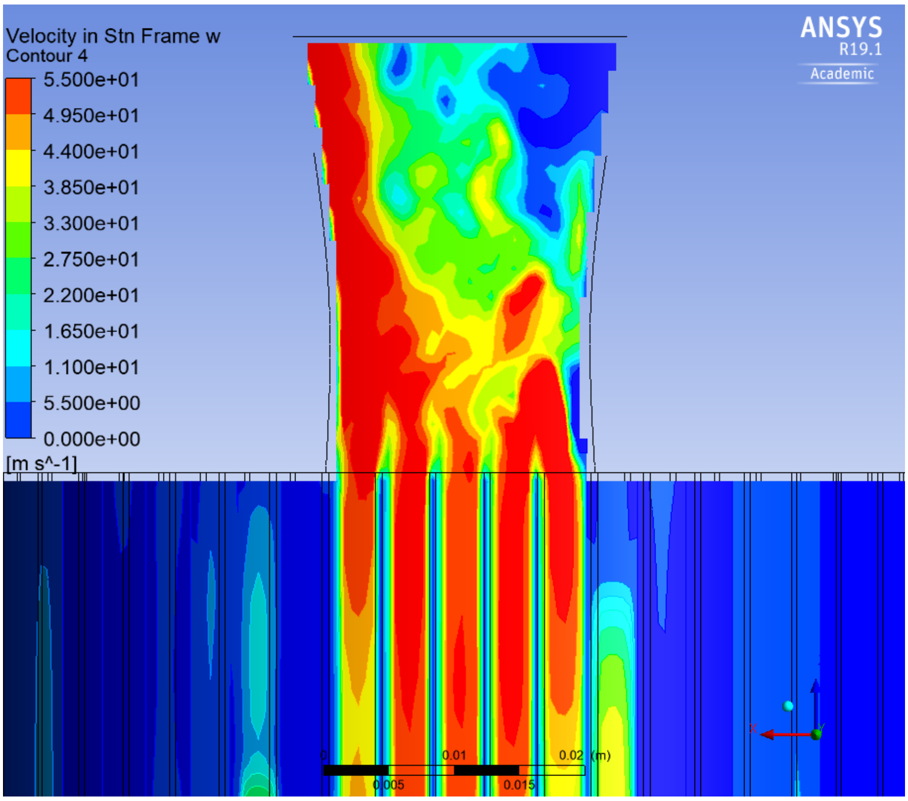

(a) Outlet port

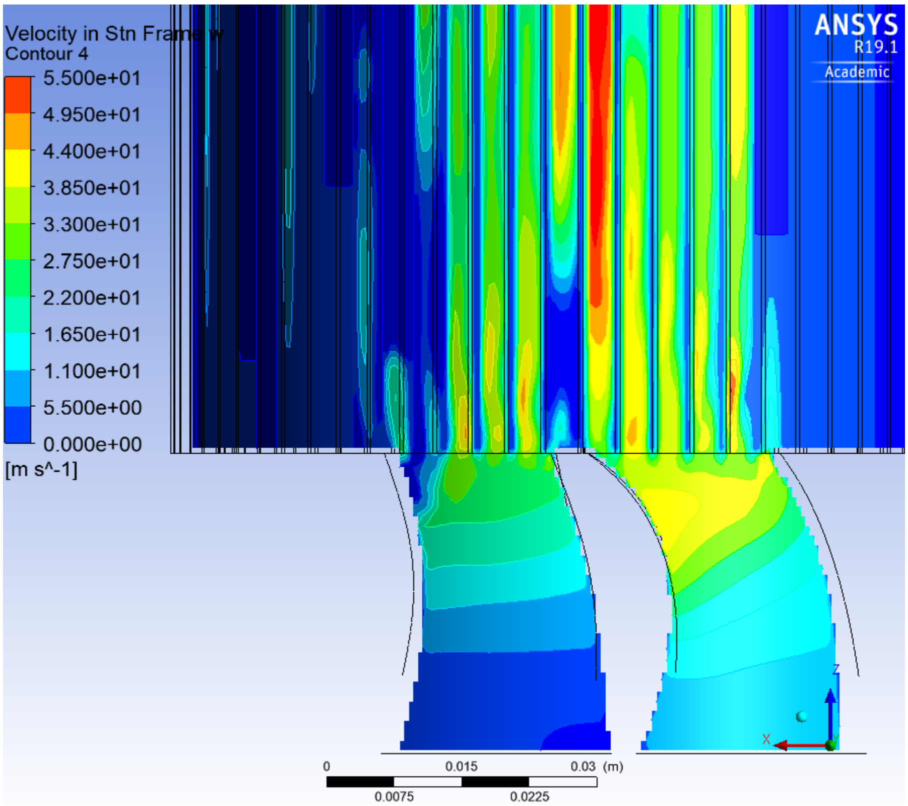

(b) Inlet ports

Figure F.7: Velocity positive Z direction ports close up

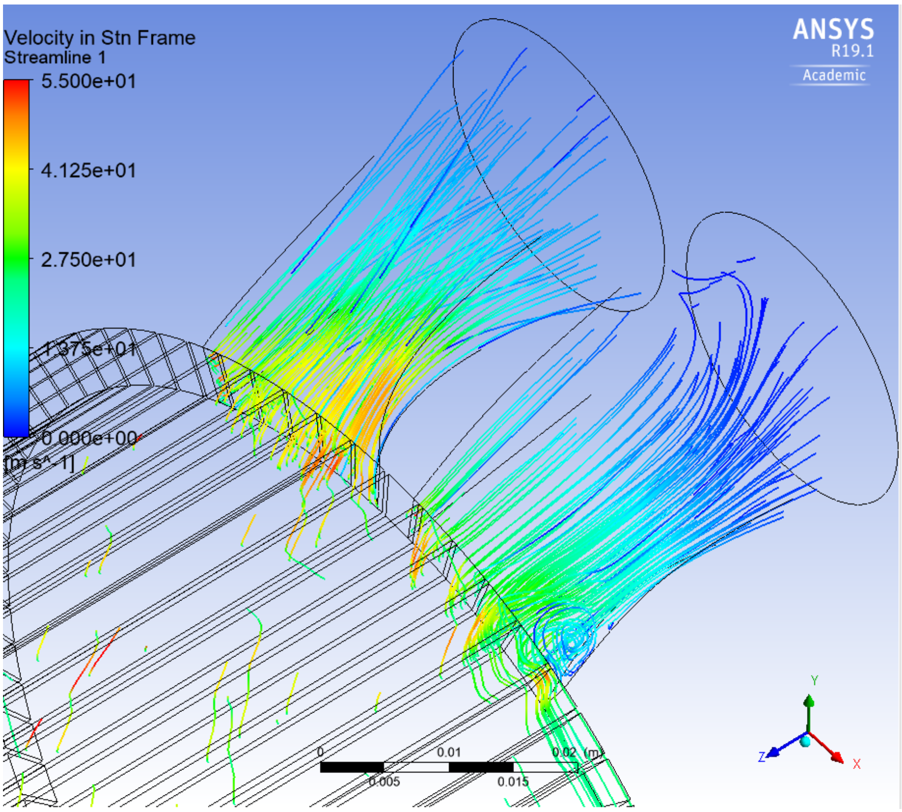

(a) Inlet ports

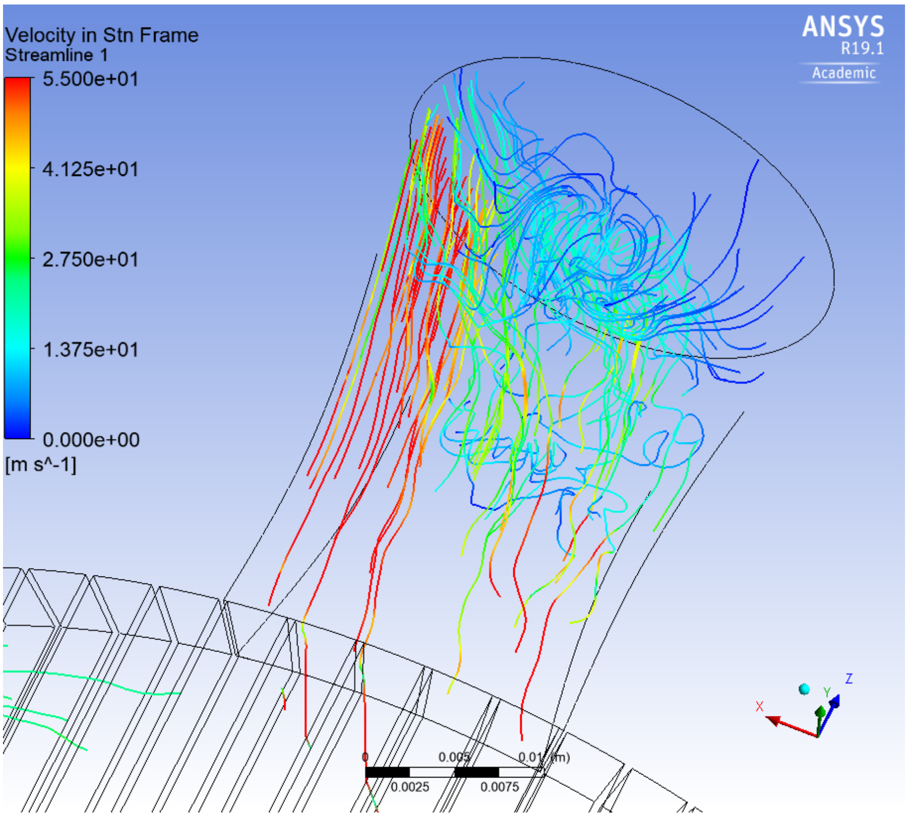

(b) Outlet port

Figure F.8: Port velocity streamlines

Appendix G

Risk Management Plan

UNIVERSITY OF SOUTHERN QUEENSLAND

University of Southern Queensland — Print View

USQ Safety Risk Management System

Version 2.0

Safety Risk Management Plan

Risk Management Plan ID:	Status:	Current User:	Author:	Supervisor:	Approver:
RMP_2019_3560	*Approve*	i:0#.w|usq\u1085095	i:0#.w|usq\u1085095	i:0#.w|usq\buttswod	i:0#.w|usq\buttswod

Assessment Title:	Wave rotor experiments in P10	Assessment Date:	20/06/2019
Workplace (Division/Faculty/Section):	204070 - School of Mechanical and Electrical Engineering	Review Date:	(5 years maximum)

Approver: *David Buttsworth*	*Supervisor: (for notification of Risk Assessment only)* *David Buttsworth*

Context

DESCRIPTION:

What is the task/event/purchase/project/procedure?	Experiments associated with final year project work in Engineering
Why is it being conducted?	For training and research
Where is it being conducted?	P10
Course code (if applicable)	ENG4111/4112
Chemical Name (if applicable)	

WHAT ARE THE NOMINAL CONDITIONS?

Personnel involved	Liam Channer, David Buttsworth, Brian Lenske
Equipment	Wave rotor apparatus, including rotor and associated instrumentation
Environment	Normal laboratory conditions - nominally greater than 10 degC and less than 30 degC
Other	
Briefly explain the procedure/process	Assemble, configure, commission, instrument, experiment with spinning but enclosed rotor and low pressure air flows in and out of the device

Assessment Team - who is conducting the assessment?

Assessor(s):	Liam Channer
Others consulted: (eg elected health and safety representative, other personnel exposed to risks)	*Brian Lenske*

RMP continued...

Risk Matrix					
	Consequence				
Probability	Insignificant No Injury 0-$5K	Minor First Aid $5K-$50K	Moderate Med Treatment $50K-$100K	Major Serious Injury $100K-$250K	Catastrophic Death More than $250K
Almost Certain 1 in 2	M	H	E	E	E
Likely 1 in 100	M	H	H	E	E
Possible 1 in 1,000	L	M	H	H	H
Unlikely 1 in 10,000	L	L	M	M	M
Rare 1 in 1,000,000	L	L	L	L	L

Recommended Action Guide	
Extreme:	E= Extreme Risk – Task *MUST NOT* proceed
High:	H = High Risk – Special Procedures Required (Contact USQSafe) Approval by VC only
Medium:	M= Medium Risk - A Risk Management Plan/Safe Work Method Statement is required
Low:	L= Low Risk - Manage by routine procedures.

Risk Register and Analysis												
	Step 1	Step 2	Step 2a	Step 2b	Step 3			Step 4				
	Hazards: From step 1 or more if identified	*The Risk:* What can happen if exposed to the hazard without existing controls in place?	*Consequence:* What is the harm that can be caused by the hazard without existing controls in place?	*Existing Controls:* What are the existing controls that are already in place?	*Risk Assessment:* Consequence x Probability = Risk Level			*Additional Controls:* Enter additional controls if required to reduce the risk level	*Risk assessment with additional controls:* Has the consequence or probability changed?			
					Probability	*Risk Level*	*ALARP*		*Consequence*	*Probability*	*Risk Level*	*ALARP*
	Example											
	Working in temperatures over 35⁰ C	*Heat stress/heat stroke/exhaustion leading to serious personal injury/death*	*catastrophic*	*Regular breaks, chilled water available, loose clothing, fatigue management policy.*	*possible*	*high*	*No*	*temporary shade shelters, essential tasks only, close supervision, buddy system*	*catastrophic*	*unlikely*	*mod*	*Yes*
1	spinning apparatus	injury because of pinch points	Minor	rotor itself is fully enclosed in a metal housing and the belt drive is appropriately guarded. motor drive power is limited and device easily stalls if overloaded. only trained personnel are operating the wave rotor and remain clear of the hazard during operation.	Unli	Low	✓					
2	moderately compressed air flows	injury from noise or high speed flow of air	Insignifi	level of compression of the air is very modest due to the physical characteristics of the device and is very unlikely to exceed atmospheric pressure.	Poss	Low	✓					

RMP continued...

3	vacuum	injury due to suction	Insignifi	suction points are enclosed and inlets are guarded or controlled by needle valve	Rare	Low							
4	electricity - instrumentation	minor electric shock	Insignifi	all instruments are powered by either low voltage and current limited laboratory power supplies (with appropriate tag and testing up to date and laboratory RCD active) or 6 V low amp-hour sealed lead acid battery.	Poss	Low							
5	240 V electric motor drive	electric shock	Modera	variable speed drive wired up by qualified electrical technical officer as device instruction manual, all connections are appropriately insulated and physically inaccessible to routine operation. all 240 V components purchased new for this project. laboratory RCD functioning. 240 V power unplugged unless rotor testing is being performed.	Rare	Low							

Step 5 - Action Plan (for controls not already in place)

	Additional Controls:	Exclude from Action Plan: (repeated control)	Resources:	Persons Responsible:	Proposed Implementation Date:

Supporting Attachments

View Attachments

Click here to attach a file

Step 6 – Request Approval

Drafters Name: *Liam Channer*

Draft Date: *20/06/2019*

Drafters Comments:

Assessment Approval: All risks are marked as ALARP

Maximum Residual Risk Level: Low - Manager/Supervisor Approval Required

Document Status: *Approve*

Step 6 – Approval

Approvers Name: *David Buttsworth*

Approvers Position Title: *supervisor*

Approvers Comments:

I am satisfied that the risks are as low as reasonably practicable and that the resources required will be provided.

Approval Decision: *Approve*

Approve / Reject Date: *20/06/2019*

Document Status: *Approve*